Corrosion properties of 17-4 PH martensitic stainless steel obtained by additive manufacturing

Michella Alnajjar

▶ **To cite this version:**

Michella Alnajjar. Corrosion properties of 17-4 PH martensitic stainless steel obtained by additive manufacturing. Other. Université de Lyon, 2019. English. NNT : 2019LYSEM035 . tel-02966675

HAL Id: tel-02966675
https://theses.hal.science/tel-02966675

Submitted on 14 Oct 2020

HAL is a multi-disciplinary open access archive for the deposit and dissemination of scientific research documents, whether they are published or not. The documents may come from teaching and research institutions in France or abroad, or from public or private research centers.

L'archive ouverte pluridisciplinaire **HAL**, est destinée au dépôt et à la diffusion de documents scientifiques de niveau recherche, publiés ou non, émanant des établissements d'enseignement et de recherche français ou étrangers, des laboratoires publics ou privés.

N°d'ordre NNT : 2019LYSEM035

THESE de DOCTORAT DE L'UNIVERSITE DE LYON
opérée au sein de
Mines Saint-Etienne

Ecole Doctorale N° 488
Sciences, Ingénierie, Santé

Spécialité de doctorat : Sciences et Génie des Matériaux

Soutenue publiquement le 18/12/2019, par :

Michella ALNAJJAR

Corrosion properties of 17-4 PH martensitic stainless steel obtained by additive manufacturing

Devant le jury composé de :

Delagnes, Denis	Professeur	IMT Mines Albi	Président
Duhamel, Cécilie	Professeur	Mines ParisTech	Rapporteure
Blanc, Christine	Professeur	Toulouse INP-ENSIACET	Rapporteure
Delagnes, Denis	Professeur	IMT Mines Albi	Examinateur
Christien, Frédéric	Professeur	Mines Saint-Etienne	Directeur de thèse
Wolski, Krzysztof	Directeur de recherche	Mines Saint-Etienne	Co-directeur de thèse
Bosch, Cédric	Chargé de recherche	Mines Saint-Etienne	Co-encadrant
Grosjean, Christophe	Ingénieur	CETIM	Invité

Spécialités doctorales	Responsables :	Spécialités doctorales	Responsables
SCIENCES ET GENIE DES MATERIAUX	K. Wolski Directeur de recherche	MATHEMATIQUES APPLIQUEES	O. Roustant, Maître-assistant
MECANIQUE ET INGENIERIE	S. Drapier, professeur	INFORMATIQUE	O. Boissier, Professeur
GENIE DES PROCEDES	F. Gruy, Maître de recherche	SCIENCES DES IMAGES ET DES FORMES	JC. Pinoli, Professeur
SCIENCES DE LA TERRE	B. Guy, Directeur de recherche	GENIE INDUSTRIEL	N. Absi, Maître de recherche
SCIENCES ET GENIE DE L'ENVIRONNEMENT	D. Graillot, Directeur de recherche	MICROELECTRONIQUE	Ph. Lalevée, Professeur

EMSE : Enseignants-chercheurs et chercheurs autorisés à diriger des thèses de doctorat (titulaires d'un doctorat d'État ou d'une HDR)

ABSI	Nabil	MR	Génie industriel	CMP
AUGUSTO	Vincent	CR	Image, Vision, Signal	CIS
AVRIL	Stéphane	PR2	Mécanique et ingénierie	CIS
BADEL	Pierre	MA (MDC)	Mécanique et ingénierie	CIS
BALBO	Flavien	PR2	Informatique	FAYOL
BASSEREAU	Jean-François	PR	Sciences et génie des matériaux	SMS
BATTON-HUBERT	Mireille	PR2	Sciences et génie de l'environnement	FAYOL
BEIGBEDER	Michel	MA (MDC)	Informatique	FAYOL
BLAYAC	Sylvain	MA (MDC)	Microélectronique	CMP
BOISSIER	Olivier	PR1	Informatique	FAYOL
BONNEFOY	Olivier	PR	Génie des Procédés	SPIN
BORBELY	Andras	MR(DR2)	Sciences et génie des matériaux	SMS
BOUCHER	Xavier	PR2	Génie Industriel	FAYOL
BRODHAG	Christian	DR	Sciences et génie de l'environnement	FAYOL
BRUCHON	Julien	MA (MDC)	Mécanique et ingénierie	SMS
CAMEIRAO	Ana	MA (MDC)	Génie des Procédés	SPIN
CHRISTIEN	Frédéric	PR	Science et génie des matériaux	SMS
DAUZERE-PERES	Stéphane	PR1	Génie Industriel	CMP
DEBAYLE	Johan	MR	Sciences des Images et des Formes	SPIN
DEGEORGE	Jean-Michel	MA (MDC)	Génie industriel	Fayol
DELAFOSSE	David	PR0	Sciences et génie des matériaux	SMS
DELORME	Xavier	MA (MDC)	Génie industriel	FAYOL
DESRAYAUD	Christophe	PR1	Mécanique et ingénierie	SMS
DJENIZIAN	Thierry	PR	Science et génie des matériaux	CMP
BERGER-DOUCE	Sandrine	PR1	Sciences de gestion	FAYOL
DRAPIER	Sylvain	PR1	Mécanique et ingénierie	SMS
DUTERTRE	Jean-Max	MA (MDC)		CMP
EL MRABET	Nadia	MA (MDC)		CMP
FAUCHEU	Jenny	MA (MDC)	Sciences et génie des matériaux	SMS
FAVERGEON	Loïc	CR	Génie des Procédés	SPIN
FEILLET	Dominique	PR1	Génie Industriel	CMP
FOREST	Valérie	MA (MDC)	Génie des Procédés	CIS
FRACZKIEWICZ	Anna	DR	Sciences et génie des matériaux	SMS
GARCIA	Daniel	MR(DR2)	Sciences de la Terre	SPIN
GAVET	Yann	MA (MDC)	Sciences des Images et des Formes	SPIN
GERINGER	Jean	MA (MDC)	Sciences et génie des matériaux	CIS
GOEURIOT	Dominique	DR	Sciences et génie des matériaux	SMS
GONDRAN	Natacha	MA (MDC)	Sciences et génie de l'environnement	FAYOL
GONZALEZ FELIU	Jesus	MA (MDC)	Sciences économiques	FAYOL
GRAILLOT	Didier	DR	Sciences et génie de l'environnement	SPIN
GROSSEAU	Philippe	DR	Génie des Procédés	SPIN
GRUY	Frédéric	PR1	Génie des Procédés	SPIN
HAN	Woo-Suck	MR	Mécanique et ingénierie	SMS
HERRI	Jean Michel	PR1	Génie des Procédés	SPIN
KERMOUCHE	Guillaume	PR2	Mécanique et Ingénierie	SMS
KLOCKER	Helmut	DR	Sciences et génie des matériaux	SMS
LAFOREST	Valérie	MR(DR2)	Sciences et génie de l'environnement	FAYOL
LERICHE	Rodolphe	CR	Mécanique et ingénierie	FAYOL
MALLIARAS	Georges	PR1	Microélectronique	CMP
MOLIMARD	Jérôme	PR2	Mécanique et ingénierie	CIS
MOUTTE	Jacques	CR	Génie des Procédés	SPIN
NAVARRO	Laurent	CR		CIS
NEUBERT	Gilles			FAYOL
NIKOLOVSKI	Jean-Pierre	Ingénieur de recherche	Mécanique et ingénierie	CMP
NORTIER	Patrice	PR1	Génie des Procédés	SPIN
O CONNOR	Rodney Philip	MA (MDC)	Microélectronique	CMP
PICARD	Gauthier	MA (MDC)	Informatique	FAYOL
PINOLI	Jean Charles	PR0	Sciences des Images et des Formes	SPIN
POURCHEZ	Jérémy	MR	Génie des Procédés	CIS
ROUSSY	Agnès	MA (MDC)	Microélectronique	CMP
ROUSTANT	Olivier	MA (MDC)	Mathématiques appliquées	FAYOL
SANAUR	Sébastien	MA (MDC)	Microélectronique	CMP
SERRIS	Eric	IRD		FAYOL
STOLARZ	Jacques	CR	Sciences et génie des matériaux	SMS
TRIA	Assia	Ingénieur de recherche	Microélectronique	CMP
VALDIVIESO	François	PR2	Sciences et génie des matériaux	SMS
VIRICELLE	Jean Paul	DR	Génie des Procédés	SPIN
WOLSKI	Krzystof	DR	Sciences et génie des matériaux	SMS
XIE	Xiaolan	PR0	Génie industriel	CIS
YUGMA	Gallian	CR	Génie industriel	CMP

Mise à jour : 30/08/2018

Table of contents

General introduction

The main objective of this thesis was to study the corrosion behavior of 17-4 PH stainless steel fabricated by selective laser melting (SLM). It was conducted in the SMS Materials and mechanical engineering R&D center (LGF laboratory) of Mines Saint-Etienne (France).

This work was motivated by the growing demand of additively manufactured materials, specifically of selective laser melted alloys. Additive manufacturing is a relatively new technology that allows 3D objects to be fabricated layer by layer according to a computer-aided design (CAD). SLM is a technique of additive manufacturing, which utilizes high power laser to melt metallic powder to produce 3D objects. SLM is still in its development period and there are still many limitations for this technology, including the availability and price of powders, the limited choice of materials, sanitary issues and problems in the recyclability of powders. In addition, another very important issue is the durability of the SLM-ed materials in service conditions, which is still unclear and not fully explored. The durability of SLM-ed steels was our point of interest is in this PhD study.

After defining the context of this thesis, the choice of the material had to be done, which depended on the availability of the powder and the ease of fabrication by SLM technique. The 17-4 PH stainless steel was selected for this study, because it responded to those criteria. In addition, it is one of the most used materials in the SLM fabrication and thus it was easy to find industrial partners able to produce SLM-ed 17-4 PH steel with optimized process parameters. Thus, the durability study was conducted on SLM-ed 17-4 PH steels having limited porosity and appropriate mechanical properties compared to its wrought counterpart. What motivated our study is also the limited research on this SLM-ed steel so far, in particular concerning its durability.

The durability is a very wide and complex subject, but obviously, due to the limited time of the PhD, we had to choose specific types of conditions and environments. Our first choice was to investigate the electrochemical corrosion because it is the most encountered type of corrosion during service of stainless steels, including 17-4 PH steel. The electrochemical characterization was done in a typical acidic medium containing 30 g/l NaCl, which is close to the seawater concentration and already used a lot in corrosion research. Our second choice was to study the hydrogen embrittlement (HE), that is a crucial problem to address since hydrogen is likely to enter the material as soon as corrosion reactions occur at the surface during service. In addition, high strength steels as the one studied here are expected to be sensitive to hydrogen embrittlement. We thought it would be interesting to investigate how a high strength material produced using SLM would be affected by HE.

It was a deliberate choice in this study to work in a comparative manner: the different series of experiments were always conducted on both the SLM-ed material and the conventional wrought

material. Several SLM-ed materials were studied; they were obtained from different industrial partners. A list of the different materials, including SLM-ed and wrought, is provided in Appendix 1.

This thesis is divided into four main chapters. The first chapter is the literature review and the three following chapters present the work done during this PhD thesis.

The first chapter presents a review on additive manufacturing with particular interest on selective laser melting (SLM) process and the microstructures obtained by SLM. This was followed by a literature review on the microstructure of wrought and SLM-ed 17-4 PH steels. The corrosion of stainless steels and some corrosion measurements techniques were then discussed. A literature review on the corrosion of SLM-ed stainless steels, wrought and SLM-ed 17-4 PH steels were presented. A presentation on hydrogen embrittlement (HE) was given, which included hydrogen-metal interaction, hydrogen diffusion and trapping and HE mechanisms. A literature review on HE of ferritic and martensitic steels, the effect of strain rate and yield strength on HE and subcritical crack growth was conducted.

The second chapter of this thesis is dedicated to the study of the microstructure of SLM-ed 17-4 PH steel in the as-built state. It was expected that the resulted microstructure would be different from its wrought counterpart, due to the high thermal rates and the complex thermal history experienced during SLM. Optical microscopy, X-ray diffraction, scanning electron microscopy equipped with electron backscatter diffraction and energy-dispersive X-ray spectroscopy were all used in this study. In addition, a comparison of microstructures was made between wrought and SLM-ed steels. A detailed analysis was conducted to fully understand this unique SLM-ed microstructure. Dilatometry measurements were done in order to identify the phase transformations in this steel at high temperatures. Furthermore, microstructures of 17-4 PH steels obtained by different SLM machines were also observed in order to generalize and ensure reproducibility of the results. As shown in this chapter the microstructures obtained in the as-built state are very unique and different from the conventional martensitic microstructure of the wrought 17-4 PH steel. One approach could have been to heat treat the SLM-ed material to make it "as similar as possible" to the wrought material. This is not the approach we followed. In contrast, we thought that the unique microstructure obtained from SLM was very interesting from the academic point of view. This is the reason why the corrosion studies presented in the following chapters were conducted on the SLM-ed steel without any treatment likely to recover the usual microstructure of 17-4 PH steel.

The third chapter of this thesis focused on the corrosion properties of the SLM-ed 17-4 PH steel, specifically the electrochemical behavior. First, the microstructures of wrought steel and two SLM-ed steels (as-built and after solution treatment) were identified, which included their phase constitutions,

their inclusion, and their porosity contents. Secondly, anodic scans were performed on all three materials in acidic chloride containing environment. As the corrosion behavior is directly related to the microstructure, it was very important to correlate the electrochemical results with the observed microstructures. Furthermore, X-ray photoelectron spectroscopy was used to confirm the correlation between surface composition and corrosion behavior.

The fourth chapter of this thesis continue the investigation of the corrosion properties of the SLM-ed 17-4 PH steel, specifically the hydrogen embrittlement. The materials studied were both wrought and SLM-ed steels that were subjected to an overaging treatment at 580°C for 4 hours. As usual, their microstructures were first reviewed. This was followed by tensile testing in air for smooth and notched specimens. Slow strain rate tests (SSRT) were then performed under cathodic charging in acidic chloride solution. Comparisons were made between the stress-strain curves in air and under hydrogen charging for both wrought and SLM-ed steels, in order to evaluate the degree of hydrogen susceptibility for each steel. The effect of strain rate and pre-charging on hydrogen susceptibility were also investigated. The fracture surfaces were observed after each test. Moreover, electrochemical permeation tests were conducted to reveal the hydrogen diffusion distance during SSRT. The analysis consisted of correlating the SSRT results and the observed fractographs to the charging conditions and the microstructures. The hydrogen embrittlement mechanisms of each material were also discussed, in a comparative way.

The three main chapters of this manuscript are presented as self-consistent papers. Each of them contains a short literature review, in addition to the general literature review presented at the beginning of the manuscript.

Chapter 1Literature review

Table of contents

1.1 Additive manufacturing

Additive manufacturing (AM) also known as 3D-printing refers to the technologies that builds a three-dimensional object by adding material layer by layer according to computer-aided design (CAD) model. As opposed to traditional "subtractive" fabrication methods where the finished part is obtained by removing material from a block part by cutting and/or drilling, AM requires almost no tooling in order to produce a functioning part. This technique is capable of building parts having very complex geometries that usually are difficult or sometimes impossible to be fabricated by conventional manufacturing processes [1–4]. In addition, AM presents a lot of potential benefits such as reducing the fabrication time and making economies in material by minimizing the waste. Thus, due to its various advantages, AM has been developing and growing rapidly in the past few years. By 2016, the global 3D printing market reached nearly US$ 3.7 billion and is expected to grow at a compound annual growth rate of 23% for the period of 2016-2021 [5].

This technology was first introduced in the late 1980 as rapid prototyping solution and was later evolved to rapid tooling and manufacturing. In the early stages, AM was used for rapid prototyping such as building prototype parts for testing and assessment, fabricating models for art and medical uses and casting patterns. As development and improvement of AM technology continued to grow, indirect and direct tooling emerged as a new method of fabrication of tools, molds and dies [6]. More recently, AM has been adopted for building near-net shape and end-use products [2,3]. Its application has broadened to include biomedical industries, aerospace, civil engineering, automobile and even fashion industries [3,7]. A wide range of materials can be used in AM including plastics, polymers, metals, concrete, ceramics and human tissue. Depending on the state of the material used, AM can be divided into 3 main groups: liquid based such as fuse deposition modelling, solid based such as laminated object manufacturing and powder based such as selective laser sintering [8]. AM incorporates different processes that can be classified into seven different categories [1,9]:

1- Binder jetting (BJ) where a liquid binding agent is printed into thin layer of powder particles to join them together. An example of BJ process is 3D inkjet technology.

2- Directed energy deposition (DED) where focused thermal energy melts materials during deposition. Examples of this process are laser engineered net shaping and 3D laser cladding.

3- Material extrusion (ME) where material is pushed out through a nozzle and deposited layer by layer. The most common example of ME is fuse deposition modelling.

4- Material jetting (MJ) where material is jetted from a nozzle on the build platform using continuous or drop on demand method.

5- Powder bed fusion (PBF) where a laser or electron beam source selectively fuses a powder layer deposited on the build platform. Examples of PBF are electron beam melting (EBM) and selective laser sintering (SLS) or melting (SLM).

6- Sheet lamination (SL) where sheets or ribbons of material are bonded together. Examples of this process are ultrasonic additive manufacturing and laminated object manufacturing.

7- Vat photopolymerization (VP) where liquid polymer in a vat is light-cured.

AM is still an evolving technology and many researches are being done in order to improve the profitability and the quality of produced materials. However, there are still some limitations for this technology, which includes poor surface quality due to "stair-stepping" effect, the limited number of materials that can be used, poor repeatability and powder availability [3,10]. In addition, the microstructures obtained are usually different from their wrought counterparts. Thus, their mechanical and corrosion properties need to be thoroughly examined before their use in service [11].

1.2 Selective laser melting

Selective laser melting (SLM) is the most widely used AM technique which is based on powder bed fusion. SLM is a relatively new technology that appeared in the late 90's. It has developed from rapid prototyping to direct manufacturing. This is mainly because SLM is capable of producing near-net shape "fully" dense material that can reach a density of 99.99% and requires few post-processing stages [12,13]. This leads to significant gain in production rate and cost due to the elimination of expensive post-processes. In addition, materials produced by SLM can have comparable mechanical properties to their cast counterparts. The materials that are being used in this process include copper, aluminum, micro-alloyed steels, stainless steels, superalloys, titanium and their composites [12].

As for all AM techniques, SLM process begins with the preparation of CAD data. It is then converted to StereoLithography (STL) files before being uploaded to the SLM machine. The building process begins by deposing a thin layer of metal powder onto the building plate in the building chamber. Then, a high energy laser source melts selectively certain region of the laid powder according to the processed CAD data. Then, another powder layer is deposited above the previous one, and the laser scans the powder. The process repeats itself until building the required part (**Figure 1. *1***). Once the building process is complete the excess powder is removed and the part is cut from the substrate plate [12].

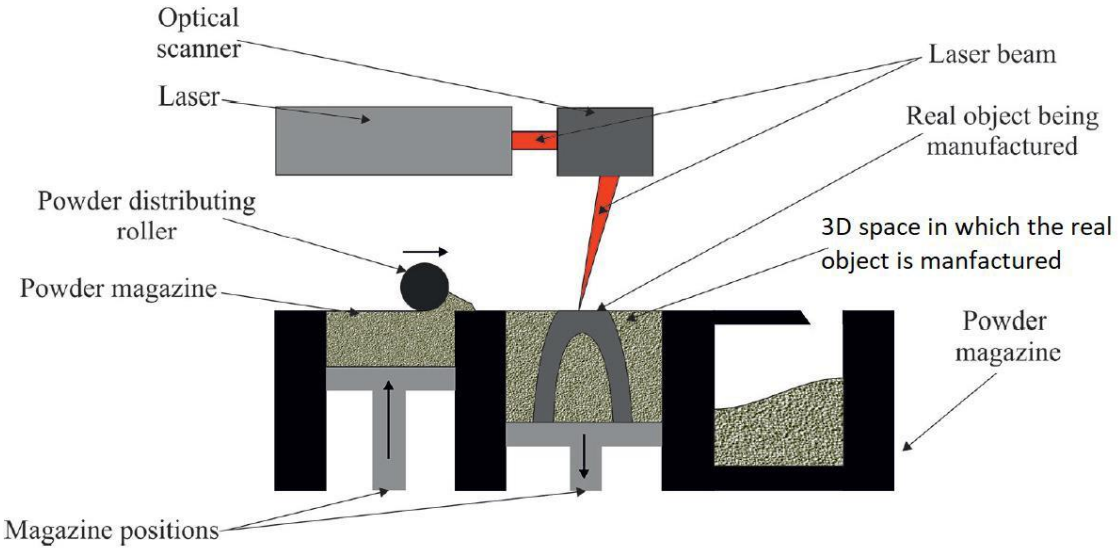

Figure 1. 1: Schematic representation of the Selective Laser Melting (SLM) process [14].

All the building process is done in the building chamber where an inert gas is purged, usually argon or nitrogen, in order to avoid oxygen contamination and subsequent oxidation. The building chamber can be heated to minimize the thermal stresses caused by the large thermal gradients and cooling rates. In addition, a pre-heating of the substrate plate (200–500°C) can also be done for the same reason [12]. Powder parameters should be considered during the process since they can affect the final part quality. The powder particle size, size distribution, shape, density are among many other powder parameters. Gas-atomized powders are usually adopted due to their high sphericity as compared to water atomized powders (**Figure 1. *2***). A spherical powder shape is desirable for better powder packing density and consequently better final part density. A wider range of powder particle size provides higher powder bed density and generates smoother side surface finish [15]. The powder particle size usually varies between 1 and 100 µm [16]. Finer powder size will lead to an improved surface roughness, but can reduce powder flowability. Thus, a compromise should be achieved between good flowability for coarser particles and better surface finish for finer particles [15,17].

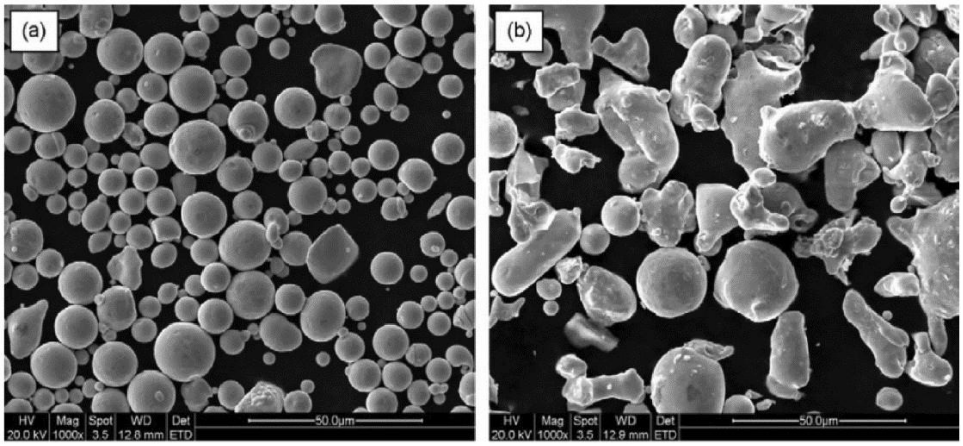

Figure 1. 2: (a) Gas-atomized powder and (b) water-atomized powder of 316L stainless steel [15].

Furthermore, a large number of process parameters should be optimized to obtain a nearly fully dense functioning part. The most important parameters include laser power, laser speed, layer thickness and hatch spacing. **Figure 1.** ***3*** depicts a schematic representation of these parameters. The commonly used laser system for SLM is Nd:YAG fiber laser ($\lambda \sim 10.6$ µm), with a power varying between 50 and 1000 W. The laser operates in continuous mode [16]. The beam diameter/spot size can typically vary between 30 to 1000 µm [18]. By increasing the laser beam diameter, the SLM build rate is improved but at the cost of precision and surface roughness [19]. The laser scan speed usually varies from some dozen mm/s to some thousand mm/s [20], while the layer thickness ranges between 20 to 100 µm [12]. The "stair-stepping" effect is more visible with higher layer thickness [16]. The hatch spacing is the distance between neighboring scan vectors that allows a certain degree of re-melting of the previous track [18,19]. At high hatch spacing, i.e. at insufficient overlap of adjacent melt pools, lack of fusion occurs which leads to high porosity content [19]. These parameters are almost never varied independently, but rather their combinations are adjusted. For instance, they can be combined into one parameter called laser energy density E (J/mm^3) [15]:

$$E = \frac{P}{vht}$$

Where P is the laser power (W), v is the scanning speed (mm/s), h is the hatch spacing (mm), and t is the layer thickness (mm). The laser energy density has a direct effect on the densification of the final part and consequently its mechanical properties. **Figure 1.** ***4*** depicts the operating window as a function of laser power and scan speed. In this window, the laser energy is efficiently absorbed by the powder and produces a stable melt pool of optimum size with good fusion with the previous layer, while avoiding excessive re-melting [21]. This will lead to a fully dense part. However, for a very low energy density (low laser power, high scan speed), the melt pool is small leading to unmelted powder

and high lack of fusion porosity content. In contrast, for very high energy density (high laser power, low scan speed), the penetration of the laser into the metal is too deep leading to keyhole formation. In this regime, the melt pool is unstable and the vaporization of material and trapping of gas take place. At very high power and speed, the melt pool tends to disconnect into metal balls. This phenomenon is called, the balling effect [21]. As can be seen, the melt pool size is dependent on the process parameters. Ref. [22] gives an example of melt pool size for 316L stainless steel: for 200 W of laser power, 50 µm of layer thickness, 75 µm of beam diameter, 400 mm/s of scan speed and 75 µm of hatch spacing, the width of the melt pool is 221 µm and the depth is 81.4 µm. By comparing the depth of the melt pool with the layer thickness, a re-melting of previous layer can be noticed [22].

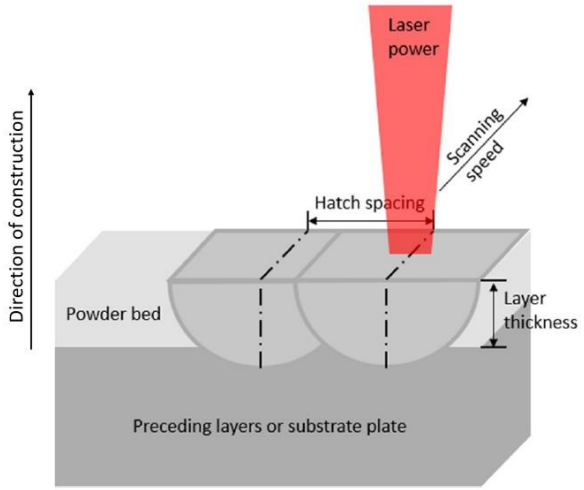

Figure 1. 3: SLM process parameters: laser power, scanning speed, hatch spacing and layer thickness [12].

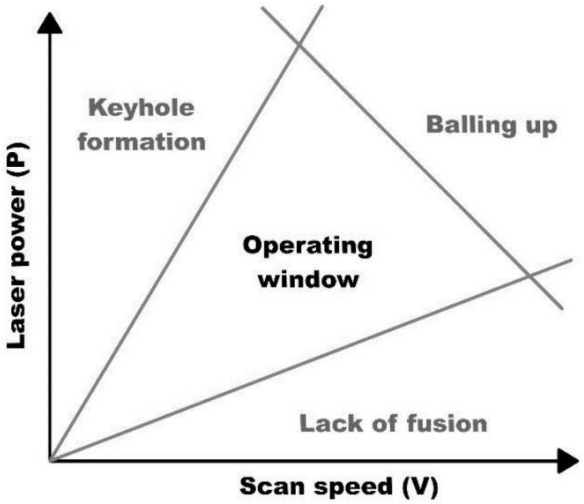

Figure 1. 4: Schematic representation of the operating window as a function of laser power and scan speed [21].

The laser scanning strategy also have an effect on the quality of the final part. **Figure 1. *5*** shows some examples of scanning strategies. These scanning strategies can influence the thermal history during

SLM and consequently alter the material properties including crystallographic texture, anisotropy [23] and residual stresses [24].

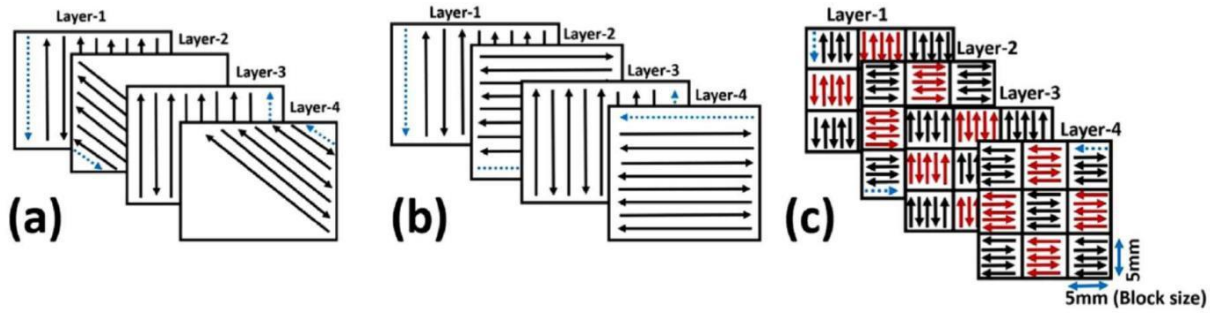

Figure 1. 5: Schematic representation of laser scanning strategies (a) 45° Alternating (b) 90° Alternating (c) Chessboard Scanning [24].

After fabrication of the part, post-processing tasks are required to produce a functioning part. The first post-process is the removal of the materials that surround the part by brushes or compressed air [25]. It is usually followed by a heat treatment to relieve residual stresses, before the removal of the substrate and the rigid extra structures that connect the part to the substrate. This is usually done by using metal cutting techniques such as milling, band saws [16]. Furthermore, the surface roughness obtained from the SLM process can vary from several µm to more than one hundred µm, depending on the optimization of process parameters [26]. The typical roughness value of as-built SLM parts is between 10 and 30 µm, which is significantly higher than the value obtained by traditional mechanical methods (<1-2 µm) [27]. Thus, post-processes are needed to flatten the surface such as bead blasting, wet or dry sanding and hand polishing. In addition, hot isostatic pressing may also be applied to eliminate the pores [16,25].

1.2.1 Microstructures of SLM-ed materials

During the SLM process, the metal powder first undergoes rapid solidification in the order of 10^5-10^6 K/s. Then, the solidified melt pool will be re-melted and subjected to multiple rapid heating and cooling (10^5-10^6 K/s) due to adjacent laser scans and the melting of the upper layers [11,28]. Hence, the rapid thermal rates experienced during SLM will result in microstructures usually different from their wrought counterparts. Some studies have reported dislocation cell sub-structures (***Figure 1. 6***) [29–31], high residual stresses in the order of several hundred MPa [32,33] and highly crystallographically textured columnar grains (***Figure 1. 7***) [34–37]. In ***Figure 1. 7***, coarse grains can be observed that extend over several powder layers along the build direction due to epitaxial growth. Furthermore, the microstructures might also have different phase constitution and elemental segregation, compared to wrought materials [38,39]. The latter is due to the high solidification rates that result in dendritic or cellular morphology of the solid/liquid interface. ***Figure 1. 8*** shows elemental

segregation of Mo and Cr in the as-built SLM-ed 316L steel. Concerning phase constitution of SLM-ed metals, some studies found that duplex stainless steels fabricated by SLM resulted in a mono-phase ferritic microstructure in contrast to the dual phase structure of their wrought counterparts [30,40]. This was attributed to the retention of delta ferrite. All these findings prove that the as-built SLM-ed microstructure is none other than the retained solidification structure. As mentioned earlier, some metallurgical defects may be formed such as hot tear cracks, entrapped gas porosity and lack of fusion porosity (***Figure 1. 9***) [41,42]. However, by optimizing the process parameters, the porosity level can be significantly reduced. For example, a residual porosity of <0.05 vol% was reached for SLM-ed Ti6Al4V [43]. Based on these findings, the mechanical and corrosion behaviors of the SLM-ed steels are expected to be different from their wrought counterparts.

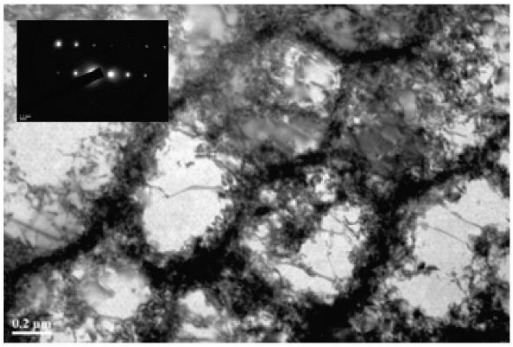

Figure 1. 6: Bright field TEM image of the dislocation structures observed in the as-built 316L steel fabricated by SLM [29].

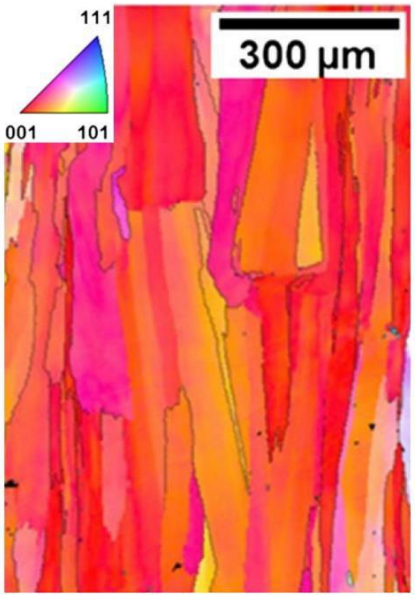

Figure 1. 7: IPF map obtained by EBSD of as-built 316L steel fabricated by SLM showing highly textured columnar coarse grains. The build direction is vertical [36].

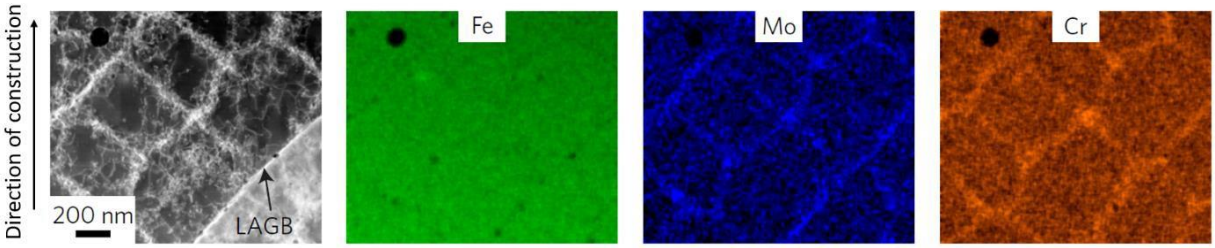

Figure 1. 8: A high-angle annular dark-field scanning TEM image with corresponding energy-dispersive spectroscopy (EDS) maps showing segregation of Mo and Cr to the solidification cellular walls in the as-built 316L steel fabricated by SLM (LAGB: low angle grain boundaries) [39].

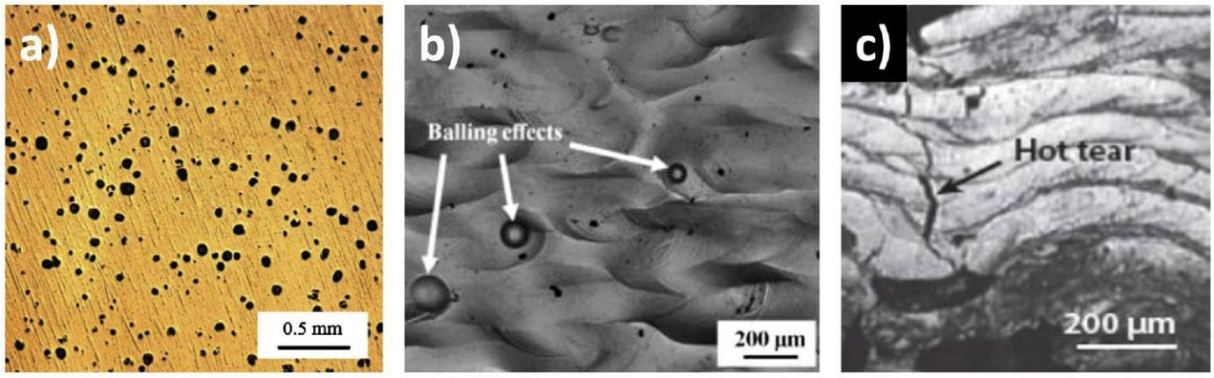

Figure 1. 9: Examples of defects that can form in SLM materials: (a) porosity, (b) balling and (c) hot tears [41].

1.3 17-4 PH stainless steel

1.3.1 Wrought 17-4 PH stainless steel

The material used in this study is 17-4 PH stainless steel. It is the most popular grade of precipitation hardenable stainless steel due to its high tensile strength, fracture toughness and corrosion resistance. It is widely used in a variety of applications, including oil field valve parts, chemical process equipment, aircraft fittings and pump shafts [44]. This steel contains 15-17.5% Cr, 3-5% Ni and 3-5% Cu.

Wrought 17-4 PH steel exhibits a martensitic microstructure supersaturated with copper after a solution heat treatment at about 1040-1050°C in the austenite domain, followed by cooling to room temperature. ***Figure 1. 10*** shows a typical martensitic microstructure of wrought 17-4 PH steel with martensite lathes inside the prior austenitic grains [45]. The martensitic matrix exhibits a very high

dislocation density $\sim 4 \times 10^{15}$ m^{-2} [46]. Some minor fraction of δ ferrite can also be observed [44,47,48]. In addition, NbC carbides and inclusions such as MnS are present in the solution annealed condition [49,50]. Typically, this steel is used after an aging treatment in the range 480-620°C. This aging treatment results in strengthening by precipitation of copper-rich particles. 17-4 PH steel attains its peak hardness and strength after 1 hour maintain at 480°C, as shown in **Figure 1. *11*** [44]. In the early stages of aging treatment, copper precipitates are coherent with the martensitic matrix. As the time progresses, copper precipitates continue to grow and transform to incoherent FCC particles. The typical size of the copper rich precipitates in the coherent state is about 2-5 nm (***Figure 1. 12***). For

example, after an aging treatment at 400°C for 100 hours, the size of the copper precipitates is around 3 nm [49]. As for the incoherent copper precipitates their size can reach some dozens nm. An aging treatment at 620°C for 4 hours results in an average size of copper particles of about 30 nm [44]. Furthermore, the chromium concentration in 17-4 PH stainless steel is within the solid state miscibility gap. As a result, a phase decomposition of the martensite into chromium-rich α' and iron-rich α phases is expected to occur below 550°C after long time aging. This decomposition induces hardening of the steel [51,52]. In addition, reverted austenite can form with the aging treatments at temperatures above 550°C. No significant effect of reverted austenite on the mechanical properties and impact toughness of the material has been observed [53]. However, the maximum content of reverted austenite measured in this study was about 4%.

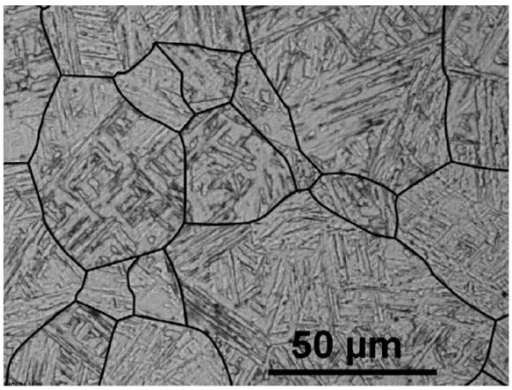

Figure 1. 10: Optical micrograph of wrought 17-4 PH steel showing a typical martensitic microstructure [45].

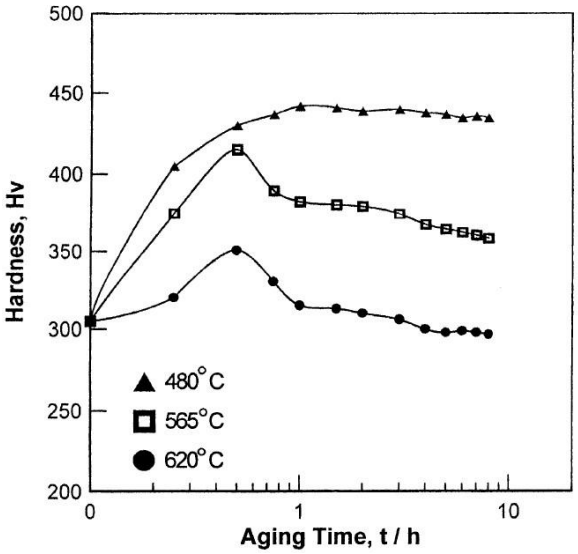

Figure 1. 11: The evolution of the hardness with aging time at various temperatures [44].

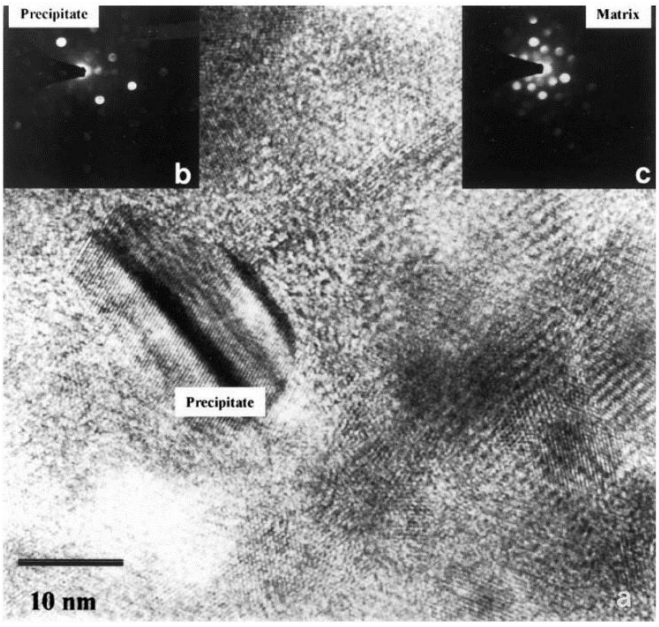

Figure 1. 12: (a) FEG-TEM bright field image and corresponding diffraction patterns for (b) copper precipitate obtained from the specimen aged at 480 ◦C for 1 h and (c) the matrix [44].

The phase transformation martensite/austenite in this steel has been a subject of many researches [44,45,54–58]. It was found that the martensite to austenite transformation during heating begins at approximately 650°C and it is achieved at approximately 1000°C. During cooling, the displacive martensitic transformation occurs between 130°C and room temperature [45]. However, there was little to no investigation concerning the phase transformation at very high temperatures (i.e. between 1000°C and 1400°C) in this steel [54]. Thus, it is currently not known in which phase (either austenite or δ ferrite) this steel solidifies.

1.3.2 SLM-ed 17-4 PH steel

The first part of this thesis deals with the microstructure of 17-4 PH steel obtained by SLM process. Several research groups studied the microstructure of SLM-ed 17-4 PH steel and the influence of process parameters. For instance, Murr *et al.* [59] found that the powder atomization in an argon (Ar) environment produced martensitic powders. In contrast, in a nitrogen (N_2) environment, the microstructure of atomized powder was primarily austenite. The SLM fabrication using either austenitic or martensitic powders in an Ar environment resulted in a mostly martensitic microstructure, according to the authors. In contrast, after SLM fabrication in N_2 environment, the microstructure of the part was similar to the powder microstructures (either austenitic or martensitic) [59]. They attributed the retained austenite to the presence of nitrogen that stabilized this phase. In addition, the observed microstructures had columnar grains elongated in the direction of construction (***Figure 1. 13***). Rafi *et al.* [60], Starr *et al.* [61] and Cheruvathur *et al.* [38] had similar observations. Furthermore, they found a dendritic-cellular solidification structure due to the high cooling rates

experienced during SLM. Cheruvathur *et al.* [38] also reported microsegregation of elements that led to the presence of an austenite phase enriched with austenite stabilizers.

Based on these findings, the powder atomization and the SLM fabrication environments should be chosen carefully, because of their significant effect on the phase constitution of SLM-ed 17-4 PH steel. In this study, an argon environment was used during the SLM construction. According to the literature [59–61], the microstructure should be mainly martensitic regardless of the powder atomization environment. In these reports, the phase analysis was done by X-ray diffraction and optical microscopy. By using X-ray diffraction, these authors were able to identify the BCC and FCC phases. However, this technique is not capable of distinguishing between martensite and possible δ ferrite, since both phases have a BCC structure. Furthermore, even though the microstructure was considered martensitic, the optical micrographs observed by Murr et *al.* [59] didn't reveal a typical martensitic microstructure with lathes (***Figure 1. 13***). Thus, based on these reports, the microstructure of as-built SLM-ed 17-4 PH steel fabricated under an argon environment was not clearly identified and further investigation should be done.

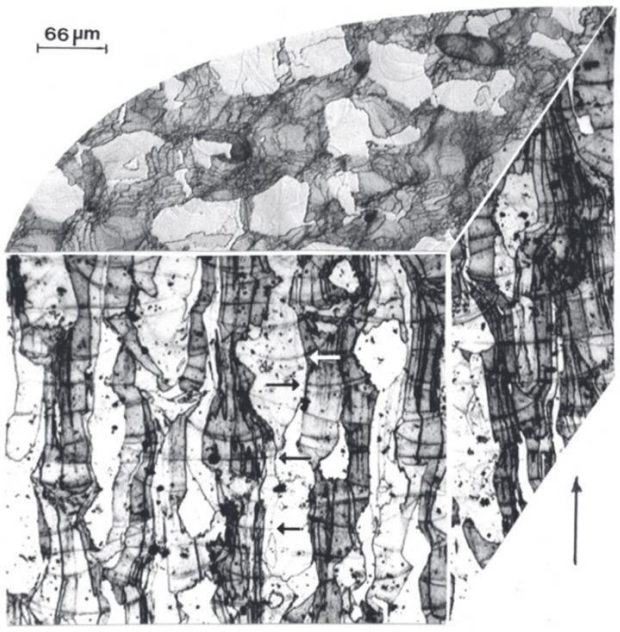

Figure 1. 13: 3D optical micrograph of as-fabricated 17-4 PH steel in argon environment using argon atomized 17-4 PH steel powder. Arrow shows the build direction [59].

1.4 Corrosion of stainless steels

Stainless steels are widely used in a variety of applications such as food processing, petrochemical plants and transportation industries, due to their high strength and good corrosion resistance. They

are iron-based alloys that contain at least 11% chromium. This chemical composition is necessary to develop an adherent chromium-rich oxide surface film, which acts as a barrier to metal surface corrosion in atmospheric and aqueous environment. This oxide film forms and heals itself in the presence of oxygen [62]. The stability of the passive film is determined by its composition, thickness (typically 1-3 nm) and structure. For an alloy containing 15% chromium, the chromium content in the passive film can be as high as 80% [63]. The passive film on stainless steel can be mainly divided into two layers: exterior layer formed by iron hydroxide and an interior layer formed by chromium oxide [64]. The latter has the protective properties. The passive film also changes depending on the environment: it can grow, dissolve and adsorb or incorporate anions [65]. The presence of certain anions such as chlorides and sulphates may be detrimental to the film stability and lead to pit initiation. Although stainless steels have good corrosion resistance, they can still be subjected to corrosion in some environments and conditions. Depending on the environment, there are mainly two types of corrosion: wet and dry. In this study, the focus will be on wet (aqueous) corrosion, which occurs by electrochemical mechanism. The phenomenon usually consists of anodic oxidation of metallic substances and the cathodic reduction of environmental substances. The anodic reaction of the metal is of the form:

The ions M^{y+} are transferred to the solution and the released electrons are conducted through the metal to the cathodic area where they are consumed by the following cathodic reaction:

$$X^{y+} + ne^- \rightarrow X$$

The typical reduction reactions in aqueous solution are hydrogen evolution: $(2H^+ + 2e^- \rightarrow 2H)$ in acidic solution and oxygen reduction: $(O_2 + 2H_2O + 4e^- \rightarrow 4OH^-)$ in neutral solution or $(O_2 + 4H^+ + 4e^- \rightarrow 2H_2O)$ in acidic solution. For the corrosion to occur, four requirements must be met [66]:

1. An anodic site for oxidation reaction,
2. A cathodic site for reduction reaction,
3. An electric circuit in the metal for connection between the two sites,
4. An ionic circuit in the aqueous solution or connection between the two sites

The most common forms of corrosion in aqueous environment for stainless steels are: pitting corrosion, crevice corrosion, general corrosion, stress corrosion cracking, intergranular corrosion and galvanic corrosion [67]. General and pitting corrosions in aqueous environment are the two types of corrosion that are relevant to the present study.

1.4.1 General corrosion

General corrosion, also called uniform corrosion, is the most common form of corrosion and is responsible for most of the material loss. During this type of corrosion, the anodic and cathodic reactions take place all over the electrode surface but not simultaneously at the same place. These reactions exchange places constantly. The general corrosion proceeds evenly over the entire exposed surface or over a large fraction of the total surface. This will result in general thinning of the material (***Figure 1. 14***). However, this type of corrosion is not recognized as dangerous since it can be simply predicted and can be prevented by different protection methods [68]. For stainless steels, general corrosion occurs when they are in contact with acidic mediums at pH lower than their depassivation pH, which de-stabilize the passive layer.

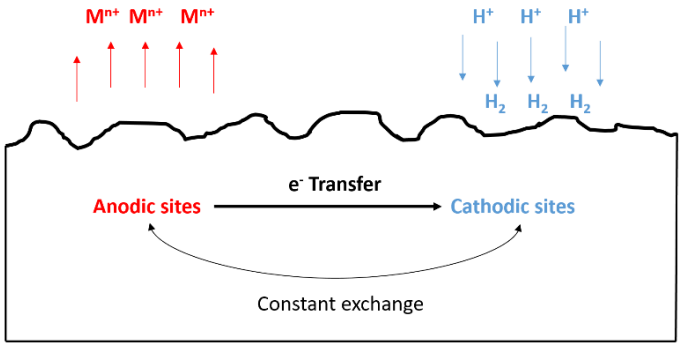

Figure 1. 14: Schematic representation of general corrosion of stainless steels in acidic solution.

1.4.2 Pitting corrosion

In contrast to general corrosion, pitting is a form of localized corrosion where small specific sites on the metal surface is attacked, while the rest of the surface remains passive. Pitting in stainless steels is often due to chloride ions. The latter penetrates the protective oxide film at specific sites and leads to its breakdown. Anodic reaction occurs at the specific site, while cathodic reactions take place at the protected surface (***Figure 1. 15***). The pitting corrosion normally initiates at some microstructural defects or discontinuities in the passive film caused by inclusions, grain boundaries and dislocations [69]. Pitting is a dangerous form of corrosion because it cannot be predicted and sometimes cannot be detected due to small, narrow pits. Performance of stainless steels in the area of pitting is usually assessed using the pitting resistance equivalent number (PREN). The higher the PREN number, the more resistant the material is supposed to be. The PREN number is determined by the nitrogen, molybdenum and chromium contents [67]:

$$PREN = \%Cr + 3.3(\%Mo) + 16(\%N)$$

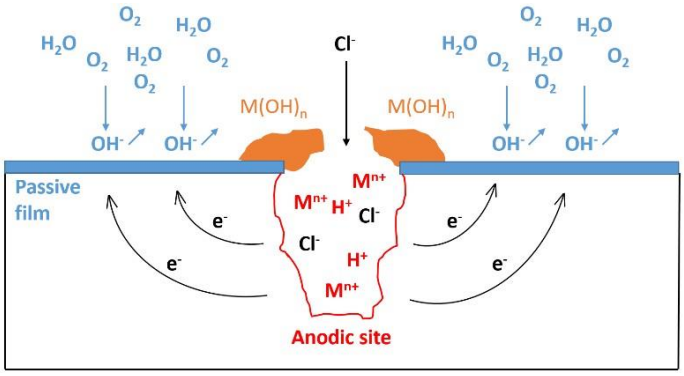

Figure 1. 15: Schematic representation of pitting corrosion of stainless steels.

1.4.3 Corrosion measurement techniques

Many techniques are used to assess the corrosion behavior of stainless steels in the laboratory including measurement of corrosion potential (E_{corr}) versus time, potentiodynamic polarization, linear polarization, electrochemical impedance and electrochemical noise measurement. In the second part of this thesis, the first two techniques were used to study the corrosion behavior of 17-4 PH stainless steel and will be explained more in details.

1.4.3.1 Open circuit potential (OCP)

Open circuit potential (OCP), also called corrosion or rest potential, is the potential that indicates the tendency of a metal to electrochemical oxidation in a corrosive medium [70]. It is not characteristic of the metal like the thermodynamic equilibrium potential, but instead depends on the experimental conditions such as the pH, oxygen content, concentration of specific anions and temperature of the aqueous solution, and the surface state of the metal. At this potential, the exchange of the whole charges between the metal and the solution is at the equilibrium. Nevertheless, the kinetics of oxidation and reduction reactions may differ due to the evolution of the density of active surfaces and the evolution of the local environment, notably the pits [67,71]. The variation of OCP with time is an indication of changes in the nature of the surface of the metal. ***Figure 1. 16*** shows the main shapes that the curves of OCP versus time can take:

a) OCP increases steadily with time to more positive values, indicating the passivation of the metal by formation of a protective oxide film,
b) OCP become more and more negative indicating a continuous attack of the metal,
c) OCP first becomes more negative then tends to positive values. This is an indication of an attack followed by passivation,

d) OCP first becomes positive then tends to negative values. This indicates the presence of a protective film at the immersion. The film develops for a certain duration, and then it is attacked leading to its destruction.

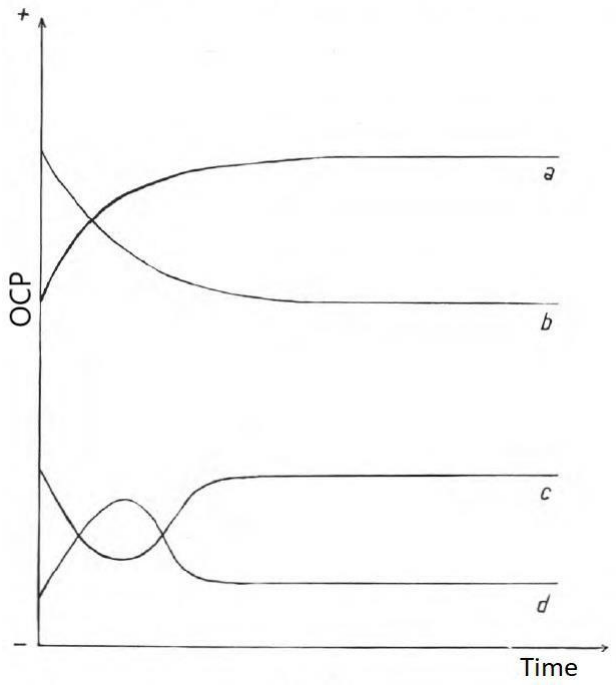

Figure 1. 16: Most common shapes of the OCP versus time curves [71].

1.4.3.2 Potentiodynamic polarization

In a potentiodynamic polarization experiment, the driving force (i.e. the potential) for anodic or cathodic reactions is controlled, and the net change in the reaction rate (i.e. the current) is observed. The potentiostat measures the current which must be applied to the system in order to achieve the desired increase in driving force [72]. A schematic representation of a typical anodic polarization curve of stainless steels in acidic medium is given in ***Figure 1. 17.a***. As the potential increases from the cathodic potentials, there is a region (active region) where the current density increases, which corresponds to the general oxidation/dissolution of the steel. The current density reaches a maximum and then decreases. In the passive region, the steel dissolution is much slower or is passive due to the formation of a protective oxide film. As the potential further increases, the current density increases due to pitting or oxygen evolution or transpassive metal dissolution [72,73]. ***Figure 1. 17.b*** shows the evolution of the anodic characteristic of stainless steels when decreasing the pH and increasing the chloride content. It can be seen that the passivity range decreases and the anodic current increases, which indicates a loss in passivity.

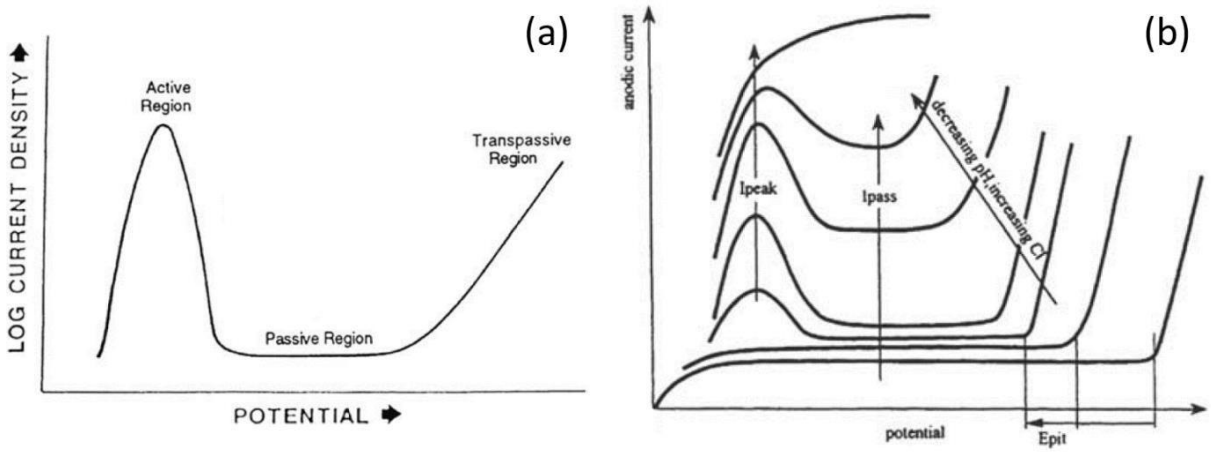

Figure 1. 17: (a) Typical anodic polarization curve of stainless steels exhibiting passivity, (b) evolution of the anodic characteristic of stainless steel when decreasing the pH and increasing the chloride content [73].

1.4.4 Corrosion of SLM-ed stainless steels

Corrosion studies of SLM-ed stainless steels have principally been reported on 316L austenitic stainless steel [11,74–81]. Chao *et al.* [74] and Sun *et al.* [75] investigated the corrosion behavior of SLM-ed 316L stainless steel in 0.6 M NaCl and found that the SLM-ed steel was more resistant to pitting corrosion compared with its wrought counterpart. This behavior was attributed to the absence of MnS inclusions in the SLM-ed steel. Similarly, Lodhi *et al.* [76] found that SLM-ed 316L had higher barrier properties of the passive film, which was associated to the fine polygonal shape grain structure and the absence of MnS inclusions. The effect of porosities on pitting of the SLM-ed 316L steel was investigated by Sun *et al.* [77] and Sander *et al.* [78]. The porosity values varied between 1% and 7% in the work of Sun *et al.* [77]. They found that the pitting potential and the repassivation potential were lower in the SLM-ed steel. This was attributed to the presence of porosities. On the other hand, Sander *et al.* [78] reported better pitting resistance for the SLM-ed steel and no trend in pitting potential with the increase of porosity. However, in this work the porosity values varied between 0.01% and 0.4%. Zhang *et al.* [79] studied the corrosion behavior of SLM-ed 316L steel by potentiodynamic anodic polarization in 3.5 wt. % NaCl solution. They found that corrosion potential was decreased with higher porosity content. Trelewicz *et al.* [80] found that SLM-ed 316L was less resistant in 0.1 M HCl due to inhomogeneous solute distribution, non-equilibrium microstructures and porosity. In general, in case of well controlled porosity content, the SLM-ed 316L steel had better corrosion resistance than its wrought counterpart, mainly due to the absence of MnS inclusions.

1.4.5 Corrosion of wrought 17-4 PH steel

Mudali *et al.* [82] studied the localized corrosion behavior of 17-4 PH steel in acidic chloride solution and sulfuric acid solution. Three different states were compared: solution annealed, aged and overaged. It was found that in acidic chloride medium, the aged steel exhibited passivity while the annealed and overaged states corroded uniformly. This was attributed to the presence of coherent copper precipitates that formed a protective copper oxide film and to the stress relieved martensitic matrix. However, the absence in passivity for the annealed state was attributed to the unaged (stressed) martensite, while for the overaged state it was attributed to the incoherent copper precipitates, $M_{23}C_6$ carbides and reverted austenite. Moreover, they found that localized corrosion occurred at the inclusions such as MnS inclusions. Syrett *et al.* [83] also studied the effect of microstructure on the pitting corrosion of 17-4 PH steel. Their results indicated that the microstructure had little to no effect on pitting, in particular the retained austenite and untempered martensite. However, the comparison was made only between two overaged states at different temperatures (tempered martensitic matrix) and the effect of copper was not discussed.

1.4.6 Corrosion of SLM-ed 17-4 PH steel

The second part of this thesis addresses the corrosion behavior of SLM-ed 17-4 PH steel by electrochemical means. Only few researches were found in the literature that investigated this subject. These studies performed electrochemical tests in almost similar chloride concentration solutions. Stoudt *et al.* [84] reported an improved corrosion resistance of SLM-ed 17-4 PH steel after a solution heat treatment compared with the wrought steel. This behavior was attributed to a finer martensite lath structure, more homogeneously distributed NbC precipitates and a more stable passive film. On the other hand, Schaller *et al.* [85] reported a reduced passivity range and active corrosion of the SLM-ed 17-4 PH steel compared to the wrought counterpart. This reduced corrosion resistance is attributed to the presence of porosity. The results presented by Stoudt *et al.* and Schaller *et al.* are contradictory. Hence, further investigation should be done by considering all the microstructure characteristics of SLM-ed 17-4 PH such as phase constitution, porosities, precipitations, inclusions and elemental distribution. Irrinki *et al.* [86] studied the effect of processing parameters and powder characteristics on the corrosion behavior of SLM-ed 17-4 PH steel. It was found that the density and consequently the corrosion resistance were improved by the increase in energy density. Finer powders gave better material density and corrosion resistance than coarser powders for the same laser energy level. Moreover, the corrosion resistance of SLM-ed 17-4 PH was superior compared to the wrought steel.

1.5 Hydrogen embrittlement

The third part of this thesis consisted of studying the hydrogen embrittlement (HE) of SLM-ed 17-4 PH stainless steel compared to the wrought steel. HE of materials was first recognized in the early 1870s. Since then, there has been intensive work to understand and characterize the HE phenomenon [87]. Many types of materials are susceptible to HE including high strength steels, high manganese-steel, aluminum alloys, titanium, magnesium and magnesium alloys [88]. The HE damage can be assessed by many manifestations such as a loss of ductility, reduction in tensile and fatigue strength and impact toughness.

Depending on the source of hydrogen, HE can be divided into two main groups [87]:

1. Hydrogen-environment embrittlement (HEE) involves cracking of materials under stress in hydrogen containing environment through hydrogen adsorption and absorption. The focus of this study is the HEE.
2. Internal hydrogen embrittlement in contrast takes place in the absence of hydrogenated environment. It involves the pre-existing hydrogen in the material that entered during fabrication and processing of materials.

1.5.1 Hydrogen-metal interaction

1.5.1.1 Hydrogen adsorption and absorption

The hydrogen adsorption on the metallic surface usually depends on the hydrogen containing environment (gaseous or liquid environment). In this study, the hydrogen was introduced by electrochemical charging in an aqueous acidic environment. During cathodic charging in acidic solutions, the hydrogen is present in the form of protons. The hydrogen adsorption occurs electrochemically, i.e. assisted by the potential, by reduction of hydrated protons according to Volmer reaction [89–91]:

$$^{+} + \square + \square \rightarrow \square H$$

$$H_{hy} \qquad \square\square\square$$

The adsorbed hydrogen on the surface can either be absorbed by the metal or desorbed by a recombination to form H_2 gas. The hydrogen desorption from the metal surface is supposed to occur through two possible paths:

A chemical desorption (Tafel reaction):

$$\square H_{\square\square\square} + \square H_{\square\square\square} \rightarrow H_{2(\square)} + 2\square$$

An electrochemical desorption (Heyrovsky reaction):

$$H_{ads} + H^+ + e^- \rightarrow H_2 + e$$

The atomic hydrogen transfer from the surface to the bulk occurs by a pure chemical reaction:

$$H_{ads} \rightarrow H_{abs} + e$$

1.5.1.2 Hydrogen diffusion

Once the hydrogen is absorbed, it can either be present in solid solution or trapped at some microstructural defects. Due to its small volume, hydrogen in solid solution can diffuse easily. The presence of microstructural defects such as grain boundaries and dislocations can also facilitate the hydrogen transport or induce trapping.

1.5.1.2.1 Lattice diffusion

Due to its small size, the hydrogen diffuses easily between interstitial sites (octaedric and tetraedric) inside the metallic material. The lattice diffusion consists in series of jumps from one interstitial site to another. For the jump to occur, a sufficient activation energy is required to overcome the energetic barrier. The main driving force for the diffusion is the concentration gradient [92]. In the ideal case of diffusion, i.e. without trapping and under concentration gradient, the hydrogen diffusion obeys Fick's laws:

$$J = -D\frac{\partial C}{\partial x}$$

$$\frac{\partial C}{\partial t} = D\frac{\partial^2 C}{\partial x^2}$$

Where J is the hydrogen flux, D is diffusion coefficient for the ideal case, C is the hydrogen concentration, t is the time and x is the distance in the diffusion direction. However, the diffusion can also be controlled by other gradients such as chemical potential, stress, electrical potential and temperature [92,93].

1.5.1.2.2 Short-circuit diffusion

The role of grain boundaries and dislocations in the hydrogen transport process is complex. These defects could slow the hydrogen diffusion by acting as trapping sites. However, they can also act as short-circuits and therefore enhance the hydrogen diffusion [92]. The contribution of grain boundaries

and dislocations to a faster diffusion process is limited to metals where the diffusion is relatively slow such as austenitic stainless steels and nickel alloys [94].

1.5.1.2.3 Hydrogen transport by moving dislocations

This concept was first proposed by Bastien and Azou [95]. They suggested the trapping of hydrogen by dislocations and their transport in the form of "Cottrell atmosphere" by moving dislocations. Under dynamic plastic deformation, the transport of hydrogen by moving dislocations may occur faster than lattice diffusion and can be a critical component in establishing the local conditions that promote failure. Thus this concept can be considered when the lattice diffusion is too slow to account for the observed cracking velocity [96]. Evidence of hydrogen transport by moving dislocations has been proposed in several experimental works [97–99].

1.5.1.3 Hydrogen trapping

From a thermodynamic point of view, a trapping site is considered as a site where hydrogen can lower its chemical potential. In order to escape a trap, hydrogen requires an energy substantially larger than lattice migration energy to overcome the energetic barrier of a trap. According to this energetic barrier, traps can be classified into reversible and irreversible traps [100]. Any microstructural defect inside the material such as dislocations, grain boundaries, particles and vacancies can act as trap for hydrogen. The effect of hydrogen trapping in material is to increase the apparent hydrogen solubility and to decrease the apparent diffusivity [101].

1.5.2 HE mechanisms

Over the years, multiple mechanisms have been proposed for the hydrogen embrittlement of metals. In this part, the possible mechanisms that are expected to occur in martensitic stainless steels are discussed.

A decohesion theory was first proposed by Pfeil in 1926 [87]. The hydrogen-enhanced decohesion (HEDE) mechanism was then developed by Troiano in 1959 and was later improved by Oriani [102]. Troiano suggested that interatomic bonds were weakened by the donation of hydrogen 1s electron to the unfilled 3d shell of iron atoms [103]. The decohesion mechanism is based on the weakening of average cohesive force between metal atoms by dissolved hydrogen. This will lead to a simple sequential separation of atoms.

In 1972 Beachem was the first to propose the mechanism of hydrogen-enhanced localized plasticity (HELP) [104]. It was proposed that the dislocation mobility increased with the presence of hydrogen in solid solution. A subsequent increase in local plastic deformation and decrease in macroscopic ductility

is observed on the fracture surface. The fracture mode could either be transgranular or intergranular depending on whether the hydrogen is localized within the grains or at the grain boundaries.

The adsorption-induced dislocation emission (AIDE) mechanism was first proposed by Lynch in 1976. In this mechanism, hydrogen is adsorbed at the surface of the crack tip, which will result in the reduction of cohesive force between atoms. The weakening of interatomic bonds will facilitate dislocations nucleation and its subsequent movement away from the crack tip [87]. Thus, the cracking occurs by a more localized plastic deformation, in addition to a microvoid coalescence process [105].

1.5.3 HE of ferritic steels

Malitckii *et al.* [106] investigated the hydrogen embrittlement of 18Cr ferritic stainless steel and found that this material was indeed susceptible to hydrogen embrittlement. The susceptibility increased with the increase in grain size. Fracture surfaces were found to be mainly transgranular. In addition, an increase in yield stress in the presence of hydrogen was observed. The side view of the specimen showed transgranular secondary cracks, which suggests subcritical crack growth. Konosu *et al.* [107] also reported the hydrogen susceptibility of ferritic stainless steel that manifested by a decrease in elongation to fracture and cleavage fracture mode. They observed an increase in yield strength for the hydrogen charged materials. Trasatti *et al.* [108] reported a reduction in ductility for X80 grade steel (ferrite/bainite) under hydrogen charging. They also found that the lower the strain rate the higher the susceptibility tended to be. Secondary cracks were also observed on the surface of all specimens indicating subcritical crack growth. Moreover, the fracture surfaces showed a mixed transgranular/intergranular mode for specimens tested in seawater, while they were mainly transgranular in sulfuric acid. Neeraj *et al.* [109] investigated the mechanism of hydrogen embrittlement in ferritic stainless steels and proposed a nanovoid coalescence mechanism coupled with hydrogen enhanced plasticity.

1.5.4 HE of martensitic steels

Shen *et al.* [110] reported a change from ductile to brittle intergranular fracture mode for a martensitic stainless steel under hydrogen charging. Lai et al. [111] found that 410 martensitic stainless steel was more susceptible to HE in the untempered state than in the tempered state. The fracture surface was mainly intergranular. Craig *et al.* [112] studied the hydrogen susceptibility of tempered martensite. They found that specimens tempered between 300°C and 500°C failed by intergranular mode while those tempered at higher temperatures failed by transgranular mode. The intergranular cracking was attributed to the phosphorus segregation and carbide formation at prior austenitic grain boundaries, while the transgranular cracking was initiated and propagated from the inclusions. Chen *et al.* found that HE susceptibility of ultra-high strength martensitic steel was reduced by low temperature

tempering due to the formation of epsilon-carbide that acted as hydrogen trapping sites. Lee *et al.* [113] and Nagao *et al.* [114] reported a beneficial effect of carbide precipitation on HE of martensitic steels. Kim *et al.* [115] found that tempered martensitic steel failed by intergranular mode under hydrogen charging. The intergranular mode was along prior austenitic grain boundaries. Sasaki *et al.* [116] reported that Mn segregation and MnS promote hydrogen-assisted cracking in tempered martensitic steel. The cracking was not transgranular but rather interface cracking. Beghini *et al.* [117] reported a strong hydrogen susceptibility of F82H martensitic steel. The threshold H concentrations for the transition from ductile to brittle intergranular mode was about 0.5 wppm for untempered state and reached 1.5 wppm for the tempered state. Furthermore, they reported a tendency toward an increase in susceptibility with the material strength. It can be concluded that one of the main characteristics of HE in martensitic steels is the occurrence of intergranular fracture (along prior austenitic grain boundaries), which seems to be much more frequent than in ferritic steels.

1.5.5 Effect of strain rate on HE

Momotani *et al.* [118] investigated the effect of strain rate on HE in low-carbon martensitic steel. They found that the elongation and the ultimate tensile strength decreased significantly with decreasing the strain rate (**Figure 1.** ***18***). Furthermore, the micro-cracks and fracture were mainly intergranular for the low strain rates, which was attributed to hydrogen accumulation on the prior austenitic grain boundaries. On the other hand, at higher strain rates, the micro-cracks and fracture became transgranular, due to insufficient time for hydrogen to accumulate on prior austenite grain boundaries. Bal *el at.* [119] and Hojo *et al.* [120] also found a decrease in elongation to fracture with the decrease in strain rates. Depover *et al.* [121] similarly found that HE increased with decreasing strain rates. This was attributed to the higher probability of H to diffuse to stress concentration regions ahead of the crack and accelerate failure. Toribio *et al.* [122] studied the effect of strain rate on HE of 316L stainless steel and found that fracture load decreases with the decrease in strain rate. Based on these reports, one can conclude that the HE is increased with the decrease in strain rate.

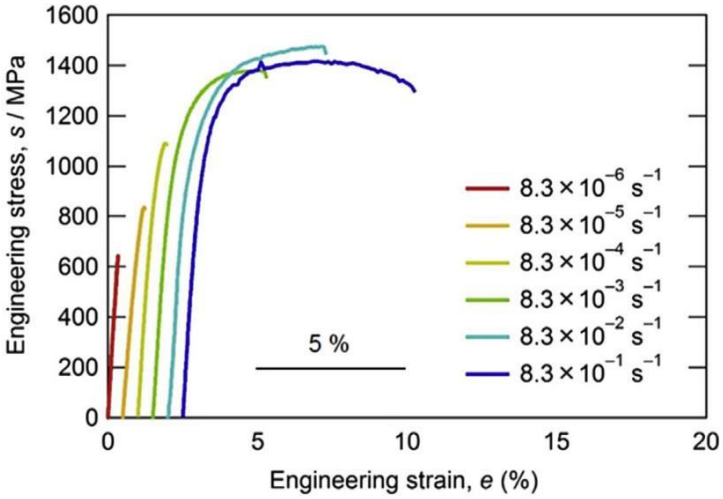

Figure 1. 18: Engineering stress-strain curves of hydrogen charged specimens under tensile testing at various strain rates, showing a decrease in elongation and stress with the decrease of strain rate [118].

1.5.6 Effect of yield strength on HE

Nanninga *et al.* [123] reported an increase in HE with the increase in hardness. It was also shown that the alloy composition and microstructural variations had some effect on HE of the studied alloys, however the strength of the steel was the dominant factor. ***Figure 1. 19*** shows a decrease in notch failure stress with the increase in hardness, for the hydrogen charged specimens. Brahimi *et al.* [124] investigated the HE of two tempered martensitic steels and found that below a hardness threshold the two steels were resistant to HE. The findings also demonstrate that although hardness and/or strength is the main factor affecting the susceptibility to HE, difference in chemistry leading to differences microstructural characteristics must also be considered. On the other hand, Bonagani *et al.* [125] studied the effect of tempering treatment on hydrogen embrittlement of martensitic stainless steel. It was found that the specimen tempered at 550°C was more susceptible to HE than the untempered and tempered at 300°C and 700°C specimens, although the specimen tempered at 550°C had lower hardness than the untempered and tempered at 300°C specimens. This result was attributed to the synergistic interaction of hydrogen and impurities segregated at prior austenitic grain boundaries. Thus, the strength is not the only factor controlling the susceptibility to HE, but also the microstructure and microchemical changes.

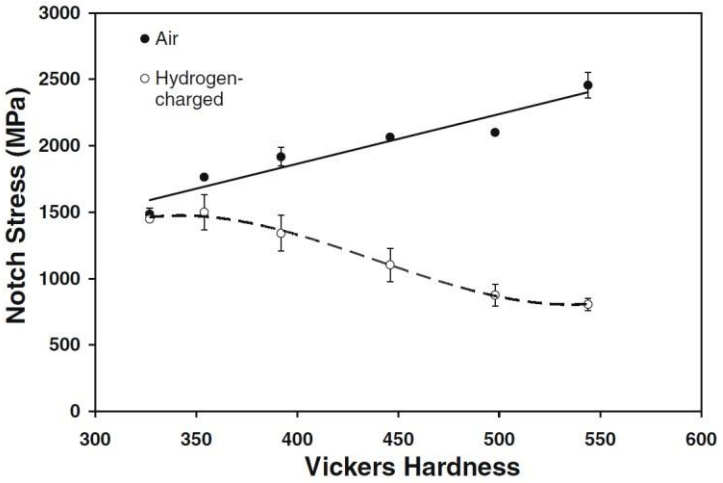

Figure 1. 19: Notch failure stress during a rising step load as a function of hardness, showing a decrease in notch failure stress with the increase in hardness for the hydrogen charged specimens [123].

1.5.7 Subcritical crack growth

Environment enhanced subcritical crack growth kinetics is illustrated in ***Figure 1. 20***. Crack growth starts at some apparent threshold stress intensity (K_{th}). Below K_{th} no observable crack growth occurs. For low K levels, the crack growth rate (da/dt) is strongly dependent on K and mostly independent of environmental conditions (stage I). At intermediate K, the crack growth rate becomes independent of K (stage II). As K approaches a critical value, or alternatively as the specimen becomes fully plastic, a rapid increase in growth rate (stage III) occurs. Stage III is followed by the specimen overload failure. The independence of the crack growth rate from the mechanical driving force (characterized by K) in stage II suggests that the growth rate is limited by chemical processes at the crack tip leading to embrittlement [126]. In other words, the crack growth rate in stage II is governed by the transport of corrosive species, such as hydrogen, to the crack tip. Stage II corresponds to the "subcritical" crack growth, in which the crack propagates "slowly" because of the environmental degradation of the crack tip. In the third stage, mechanical damage becomes much larger than environmental effect. At some point the toughness (K_{IC}) is reached and the crack critically propagates (i.e. fast propagation, of the order of the speed of sound in the metal). No environmental effect is expected in stage III because of the very high crack velocity.

When a material fails by critical crack propagation, it is very rare to observe secondary cracks. This is because once a crack has initiated, its propagation through the specimen is so fast that no other crack has enough time to initiate. In contrast, when subcritical cracking occurs, in a smooth tensile specimen for example, multiple secondary cracking is usually observed (***Figure 1. 21***).

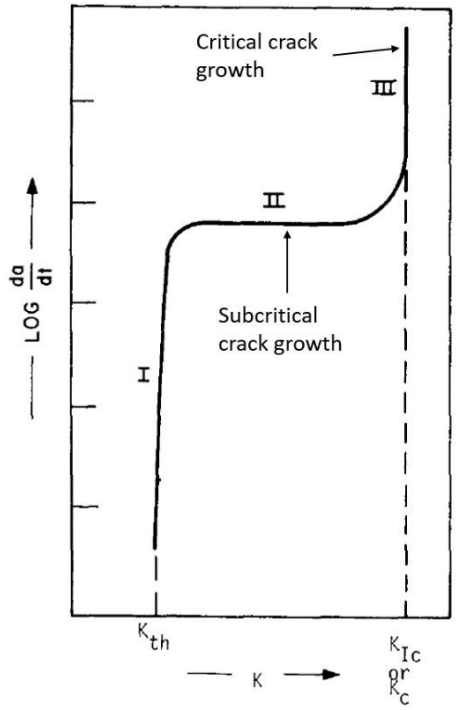

Figure 1. 20: Schematic representation of environment enhanced subcritical crack growth behavior [126].

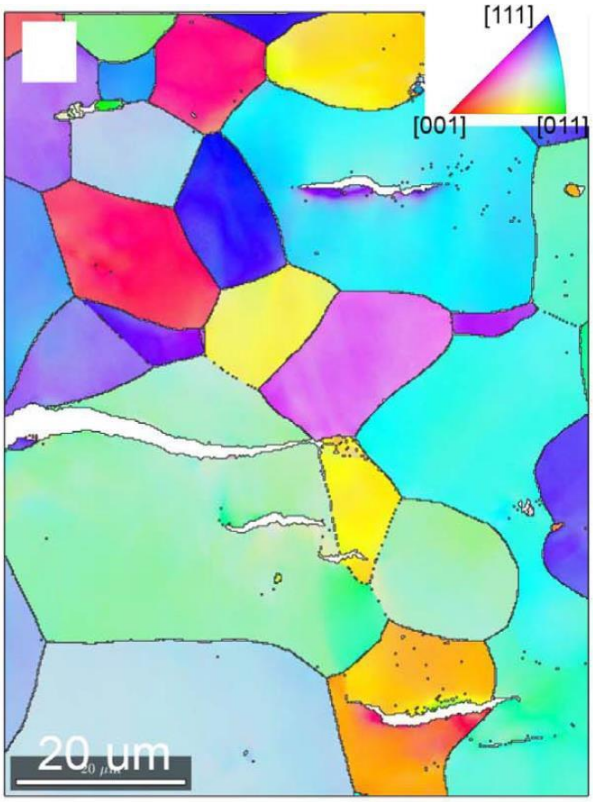

Figure 1. 21: EBSD map of the side surfaces of ferritic stainless steel specimen after tensile test under hydrogen charging showing secondary cracks, which suggests the occurrence of subcritical crack growth [106].

1.6 References

[1] S.A.M. Tofail, E.P. Koumoulos, A. Bandyopadhyay, S. Bose, L. O'Donoghue, C. Charitidis, Additive manufacturing: scientific and technological challenges, market uptake and opportunities, Mater. Today. 21 (2018) 22–37. https://doi.org/10.1016/j.mattod.2017.07.001.

[2] D. Herzog, V. Seyda, E. Wycisk, C. Emmelmann, Additive manufacturing of metals, Acta Mater. 117 (2016) 371–392. https://doi.org/10.1016/j.actamat.2016.07.019.

[3] N. Guo, M.C. Leu, Additive manufacturing: technology, applications and research needs, Front. Mech. Eng. 8 (2013) 215–243. https://doi.org/10.1007/s11465-013-0248-8.

[4] L.E. Murr, E. Martinez, K.N. Amato, S.M. Gaytan, J. Hernandez, D.A. Ramirez, P.W. Shindo, F. Medina, R.B. Wicker, Fabrication of Metal and Alloy Components by Additive Manufacturing: Examples of 3D Materials Science, J. Mater. Res. Technol. 1 (2012) 42–54. https://doi.org/10.1016/S2238-7854(12)70009-1.

[5] 3D printing market to grow by 23%, Met. Powder Rep. 71 (2016) 470–471. https://doi.org/10.1016/j.mprp.2016.10.011.

[6] D.T. Pham, S.S. Dimov, Rapid prototyping and rapid tooling—the key enablers for rapid manufacturing, Proc. Inst. Mech. Eng. Part C J. Mech. Eng. Sci. 217 (2003) 1–23. https://doi.org/10.1243/095440603762554569.

[7] T.D. Ngo, A. Kashani, G. Imbalzano, K.T.Q. Nguyen, D. Hui, Additive manufacturing (3D printing): A review of materials, methods, applications and challenges, Compos. Part B Eng. 143 (2018) 172–196. https://doi.org/10.1016/j.compositesb.2018.02.012.

[8] J.-P. Kruth, M.-C. Leu, T. Nakagawa, Progress in additive manufacturing and rapid prototyping, Cirp Ann. 47 (1998) 525–540. https://doi.org/10.1016/S0007-8506(07)63240-5.

[9] G.M. Shashi, A.R. Laskar, H. Biswas, K. Saha, A Brief Review of Additive Manufacturing with Applications, in: Proc. 14th Glob. Eng. Technol. Conf., Dhaka, Bangladesh, 2017: p. 23.

[10] Y. He, C. Montgomery, J. Beuth, B. Webler, Melt pool geometry and microstructure of Ti6Al4V with B additions processed by selective laser melting additive manufacturing, Mater. Des. 183 (2019) 108126. https://doi.org/10.1016/j.matdes.2019.108126.

[11] G. Sander, J. Tan, P. Balan, O. Gharbi, D.R. Feenstra, L. Singer, S. Thomas, R.G. Kelly, J.R. Scully, N. Birbilis, Corrosion of Additively Manufactured Alloys: A Review, CORROSION. 74 (2018) 1318–1350. https://doi.org/10.5006/2926.

[12] C.Y. Yap, C.K. Chua, Z.L. Dong, Z.H. Liu, D.Q. Zhang, L.E. Loh, S.L. Sing, Review of selective laser melting: Materials and applications, Appl. Phys. Rev. 2 (2015) 041101. https://doi.org/10.1063/1.4935926.

[13] P.K. Gokuldoss, S. Kolla, J. Eckert, Additive Manufacturing Processes: Selective Laser Melting, Electron Beam Melting and Binder Jetting—Selection Guidelines, Materials. 10 (2017) 672. https://doi.org/10.3390/ma10060672.

[14] L.A. Dobrzanski, A.D. Dobrzanska-Danikiewicz, A. Achtelik-Franczak, L.B. Dobrzanski, M. Szindler, T.G. Gawel, Porous Selective Laser Melted Ti and Ti6Al4V Materials for Medical Applications, in: L.A. Dobrzanski (Ed.), Powder Metall. - Fundam. Case Stud., InTech, 2017. https://doi.org/10.5772/65375.

[15] J.H. Tan, W.L.E. Wong, K.W. Dalgarno, An overview of powder granulometry on feedstock and part performance in the selective laser melting process, Addit. Manuf. 18 (2017) 228–255. https://doi.org/10.1016/j.addma.2017.10.011.

[16] S. Pillot, Fusion laser sélective de lit de poudres métalliques, Tech. Ing. (2016) 25.

[17] B. Liu, R. Wildman, C. Tuck, I. Ashcroft, R. Hague, Investigation the effect of particle size distribution on processing parameters optimisation in Selective Laser Melting process, in: 22nd Annu. Int. Solid Free. Fabr. Symp. - Addit. Manuf. Conf., 2011: p. 12.

[18] W. Shi, Y. Liu, X. Shi, Y. Hou, P. Wang, G. Song, Beam Diameter Dependence of Performance in Thick-Layer and High-Power Selective Laser Melting of Ti-6Al-4V, Materials. 11 (2018) 1237. https://doi.org/10.3390/ma11071237.

[19] J. Metelkova, Y. Kinds, K. Kempen, C. de Formanoir, A. Witvrouw, B. Van Hooreweder, On the influence of laser defocusing in Selective Laser Melting of 316L, Addit. Manuf. 23 (2018) 161–169. https://doi.org/10.1016/j.addma.2018.08.006.
[20] E. Yasa, J. Deckers, J. Kruth, The investigation of the influence of laser re-melting on density, surface quality and microstructure of selective laser melting parts, Rapid Prototyp. J. 17 (2011) 312–327. https://doi.org/10.1108/13552541111156450.
[21] M. Nozar, I. Zetkova, O. Hronek, Searching for Favourable Powder Bed Fusion Settings in Sintering of Maraging Steel MS1, DAAAM Proc. (2018) 0777–0785. https://doi.org/10.2507/29th.daaam.proceedings.113.
[22] Z. Dong, Y. Liu, W. Wen, J. Ge, J. Liang, Effect of Hatch Spacing on Melt Pool and As-built Quality During Selective Laser Melting of Stainless Steel: Modeling and Experimental Approaches, Materials. 12 (2018) 50. https://doi.org/10.3390/ma12010050.
[23] F. Geiger, K. Kunze, T. Etter, Tailoring the texture of IN738LC processed by selective laser melting (SLM) by specific scanning strategies, Mater. Sci. Eng. A. 661 (2016) 240–246. https://doi.org/10.1016/j.msea.2016.03.036.
[24] H. Ali, H. Ghadbeigi, K. Mumtaz, Effect of scanning strategies on residual stress and mechanical properties of Selective Laser Melted Ti6Al4V, Mater. Sci. Eng. A. 712 (2018) 175–187. https://doi.org/10.1016/j.msea.2017.11.103.
[25] L. Bian, N. Shamsaei, J. Usher, eds., Laser-based additive manufacturing of metal parts: modeling, optimization, and control of mechanical properties, CRC Press, Taylor & Francis Group, Boca Raton, 2018.
[26] B. Vayssette, N. Saintier, C. Brugger, M. Elmay, E. Pessard, Surface roughness of Ti-6Al-4V parts obtained by SLM and EBM: Effect on the High Cycle Fatigue life, Procedia Eng. 213 (2018) 89–97. https://doi.org/10.1016/j.proeng.2018.02.010.
[27] D. Wang, Y. Liu, Y. Yang, D. Xiao, Theoretical and experimental study on surface roughness of 316L stainless steel metal parts obtained through selective laser melting, Rapid Prototyp. J. 22 (2016) 706–716. https://doi.org/10.1108/RPJ-06-2015-0078.
[28] E. Liverani, S. Toschi, L. Ceschini, A. Fortunato, Effect of selective laser melting (SLM) process parameters on microstructure and mechanical properties of 316L austenitic stainless steel, J. Mater. Process. Technol. 249 (2017) 255–263. https://doi.org/10.1016/j.jmatprotec.2017.05.042.
[29] P. Krakhmalev, I. Yadroitsava, G. Fredriksson, I. Yadroitsev, Microstructural and thermal stability of selective laser melted 316L stainless steel single tracks, South Afr. J. Ind. Eng. 28 (2017). https://doi.org/10.7166/28-1-1466.
[30] K. Saeidi, L. Kevetkova, F. Lofaj, Z. Shen, Novel ferritic stainless steel formed by laser melting from duplex stainless steel powder with advanced mechanical properties and high ductility, Mater. Sci. Eng. A. 665 (2016) 59–65. https://doi.org/10.1016/j.msea.2016.04.027.
[31] K. Saeidi, F. Akhtar, Subgrain-controlled grain growth in the laser-melted 316 L promoting strength at high temperatures, R. Soc. Open Sci. 5 (2018) 172394. https://doi.org/10.1098/rsos.172394.
[32] H. Nöbauer, Residual stresses and distortions in austenitic stainless steel 316 L specimens manufactured by Selective Laser Melting, Master thesis, University west, 2018.
[33] I. Yadroitsev, I. Yadroitsava, Evaluation of residual stress in stainless steel 316L and Ti6Al4V samples produced by selective laser melting, Virtual Phys. Prototyp. 10 (2015) 67–76. https://doi.org/10.1080/17452759.2015.1026045.
[34] O. Andreau, I. Koutiri, P. Peyre, J.-D. Penot, N. Saintier, E. Pessard, T. De Terris, C. Dupuy, T. Baudin, Texture control of 316L parts by modulation of the melt pool morphology in selective laser melting, J. Mater. Process. Technol. 264 (2019) 21–31. https://doi.org/10.1016/j.jmatprotec.2018.08.049.
[35] F. Yan, W. Xiong, E. Faierson, Grain Structure Control of Additively Manufactured Metallic Materials, Materials. 10 (2017) 1260. https://doi.org/10.3390/ma10111260.

[36] T. Niendorf, S. Leuders, A. Riemer, H.A. Richard, T. Tröster, D. Schwarze, Highly Anisotropic Steel Processed by Selective Laser Melting, Metall. Mater. Trans. B. 44 (2013) 794–796. https://doi.org/10.1007/s11663-013-9875-z.
[37] A.A. Antonysamy, J. Meyer, P.B. Prangnell, Effect of build geometry on the β-grain structure and texture in additive manufacture of Ti6Al4V by selective electron beam melting, Mater. Charact. 84 (2013) 153–168. https://doi.org/10.1016/j.matchar.2013.07.012.
[38] S. Cheruvathur, E.A. Lass, C.E. Campbell, Additive Manufacturing of 17-4 PH Stainless Steel: Post-processing Heat Treatment to Achieve Uniform Reproducible Microstructure, JOM. 68 (2016) 930–942. https://doi.org/10.1007/s11837-015-1754-4.
[39] Y.M. Wang, T. Voisin, J.T. McKeown, J. Ye, N.P. Calta, Z. Li, Z. Zeng, Y. Zhang, W. Chen, T.T. Roehling, R.T. Ott, M.K. Santala, P.J. Depond, M.J. Matthews, A.V. Hamza, T. Zhu, Additively manufactured hierarchical stainless steels with high strength and ductility, Nat. Mater. 17 (2018) 63–71. https://doi.org/10.1038/nmat5021.
[40] F. Hengsbach, P. Koppa, K. Duschik, M.J. Holzweissig, M. Burns, J. Nellesen, W. Tillmann, T. Tröster, K.-P. Hoyer, M. Schaper, Duplex stainless steel fabricated by selective laser melting - Microstructural and mechanical properties, Mater. Des. 133 (2017) 136–142. https://doi.org/10.1016/j.matdes.2017.07.046.
[41] S. Gorsse, C. Hutchinson, M. Gouné, R. Banerjee, Additive manufacturing of metals: a brief review of the characteristic microstructures and properties of steels, Ti-6Al-4V and high-entropy alloys, Sci. Technol. Adv. Mater. 18 (2017) 584–610. https://doi.org/10.1080/14686996.2017.1361305.
[42] E. Yasa, J.-P. Kruth, Microstructural investigation of Selective Laser Melting 316L stainless steel parts exposed to laser re-melting, Procedia Eng. 19 (2011) 389–395. https://doi.org/10.1016/j.proeng.2011.11.130.
[43] G. Kasperovich, J. Haubrich, J. Gussone, G. Requena, Correlation between porosity and processing parameters in TiAl6V4 produced by selective laser melting, Mater. Des. 105 (2016) 160–170. https://doi.org/10.1016/j.matdes.2016.05.070.
[44] C.N. Hsiao, C.S. Chiou, J.R. Yang, Aging reactions in a 17-4 PH stainless steel, Mater. Chem. Phys. 74 (2002) 134–142. https://doi.org/10.1016/S0254-0584(01)00460-6.
[45] F. Christien, M.T.F. Telling, K.S. Knight, A comparison of dilatometry and in-situ neutron diffraction in tracking bulk phase transformations in a martensitic stainless steel, Mater. Charact. 82 (2013) 50–57. https://doi.org/10.1016/j.matchar.2013.05.002.
[46] F. Christien, M.T.F. Telling, K.S. Knight, Neutron diffraction in situ monitoring of the dislocation density during martensitic transformation in a stainless steel, Scr. Mater. 68 (2013) 506–509. https://doi.org/10.1016/j.scriptamat.2012.11.031.
[47] W.D. Yoo, J.H. Lee, K.T. Youn, Y.M. Rhyim, Study on the Microstructure and Mechanical Properties of 17-4 PH Stainless Steel Depending on Heat Treatment and Aging Time, Solid State Phenom. 118 (2006) 15–20. https://doi.org/10.4028/www.scientific.net/SSP.118.15.
[48] U.K. Viswanathan, S. Banerjee, R. Krishnan, Effects of aging on the microstructure of 17-4 PH stainless steel, Mater. Sci. Eng. A. 104 (1988) 181–189. https://doi.org/10.1016/0025-5416(88)90420-X.
[49] M. Murayama, K. Hono, Y. Katayama, Microstructural evolution in a 17-4 PH stainless steel after aging at 400 C, Metall. Mater. Trans. A. 30 (1999) 345–353.
[50] F. Christien, Fragilité intergranulaire de l'acier 17-4 PH en cours de vieillissement, PhD Thesis, Université de Nantes, 2001.
[51] G. Yeli, M.A. Auger, K. Wilford, G.D.W. Smith, P.A.J. Bagot, M.P. Moody, Sequential nucleation of phases in a 17-4PH steel: Microstructural characterisation and mechanical properties, Acta Mater. 125 (2017) 38–49. https://doi.org/10.1016/j.actamat.2016.11.052.
[52] J. Wang, H. Zou, C. Li, S. Qiu, B. Shen, The effect of microstructural evolution on hardening behavior of type 17-4PH stainless steel in long-term aging at 350 °C, Mater. Charact. 57 (2006) 274–280. https://doi.org/10.1016/j.matchar.2006.02.004.

[53] R. Bhambroo, S. Roychowdhury, V. Kain, V.S. Raja, Effect of reverted austenite on mechanical properties of precipitation hardenable 17-4 stainless steel, Mater. Sci. Eng. A. 568 (2013) 127–133. https://doi.org/10.1016/j.msea.2013.01.011.
[54] R.J. Hamlin, J.N. DuPont, Microstructural Evolution and Mechanical Properties of Simulated Heat-Affected Zones in Cast Precipitation-Hardened Stainless Steels 17-4 and 13-8+Mo, Metall. Mater. Trans. A. 48 (2017) 246–264. https://doi.org/10.1007/s11661-016-3851-6.
[55] R. Kapoor, I.S. Batra, On the α' to γ transformation in maraging (grade 350), PH 13-8 Mo and 17-4 PH steels, Mater. Sci. Eng. A. 371 (2004) 324–334. https://doi.org/10.1016/j.msea.2003.12.023.
[56] A. Ziewiec, A. ZieliŃska-Lipiec, E. Tasak, Microstructure of Welded Joints of X5CrNiCuNb16-4 (17-4 PH) Martensitic Stainlees Steel After Heat Treatment, Arch. Metall. Mater. 59 (2014). https://doi.org/10.2478/amm-2014-0162.
[57] A. Mondelin, F. Valiorgue, M. Coret, E. Feulvarch, J. Rech, Surface integrity prediction in finish turning of 15-5PH stainless steel, Procedia Eng. 19 (2011) 270–275. https://doi.org/10.1016/j.proeng.2011.11.111.
[58] H.J. Rack, Physical and mechanical properties of cast 17-4 PH stainless steel, 1981. https://doi.org/10.2172/6607517.
[59] L.E. Murr, E. Martinez, J. Hernandez, S. Collins, K.N. Amato, S.M. Gaytan, P.W. Shindo, Microstructures and Properties of 17-4 PH Stainless Steel Fabricated by Selective Laser Melting, J. Mater. Res. Technol. 1 (2012) 167–177. https://doi.org/10.1016/S2238-7854(12)70029-7.
[60] H.K. Rafi, D. Pal, N. Patil, T.L. Starr, B.E. Stucker, Microstructure and Mechanical Behavior of 17-4 Precipitation Hardenable Steel Processed by Selective Laser Melting, J. Mater. Eng. Perform. 23 (2014) 4421–4428. https://doi.org/10.1007/s11665-014-1226-y.
[61] T.L. Starr, K. Rafi, B. Stucker, C.M. Scherzer, Controlling phase composition in Selective Laser Melted stainless steels, in: 23rd Annu. Int. Solid Free. Fabr. Symp. - Addit. Manuf. Conf., 2012: p. 8.
[62] J.R. Davis, ASM International, eds., in: Stainl. Steels, ASM International, Materials Park, Ohio, 1994: pp. 3–5.
[63] J.H. Qiu, Passivity and its breakdown on stainless steels and alloys, Surf Interface Anal. 33 (2002) 830–833. https://doi.org/10.1002/sia.1460.
[64] B. Baroux, Y. Bréchet, J. Charles, La corrosion des métaux passivité et corrosion localisée, L'Usine nouvelle : Dunod, Paris, 2014.
[65] C.-O.A. Olsson, D. Landolt, Passive films on stainless steels—chemistry, structure and growth, Electrochimica Acta. 48 (2003) 1093–1104. https://doi.org/10.1016/S0013-4686(02)00841-1.
[66] T. Ohtsuka, A. Nishikata, M. Sakairi, K. Fushimi, Electrochemistry for Corrosion Fundamentals, Springer Singapore, Singapore, 2018. https://doi.org/10.1007/978-981-10-6820-1.
[67] S. ghunaim Al-Subai, Corrosion resistance of austenitic stainless steel in acetic acid solution containing bromide ions, PhD Thesis, University of Manchester, 2011.
[68] E. Bardal, ed., Different Forms of Corrosion Classified on the Basis of Appearence, in: Corros. Prot., Springer London, London, 2004: pp. 89–191. https://doi.org/10.1007/978-1-85233-845-9_7.
[69] M.B. Ives, Metallography of pitting corrosion, Mater. Charact. 28 (1992) 257–270. https://doi.org/10.1016/1044-5803(92)90015-A.
[70] Y.S. Jiménez, M.T. Gil, M.T. Guerra, L. Baltes, J.C.M. Rosca, Interpretation of open circuit potential of two Titanium alloys for a long time immersion in physiological fluid, Bull Trans Uni Brasov. 2 (2009).
[71] G. DAUFIN, J. Talbot, Etude de quelques problèmes de corrosion dans l'industrie laitière. Première partie: Généralités sur la corrosion des métaux et alliages, Le Lait. 51 (1971) 375–398.
[72] D.G. Enos, The Potentiodynamic Polarization Scan, University of Virginia, 1997.
[73] P. Marcus, ed., Corrosion mechanisms in theory and practice, 2nd ed., rev.expanded, Marcel Dekker, New York, 2002.

[74] Q. Chao, V. Cruz, S. Thomas, N. Birbilis, P. Collins, A. Taylor, P.D. Hodgson, D. Fabijanic, On the enhanced corrosion resistance of a selective laser melted austenitic stainless steel, Scr. Mater. 141 (2017) 94–98. https://doi.org/10.1016/j.scriptamat.2017.07.037.
[75] S.-H. Sun, T. Ishimoto, K. Hagihara, Y. Tsutsumi, T. Hanawa, T. Nakano, Excellent mechanical and corrosion properties of austenitic stainless steel with a unique crystallographic lamellar microstructure via selective laser melting, Scr. Mater. 159 (2019) 89–93. https://doi.org/10.1016/j.scriptamat.2018.09.017.
[76] M.J.K. Lodhi, K.M. Deen, W. Haider, Corrosion behavior of additively manufactured 316L stainless steel in acidic media, Materialia. (2018). https://doi.org/10.1016/j.mtla.2018.06.015.
[77] Y. Sun, A. Moroz, K. Alrbaey, Sliding Wear Characteristics and Corrosion Behaviour of Selective Laser Melted 316L Stainless Steel, J. Mater. Eng. Perform. 23 (2014) 518–526. https://doi.org/10.1007/s11665-013-0784-8.
[78] G. Sander, S. Thomas, V. Cruz, M. Jurg, N. Birbilis, X. Gao, M. Brameld, C.R. Hutchinson, On The Corrosion and Metastable Pitting Characteristics of 316L Stainless Steel Produced by Selective Laser Melting, J. Electrochem. Soc. 164 (2017) C250–C257. https://doi.org/10.1149/2.0551706jes.
[79] Y. Zhang, F. Liu, J. Chen, Y. Yuan, Effects of surface quality on corrosion resistance of 316L stainless steel parts manufactured via SLM, J. Laser Appl. 29 (2017) 022306. https://doi.org/10.2351/1.4983263.
[80] J.R. Trelewicz, G.P. Halada, O.K. Donaldson, G. Manogharan, Microstructure and Corrosion Resistance of Laser Additively Manufactured 316L Stainless Steel, JOM. 68 (2016) 850–859. https://doi.org/10.1007/s11837-016-1822-4.
[81] M. Kazemipour, A. Nasiri, M. Mohammadi, On Microstructure and Corrosion Properties of Selective Laser Melted 316L Stainless Steel, in: Prog. Can. Mech. Eng., York University Libraries, 2018. https://doi.org/10.25071/10315/35428.
[82] U.K. Mudali, A.K. Bhaduri, J.B. Gnanamoorthy, Localised corrosion behaviour of 17–4 PH stainless steel, Mater. Sci. Technol. 6 (1990) 7. https://doi.org/10.1179/mst.1990.6.5.475.
[83] B.C. Syrett, R. Viswanathan, S.S. Wing, J.E. Wittig, Effect of Microstructure on Pitting and Corrosion Fatigue of 17-4 PH Turbine Blade Steel in Chloride Environments, CORROSION. 38 (1982) 273–282. https://doi.org/10.5006/1.3577350.
[84] M.R. Stoudt, R.E. Ricker, E.A. Lass, L.E. Levine, Influence of Postbuild Microstructure on the Electrochemical Behavior of Additively Manufactured 17-4 PH Stainless Steel, JOM. 69 (2017) 506–515. https://doi.org/10.1007/s11837-016-2237-y.
[85] R.F. Schaller, J.M. Taylor, J. Rodelas, E.J. Schindelholz, Corrosion Properties of Powder Bed Fusion Additively Manufactured 17-4 PH Stainless Steel, CORROSION. 73 (2017) 796–807. https://doi.org/10.5006/2365.
[86] H. Irrinki, T. Harper, S. Badwe, J. Stitzel, O. Gulsoy, G. Gupta, S.V. Atre, Effects of powder characteristics and processing conditions on the corrosion performance of 17-4 PH stainless steel fabricated by laser-powder bed fusion, Prog. Addit. Manuf. 3 (2018) 39–49. https://doi.org/10.1007/s40964-018-0048-0.
[87] V.S. Raja, T. Shoji, Stress corrosion cracking, Theory and practice, Woodhead Publishing Limited, Cambridge, 2011.
[88] S.K. Dwivedi, M. Vishwakarma, Hydrogen embrittlement in different materials: A review, Int. J. Hydrog. Energy. 43 (2018) 21603–21616. https://doi.org/10.1016/j.ijhydene.2018.09.201.
[89] N. Amokrane, Etude de l'adsorption et l'absorption de l'hydrogène formé par voie électrochimique sur différents métaux, PhD Thesis, Université Paris 6, 2007.
[90] E. Protopopoff, P. Marcus, Surface Effects on Hydrogen Entry into Metals, in: Corros. Mech. Theory Pract., 2nd ed., 2002: pp. 53–96.
[91] E.G. Dafft, K. Bohnenkamp, H.J. Engell, Investigations of the hydrogen evolution kinetics and hydrogen absorption by iron electrodes during cathodic polarization, Corros. Sci. 19 (1979) 591–612. https://doi.org/10.1016/S0010-938X(79)80061-X.

[92] H. Mehrer, Diffusion in solids: Fundamentals, methods, materials, diffusion-controlled process, Springer series in solid state science, 2007. 10.1007/978-3-540-71488-0.
[93] A.-M. Brass, J. Chêne, L. Coudreuse, Fragilisation des aciers par l'hydrogène : mécanismes, Tech. Ing. (2000) 15.
[94] A.M. Brass, A. Chanfreau, Accelerated diffusion of hydrogen along grain boundaries in nickel, Acta Mater. 44 (1996) 3823–3831. https://doi.org/10.1016/1359-6454(95)00446-7.
[95] P. Bastien, P. Azou, Influence de l'hydrogène sur les caractéristiques de déformation et de rupture par traction du fer et de l'acier, Rev. Métallurgie. 49 (1952) 837–848. https://doi.org/10.1051/metal/195249120837.
[96] J. Tien, A.W. Thompson, I.M. Bernstein, R.J. Richards, Hydrogen transport by dislocations, Metall. Trans. A. 7 (1976) 821–829. https://doi.org/10.1007/BF02644079.
[97] D. Guedes, A. Oudriss, S. Cohendoz, J. Creus, J. Bouhattate, X. Feaugas, F. Thebault, D. Koschel, The Influence of Hydrogen Flux on Crack Initiation in Martensitic Steels, Procedia Mater. Sci. 3 (2014) 2024–2029. https://doi.org/10.1016/j.mspro.2014.06.326.
[98] H. Shoda, H. Suzuki, K. Takai, Y. Hagihara, Hydrogen Desorption Behavior of Pure Iron and Inconel 625 during Elastic and Plastic Deformation, ISIJ Int. 50 (2010) 115–123. https://doi.org/10.2355/isijinternational.50.115.
[99] J. Chêne, A.M. Brass, Hydrogen transport by mobile dislocations in nickel base superalloy single crystals, Scr. Mater. 40 (1999) 537–542. https://doi.org/10.1016/S1359-6462(98)00451-5.
[100] G.M. Pressouyre, Trap theory of Hydrogen embrittlement, Acta Metall. 28 (1980) 895–911. https://doi.org/10.1016/0001-6160(80)90106-6.
[101] A.H.M. Krom, A. Bakker, Hydrogen trapping models in steel, Metall. Mater. Trans. B. 31 (2000) 1475–1482. https://doi.org/10.1007/s11663-000-0032-0.
[102] R.A. Oriani, A mechanistic theory of hydrogen embrittlement of steels, Berichte Bunsenges. Für Phys. Chem. 76 (1972) 10. https://doi.org/10.1002/bbpc.19720760864.
[103] A.R. Troiano, The Role of Hydrogen and Other Interstitials in the Mechanical Behavior of Metals: (1959 Edward De Mille Campbell Memorial Lecture), Metallogr. Microstruct. Anal. 5 (2016) 557–569. https://doi.org/10.1007/s13632-016-0319-4.
[104] C.D. Beachem, A new model for hydrogen-assisted cracking (hydrogen "embrittlement"), Metall. Mater. Trans. B. 3 (1972) 441–455. https://doi.org/10.1007/BF02642048.
[105] S.P. Lynch, Environmentally assisted cracking: Overview of evidence for an adsorption-induced localised-slip process, Acta Metall. 36 (1988) 2639–2661. https://doi.org/10.1016/0001-6160(88)90113-7.
[106] E. Malitckii, Y. Yagodzinskyy, P. Lehto, H. Remes, J. Romu, H. Hänninen, Hydrogen effects on mechanical properties of 18%Cr ferritic stainless steel, Mater. Sci. Eng. A. 700 (2017) 331–337. https://doi.org/10.1016/j.msea.2017.06.028.
[107] S. Konosu, T. Nakaniwa, Hydrogen cracking of ferritic stainless steel thermal storage tanks, Eng. Fail. Anal. 5 (1998) 323–331.
[108] S.P. Trasatti, E. Sivieri, F. Mazza, Susceptibility of a X80 steel to hydrogen embrittlement, Mater. Corros. 56 (2005) 111–117. https://doi.org/10.1002/maco.200403821.
[109] T. Neeraj, R. Srinivasan, J. Li, Hydrogen embrittlement of ferritic steels: Observations on deformation microstructure, nanoscale dimples and failure by nanovoiding, Acta Mater. 60 (2012) 5160–5171. https://doi.org/10.1016/j.actamat.2012.06.014.
[110] S. Shen, X. Song, Q. Li, X. Li, R. Zhu, G. Yang, A study on stress corrosion cracking and hydrogen embrittlement of Jethete M152 martensitic stainless steel, Mater. Sci. Eng. A. 740–741 (2019) 243–251. https://doi.org/10.1016/j.msea.2018.10.091.
[111] C.L. Lai, L.W. Tsay, C. Chen, Effect of microstructure on hydrogen embrittlement of various stainless steels, Mater. Sci. Eng. A. 584 (2013) 14–20. https://doi.org/10.1016/j.msea.2013.07.004.
[112] B.D. Craig, G. Krauss, The structure of tempered martensite and its susceptibility to hydrogen stress cracking, Metall. Trans. A. 11 (1980) 1799–1808. https://doi.org/10.1007/BF02655095.

[113] J. Lee, T. Lee, Y.J. Kwon, D.-J. Mun, J.-Y. Yoo, C.S. Lee, Role of Mo/V carbides in hydrogen embrittlement of tempered martensitic steel, Corros. Rev. 33 (2015). https://doi.org/10.1515/corrrev-2015-0052.
[114] A. Nagao, M.L. Martin, M. Dadfarnia, P. Sofronis, I.M. Robertson, The effect of nanosized (Ti,Mo)C precipitates on hydrogen embrittlement of tempered lath martensitic steel, Acta Mater. 74 (2014) 244–254. https://doi.org/10.1016/j.actamat.2014.04.051.
[115] J.S. Kim, Y.H. Lee, D.L. Lee, K.-T. Park, C.S. Lee, Microstructural influences on hydrogen delayed fracture of high strength steels, Mater. Sci. Eng. A. 505 (2009) 105–110. https://doi.org/10.1016/j.msea.2008.11.040.
[116] D. Sasaki, M. Koyama, H. Noguchi, Factors affecting hydrogen-assisted cracking in a commercial tempered martensitic steel: Mn segregation, MnS, and the stress state around abnormal cracks, Mater. Sci. Eng. A. 640 (2015) 72–81. https://doi.org/10.1016/j.msea.2015.05.083.
[117] M. Beghini, G. Benamati, L. Bertini, I. Ricapito, R. Valentini, Effect of hydrogen on the ductility reduction of F82H martensitic steel after different heat treatments, J. Nucl. Mater. (2001) 6.
[118] Y. Momotani, A. Shibata, D. Terada, N. Tsuji, Effect of strain rate on hydrogen embrittlement in low-carbon martensitic steel, Int. J. Hydrog. Energy. 42 (2017) 3371–3379. https://doi.org/10.1016/j.ijhydene.2016.09.188.
[119] B. Bal, M. Koyama, G. Gerstein, H.J. Maier, K. Tsuzaki, Effect of strain rate on hydrogen embrittlement susceptibility of twinning-induced plasticity steel pre-charged with high-pressure hydrogen gas, Int. J. Hydrog. Energy. 41 (2016) 15362–15372. https://doi.org/10.1016/j.ijhydene.2016.06.259.
[120] T. Hojo, R. Kikuchi, H. Waki, F. Nishimura, Y. Ukai, E. Akiyama, Effect of Strain Rate on the Hydrogen Embrittlement Property of Ultra High-strength Low Alloy TRIP-aided Steel, ISIJ Int. 58 (2018) 751–759. https://doi.org/10.2355/isijinternational.ISIJINT-2017-576.
[121] T. Depover, A. Elmahdy, F. Vercruysse, P. Verleysen, K. Verbeken, Effect of strain rate on the hydrogen embrittlement of a DP steel, EPJ Web Conf. 183 (2018) 03015. https://doi.org/10.1051/epjconf/201818303015.
[122] J. Toribio, Effects of strain rate and notch geometry on hydrogen embrittlement of AISI type 316L austenitic stainless steel, Fusion Eng. Des. 16 (1991) 377–386. https://doi.org/10.1016/0920-3796(91)90213-A.
[123] N. Nanninga, J. Grochowsi, L. Heldt, K. Rundman, Role of microstructure, composition and hardness in resisting hydrogen embrittlement of fastener grade steels, Corros. Sci. 52 (2010) 1237–1246. https://doi.org/10.1016/j.corsci.2009.12.020.
[124] S. Brahimi, K. Sriraman, S. Yue, Hydrogen embrittlement characteristics of two tempered martensitic steel alloys for high-strength bolting, Proc. Inst. Mech. Eng. Part C J. Mech. Eng. Sci. 231 (2017) 3214–3227. https://doi.org/10.1177/0954406216642476.
[125] S.K. Bonagani, B. Vishwanadh, S. Tenneti, N. Naveen Kumar, V. Kain, Influence of tempering treatments on mechanical properties and hydrogen embrittlement of 13 wt% Cr martensitic stainless steel, Int. J. Press. Vessels Pip. 176 (2019) 103969. https://doi.org/10.1016/j.ijpvp.2019.103969.
[126] S.J. Hudak, R.P. Wei, Hydrogen enhanced crack growth in 18 Ni maraging steels, Metall. Trans. A. 7 (1976) 235–241. https://doi.org/10.1007/BF02644462.

Chapter 2 Evidence of austenite by-passing in a stainless steel obtained from laser melting additive manufacturing

Table of contents

(The work presented in this chapter was published in Additive Manufacturing in 2018)

2.1 Abstract

Microstructural characterization was carried out on AISI 17-4 PH stainless steel fabricated by selective laser melting (SLM) in an argon environment. Conventionally, this steel exhibits a martensitic structure with a small fraction of δ ferrite. However, the combined findings of x-ray diffraction and electron backscatter diffraction (EBSD) proved that SLM-ed 17-4 PH steel has a fully ferritic microstructure, more specifically δ ferrite. The microstructure consists of coarse ferritic grains elongated along the build direction, with a pronounced solidification crystallographic texture. These results were associated to the high cooling and heating rates experienced throughout the SLM process that suppressed the austenite formation and produced a "by-passing" phenomenon of this phase during the numerous thermal cycles. Furthermore, the energy-dispersive X-ray spectroscopy (EDS) measurements revealed a uniform distribution of elements without any dendritic structure. The extremely high cooling kinetics induced a diffusionless solidification, resulting in a homogeneous elemental composition. It was also found that the ferritic SLM-ed material can be transformed to martensite again by re-austenitization at 1050°C followed by quenching.

2.2 Introduction

Additive manufacturing (AM) has been rapidly developing in the past few years, because it allows 3D parts, often having a complex geometry, to be directly fabricated to a near-net-shape. It consists of constructing a part by adding material layer upon layer according to a CAD (Computer-aided design) model. In contrast to conventional "subtractive" methods, it requires little machining and finishing work, thus reducing waste to a minimum. AM refers to the process itself which incorporates several techniques [1–3]. One of these techniques is selective laser melting (SLM) that is based on powder bed fusion. Atomized metal powder is deposited on a substrate plate and selectively melted by a laser beam using CAD data. Subsequently, the building platform is lowered and another powder layer is re-deposited. The procedure repeats itself until reaching the required shape. Numerous construction parameters such as laser power and speed, scanning strategy and build chamber atmosphere, should be controlled in order to obtain a nearly fully dense functioning part [4–7]. Although this technology has progressed greatly, there are still various limitations. Among them can be cited: the limited number of materials that can be used, the poor surface quality and the resulting non-equilibrium microstructures. In addition, many reports revealed that some alloys processed by SLM presented highly anisotropic microstructures [8,9] that are sometimes greatly different from those obtained by conventional fabrication routes.

This study focuses on the microstructure of 17-4 PH stainless steel fabricated by SLM process. Wrought 17-4 PH steel is a martensitic precipitation hardenable stainless steel. It is widely used in a variety of applications such as aerospace, medical and food industries, due to its high strength and relatively good corrosion resistance. A solution heat treatment is usually applied in the austenitic domain (~1050°C), followed by quenching, to obtain a martensitic structure. In order to improve the mechanical properties, a subsequent tempering treatment in the range 480°-620°C is conducted that results in precipitation-hardening by copper precipitates [10–12]. Recent studies on this steel fabricated by SLM method have investigated the effect of multiple process parameters on material properties. According to Z. Hu et al. [13], the scan velocity and layer thickness were the key factors in controlling the material density at a fixed laser power. An interaction between these factors was also taken into account. Moreover, the building orientation had a great effect on mechanical properties. A. Yadollahi et al. found that the horizontal building orientation was more favorable because it allowed fewer defects to be formed by decreasing the number of deposited layers [14,15]. In addition, a change in phase constitution was reported by multiple authors that strongly depended on the chamber atmosphere. For instance, a significant fraction of retained austenite was found in this material when built in a chamber with nitrogen atmosphere, while in an argon purging environment, the microstructure was identified as mainly martensitic. It was deduced that the nitrogen had a strong stabilizing effect on the austenitic phase [16–19]. Moreover, besides the highly anisotropic and textured microstructure usually found in these materials, some investigations have revealed a dendritic/cellular structure with micro-segregation. It was attributed to the high cooling rates (10^5-10^6 K/s) experienced during SLM that led to non-equilibrium solidification conditions [18,19].

The existing literature on SLM-ed 17-4 PH steel mainly focused on the effect of process parameters on the resulting microstructures, especially the retained austenite. However, little attention was paid to this SLM-ed steel when having a fully body centered cubic structure. In this present work, a detailed microstructural characterization was conducted on SLM-ed 17-4 PH steel fabricated under argon atmosphere.

2.3 Experimental procedure

Microstructural analysis was carried out on both wrought and SLM-ed 17-4 PH stainless steel. The wrought material is commercial 17-4 PH steel from UGINE (cast # 818025). Parts were cut from a 15 mm diameter wrought rod bar. They were heat treated at 1050°C for an hour followed by water quenching, which led to a martensitic structure. The main study of SLM-ed material was done on a specimen having a cuboidal shape with dimensions 12x12x60 mm. It was fabricated using a selective laser melting machine (SLM 280 solution) under an argon purging atmosphere. Laser was operating at

a power of 275 W and a scanning speed of 760 mm/s. The powder layer thickness was approximately 50 µm and a scanning strategy of stripes was applied with a 90° rotation between layers. The build orientation was horizontal, meaning that the longitudinal axis of the cuboid was horizontal and parallel to the build platform (X-Y plane). Parts were cut from the specimen parallel (Y-Z plane) and perpendicular (X-Y plane) to the build direction Z. A schematic representation of the cuboid and its corresponding studied planes is given in **Figure 2. *1***. Note that the SLM-ed samples were studied both in the as-built condition and after a solution heat treatment (1050°C/1 hour + water quench). The chemical compositions for both wrought and SLM-ed 17-4 PH are given in **Table 2. *1***. For wrought material, the full composition of the cast is indicated (data from the steel provider) in the first line of **Table 2. *1***. Additional measurements were conducted in this study on both wrought and SLM-ed materials (lines 2 and 3 of **Table 2. *1***). These measurements were carried out using X-ray fluorescence (XRF) (FISCHERSCOPE X-Ray XAN-FD) for elements Ni, Cr and Cu, and using combustion elemental analysis (CEA) for C, S (LECO CS 444/LS), N and O (LECO TC-436).

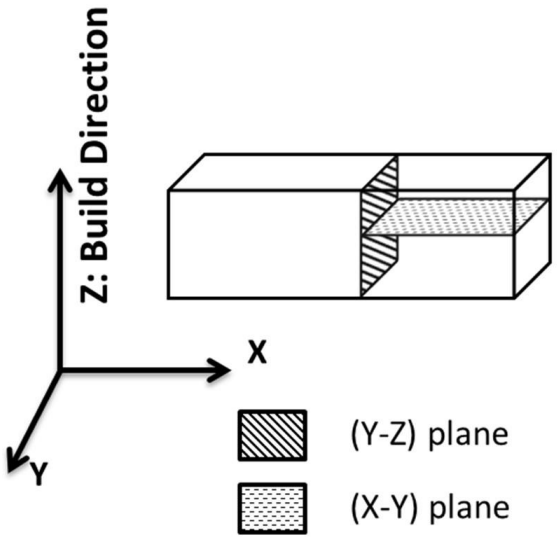

Figure 2. 1: Schematic representation of the build orientation and the planes where the microstructural characterization was carried out.

Phase identification was conducted in PANalytical's X'Pert PRO X-ray diffractometer using Cu Kα radiation. X-ray diffraction patterns were obtained in a 2Θ range of 40° to 120° with a step size of 0.04°. For optical microscopy, samples were polished to a mirror finish, and then etched with a modified Villela reagent (10 g picric acid + 10 ml hydrochloric acid + 8 ml acetic acid + 100 ml ethanol) for 30 s to reveal the martensitic microstructures. An electrochemical etching was also applied using concentrated nitric acid solution (50% HNO_3) at 2 V for 20 s to reveal the austenitic grain boundaries.

Regarding scanning electron microscopy (SEM) preparation, samples were polished up to 1200 grit, followed by electropolishing using 94% ethanol + 6% perchloric acid as electrolyte at 25 V for 60 s. SEM Zeiss SUPRA55VP was used for microstructural observations using electron backscatter diffraction (EBSD) operating at 20 kV. In addition, microchemical analysis was performed using energy dispersive spectroscopy (EDS). Dilatometric testing was carried out in a SETARAM dilatometer under argon atmosphere during continuous heating and cooling at a fixed rate of 5 K/min.

In order to ensure reproducibility, two other SLM-ed samples were studied by using EBSD and EDS techniques. They were fabricated in different machines (Machine 1: SLM solution 280 HL, machine 2: Concept Laser M2) but the same atmosphere (argon) was used as for the main SLM-ed specimen.

Table 2. 1 : Chemical composition (wt. %) of wrought and SLM-ed 17-4 PH stainless steel

17-4 PH		C	Ni	Si	P	Mn	Cr	Cu	S	N	O	Nb F	e
Wrought	Provider Data sheet	0.031	4.82	0.31	0.016	0.81	15.61	3.12	0.02	-	-	0.21	Bal.
	XRF/CEA	0.026	4.95	-	-	-	16.18	3.09	0.021	0.033	0.007	-	Bal.
SLM-ed	XRF/CEA	0.011	3.98	-	-	-	15.87	3.63	0.005	0.058	0.070	0.57	Bal.

2.4 Results and discussion

2.4.1 Microstructure of wrought 17-4 PH steel

The optical observation of wrought 17-4 PH steel revealed a typical lath martensite structure inside well defined prior austenitic grains as shown in ***Figure 2. 2.a***. The average size of the austenitic grains is approximately 18 µm. The inverse pole figure IPF map in ***Figure 2. 2.b*** shows the lathes of martensite gathered into different packets inside the same prior austenite grain. These packets are separated by grain boundaries having misorientation angles higher than 10°. As expected, the material has undergone a complete martensitic transformation upon quenching after a heat treatment at 1050°C.

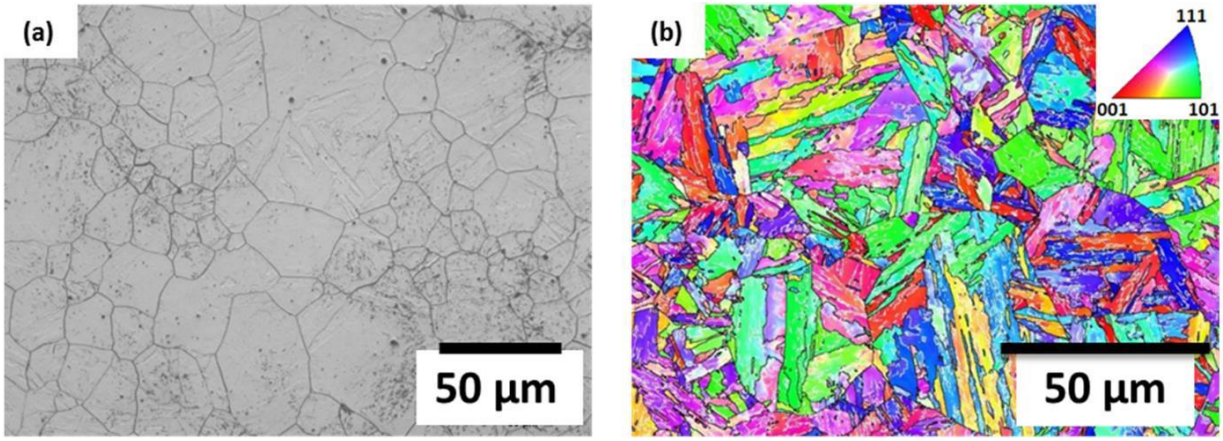

Figure 2. 2: (a) Optical micrograph and (b) EBSD orientation map (IPF Z) of wrought 17-4 PH steel showing a typical martensitic microstructure with a mean grain size of 18 µm.

2.4.2 Phase identification in as-built 17-4 PH steel

Figure 2. 3.a and .b show respectively the XRD diffraction patterns obtained from the planes (Y-Z) (parallel to the build direction) and (X-Y) (perpendicular to the build direction) for the as-built sample. It can be seen that in both planes the structure consists almost entirely of BCC phase with a small fraction of FCC austenite. The austenitic content is estimated to be less than 5%. It should be noted that the BCC phase can be attributed to either the martensite or ferrite, since the two phases cannot be distinguished by the XRD method. The martensite in stainless steels with a carbon content less than 0.2%, which is the case of 17-4 PH steel, has a BCC structure just as ferrite. Only for carbon content higher than 0.2% the martensite becomes slightly quadratic [20]. Furthermore, the peak intensity differences between the two planes (Y-Z) and (X-Y) show that the material is crystallographically textured.

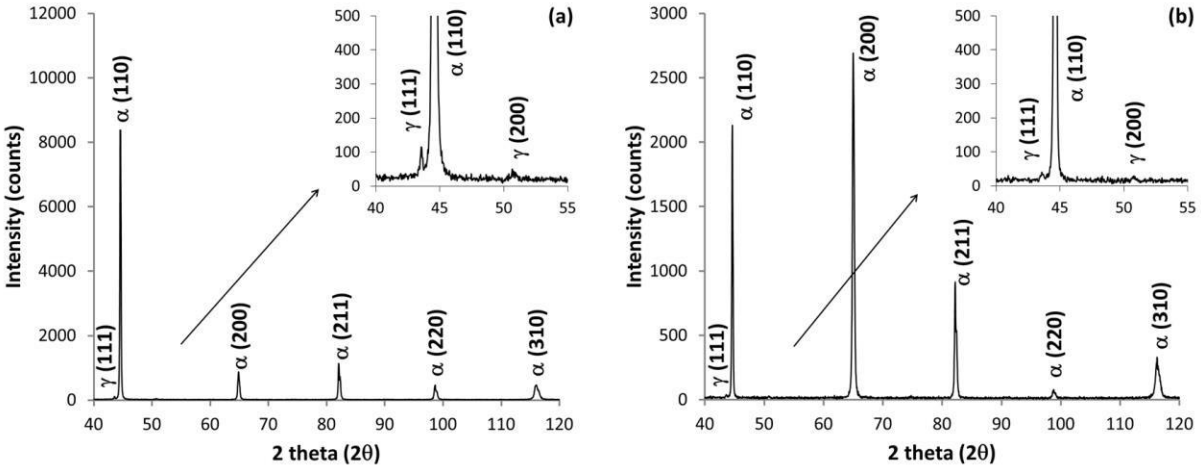

Figure 2. 3: XRD patterns of as-built 17-4 PH steel (a) in the (Y-Z) plane parallel to the build direction and (b) in the (X-Y) plane perpendicular to the build direction.

2.4.3 Microstructure of as-built 17-4 PH steel

The optical micrographs and EBSD orientation maps of the as-built 17-4 PH sample in the planes (Y-Z) and (X-Y) are shown respectively in **Figure 2. *4*** and **Figure 2. *5***. Both planes reveal a coarse grain microstructure with no presence of lathes of martensite, nor presence of any other large misorientations within the grains, which could be characteristic of a martensitic microstructure. The as-built 17-4 PH steel observed here doesn't have a martensitic structure. This contradicts with the existing literature [14,16,18] where the authors had the same observations (optical and EBSD) of the SLM-ed 17-4 PH steel fabricated in an argon environment, but considered the BCC phase to be martensite. As demonstrated using X-ray diffraction earlier (par. 3.2), this material consists mainly of a BCC phase which could either be martensite or ferrite. Thus the combined XRD and EBSD observations directly imply that this material has a fully ferritic BCC microstructure. In a similar manner, some studies reported a fully ferritic microstructure of duplex stainless steels in the as-built condition compared with their conventional dual phase structure (ferrite + austenite) [21,22]. This shows that the austenite by-passing effect observed here is also possible on other types of steels.

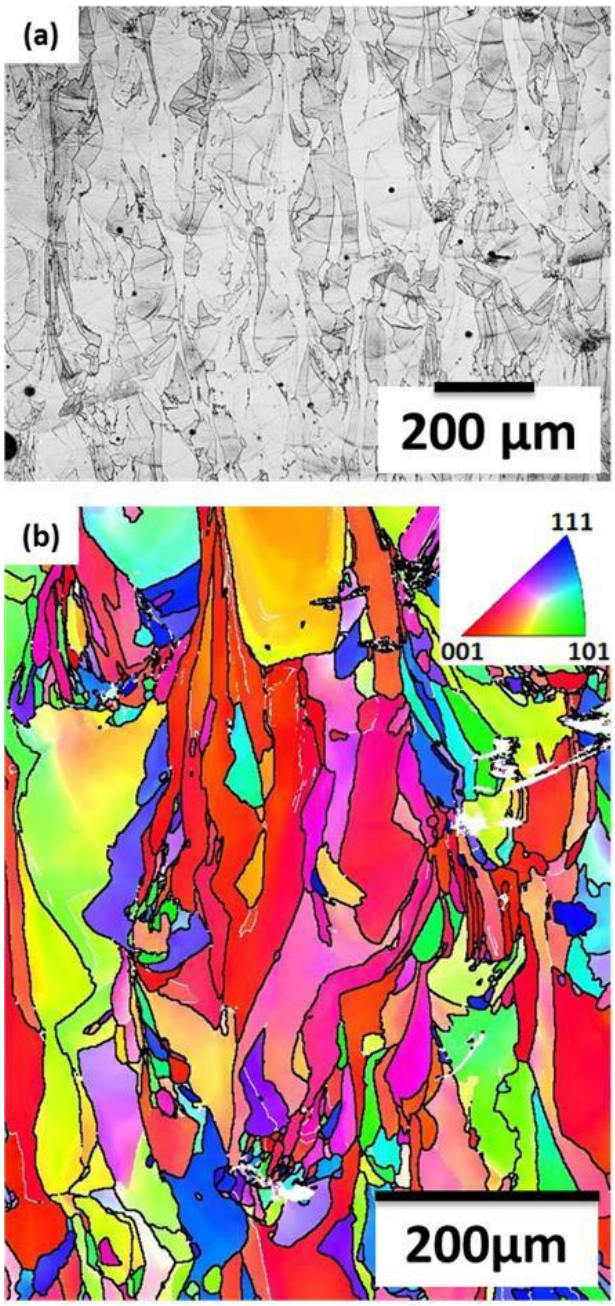

Figure 2. 4: (a) Optical micrograph and (b) EBSD orientation map (IPF Z) of as-built 17-4 PH steel in the (Y-Z) plane showing coarse grains with epitaxial growth in the build direction.

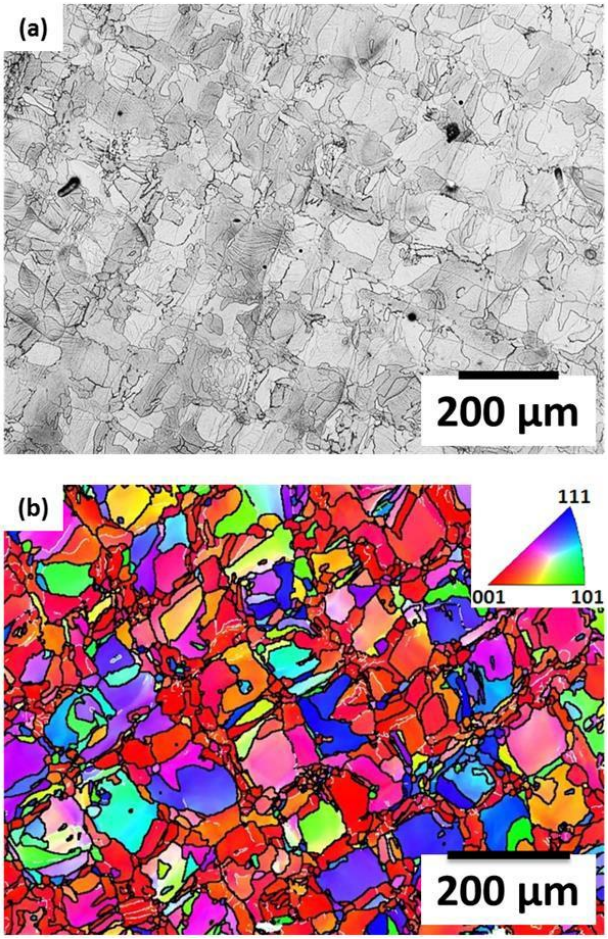

Figure 2. 5: (a) Optical micrograph and (b) EBSD orientation map (IPF Z) of as-built 17-4 PH steel in the (X-Y) plane showing coarse grain microstructure.

In order to fully understand this observed microstructure, the metallurgical evolution of this steel was analyzed. According to the Fe-Cr-Ni alloy equilibrium phase diagram [23], this steel solidifies as primary δ-ferrite, then the ferrite fully transforms into austenite and upon further cooling the martensitic transformation occurs. However, given the extremely high cooling rates (10^5-10^6 K/s) reached by SLM process, this phase sequence is no longer valid. Several authors have investigated the solidification microstructure of stainless steels under rapid cooling. They pointed out a change in primary solidification mode from that predicted by using the ratio of the chromium equivalent to the nickel equivalent (Cr_{eq}/Ni_{eq}) [24–26]. It was found that the solidification mode not only was controlled by this ratio but also by solidification growth rate and thermal gradient. Nonetheless, considering the SLM solidification parameters, the 17-4 PH melt pool is still predicted to solidify as 100% ferrite.

Regarding the possible transformation in the solid state, some welding investigations [27–29] on 17-4 PH steel reported an increase in the amount of retained δ ferrite with respect to the solution

annealed state. They concluded that the transformation of δ ferrite to austenite was not complete because of the high cooling rates experienced during welding, which are usually in the range 10^1-10^4 K/s [30–32]. However the SLM cooling rates are 1 to 2 orders of magnitude higher than those of welding. This implies that the transformation δ ferrite → γ austenite doesn't have enough time to occur. Thus, δ (BCC) ferrite passes rapidly through the austenite (FCC) stability temperature range without transforming until reaching the stability range of the BCC phase (below ~ 600°C for this steel). No further transformation is then expected, since δ ferrite is thermodynamically stable at low temperature. The phenomenon can be visualized as if δ ferrite had by-passed the FCC phase.

In addition, the solidified pools will encounter several thermal cycles, as illustrated in **Figure 2. *6***, which is due to adjacent laser scans and the melting of upper layers. A partial re-melting of the pool upon the first subsequent layers can also occur. As shown in **Figure 2. *6***, the peak temperature of the first cycles is far above the phase transformation start temperature from BCC to austenite FCC during heating (Ac1) (around ~ 600°C for this steel). Hence, the transformation might still occur. However, by taking a rate of 10^5 K/s, the maximum time spent in the FCC stability range is approximately 6 ms during heating or cooling. For kinetic reasons, this short time is supposed to be insufficient to allow austenite formation. Furthermore, according to a study [33], an increase in heating rate led to a shift of Ac1 to higher temperatures. This means that this time is even smaller than 6 ms. Moreover, a model was developed by Mondelin [34] on a similar martensitic stainless steel, which calculated the amount of transformed austenite depending on heating and cooling kinetics, by using data from dilatometric testing. Even though his model overestimated the austenitization kinetics [35], it still predicted a negligible amount of transformed austenite under SLM thermal rates (10^5-10^6 K/s). In the light of these findings, it is deduced that during these thermal cycles, either during heating or cooling, the same by-passing phenomenon is assumed to take place due to the insufficient time spent in the FCC stability range, which resulted in this observed ferritic microstructure at the end of SLM process.

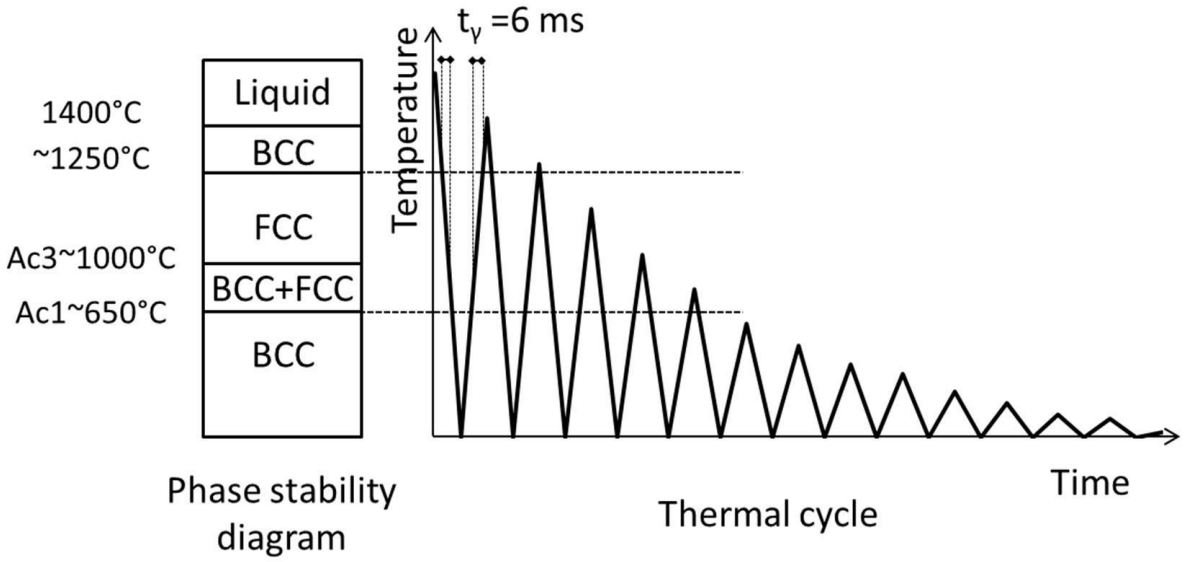

Figure 2. 6: Schematic representation of a thermal cycle of a melt pool during SLM and the phase stability diagram of 17-4 PH steel showing that the time spent by the material in the austenite stability range is very short (6 ms), both upon cooling and heating (Ac1 and Ac3 are respectively the transformation start and finish temperatures from BCC to FCC during heating).

Furthermore, another remarkable microstructural feature related to the grain morphology can be withdrawn from the orientation maps. In **Figure 2. *4***, the grains are seen elongated in the build direction following the vertical thermal gradient between the melt pool and the solidified lower layers. These columnar shaped grains can reach a length of some hundreds of µm, thus extending over several powder layers. This can be visualized in ***Figure 2. 4.a***, where the grains cross several melt pool boundaries made distinctly visible by etching. This means that during the molten pool solidification, the freshly formed crystals will have an epitaxial growth by adopting the orientation of the lower previously formed grains. It should be noted that depending on the input energy, the molten pool may include a part or the entire previous layer. Moreover in **Figure 2. *5***, the plane perpendicular to build direction shows grains having a relatively geometric structure that can be associated to the laser scanning strategy. This grain morphology was also observed by K. Saeidi et al. [22] on a duplex stainless steel obtained by SLM using a similar scanning strategy and was described as a mosaic-type structure.

In order to ensure reproducibility of these results, other specimens of as-built 17-4 PH steel fabricated under argon atmosphere by different SLM machines and different powders were studied. Their orientation maps in the build direction are given in **Figure 2. *7***. These maps present identical microstructural characteristics to that shown in **Figure 2. *4***: the microstructure is ferritic. In addition, epitaxial columnar grains are observed along the build direction. These findings are remarkable, because even though these parts were fabricated by different machines and various construction

parameters, or in other words have undergone different thermal histories, they all presented a ferritic microstructure. Solely the grain size and shape changed from one part to another due to different process parameters. However, it must be acknowledged that these results might not represent the general case: other types of microstructures (i.e. martensite with retained austenite) might be obtained in SLM depending on the heating/cooling rates, material composition and atmosphere. However in the three cases investigated here, always the same ferritic microstructure was obtained, which at least suggests a certain generality of the conclusions.

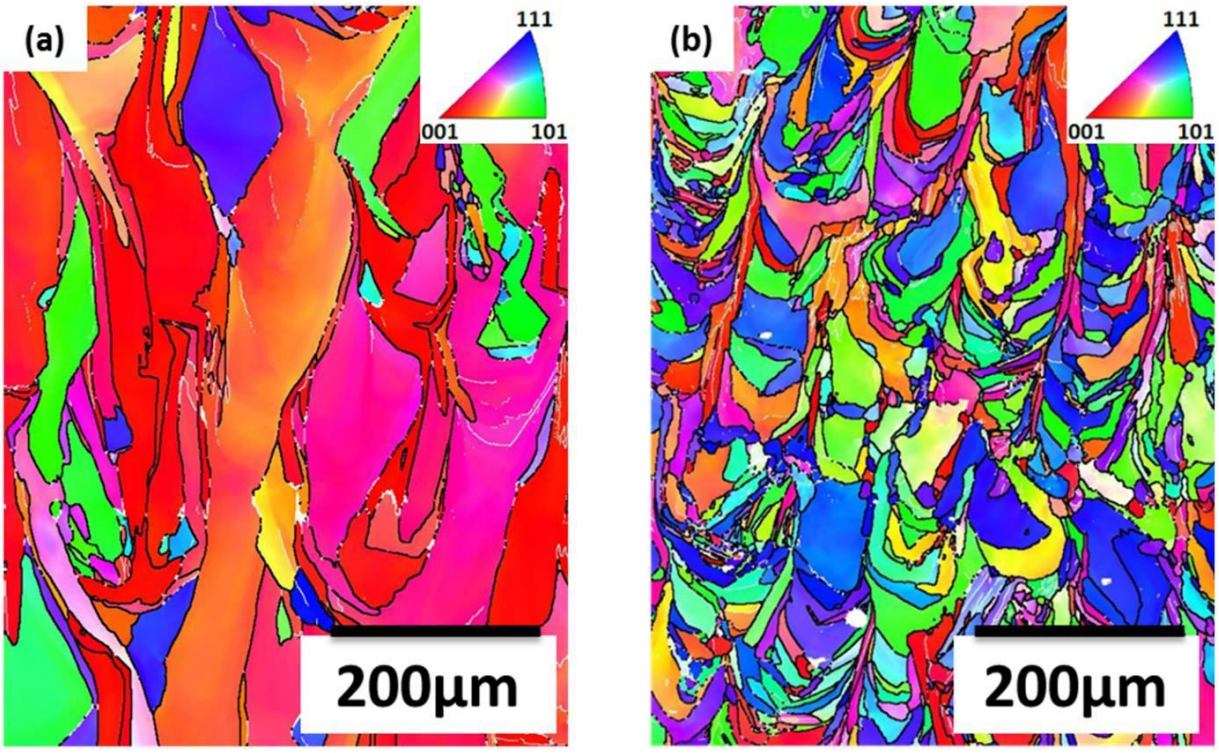

Figure 2. 7: EBSD orientation maps (IPF Z) of as-built 17-4 PH steel in the (Y-Z) plane fabricated by (a) SLM machine 1 and (b) SLM machine 2 showing coarse grains having an epitaxial growth in the build direction. The two machines used here are different from that mainly used in this study.

Figure 2. *8* shows the pole figures corresponding to the (X-Y) plane of as built 17-4 PH steel shown in **Figure 2. *5***. A strong fiber texture is observed with a <100> direction preferentially aligned with the build direction Z. The <100> fiber texture is the common solidification texture for cubic crystals, including FCC and BCC metals. However, steels usually undergo the phase transformation δ(BCC) → γ(FCC) → α or α'(BCC), resulting in a more random texture [36]. Therefore, the strong fiber texture observed in **Figure 2. *8*** contradicts with the occurrence of this transformation sequence. In contrast, it suggests that the microstructure observed is the one obtained directly after solidification, without

any further solid state phase transformation. This confirms the previous analyses that δ(BCC) phase has by-passed the austenite phase during SLM thermal cycles.

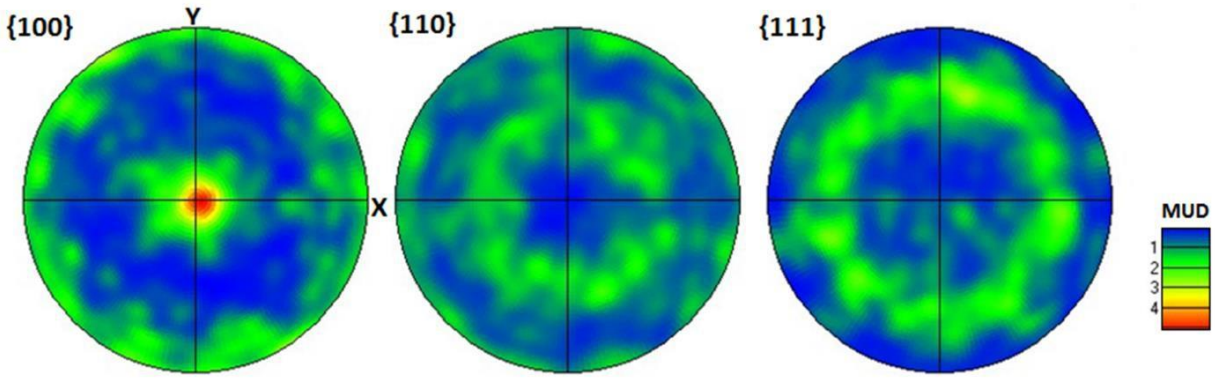

Figure 2. 8: {100}, {110} and {111} pole figures corresponding to the (X-Y) plane of as-built 17-4 PH steel in figure 5 showing a <100> preferred orientation of grains elongated in the build direction.

Element distribution in the as-built 17-4 PH steel was investigated using EDS scans over several regions at high magnification. The colored elemental mapping images of one of these regions are given in **Figure 2. *9***. Under the conditions used for EDS measurements, these maps revealed a homogeneous distribution of elements Fe, Cr, Ni, Nb, Cu and C. No precipitations of carbides or sulfides, usually found in the wrought material, were observable. **Figure 2. *9*** shows no evidence of dendrites, in contrast to some reports [18,19], where EDS measurements showed a dendritic cellular structure having a spacing of some hundreds of nm. It is well known that the solid/liquid interface morphology is mainly dependent on the solidification velocity and the temperature gradient. At very small solidification velocities, a planar interface occurs. As the velocity increases, the morphology changes to globular/cellular dendrites, then to equiaxed dendrites. At even higher growth rates, a planar front will again become stable. This phenomenon, referred to as "absolute stability" and described in details in [37–39], is characterized by diffusionless solidification and solutal trapping, resulting in a microsegregation-free structure. This explains the homogeneous distribution of elements for the as-built materials (***Figure 2. 4.a***,***Figure 2. 7.a and .b***). It should be noted that this non-segregated microstructure can be observed only with a certain combination of process parameters that allows the solidification rates of the melt pool to exceed the critical rate for absolute stability.

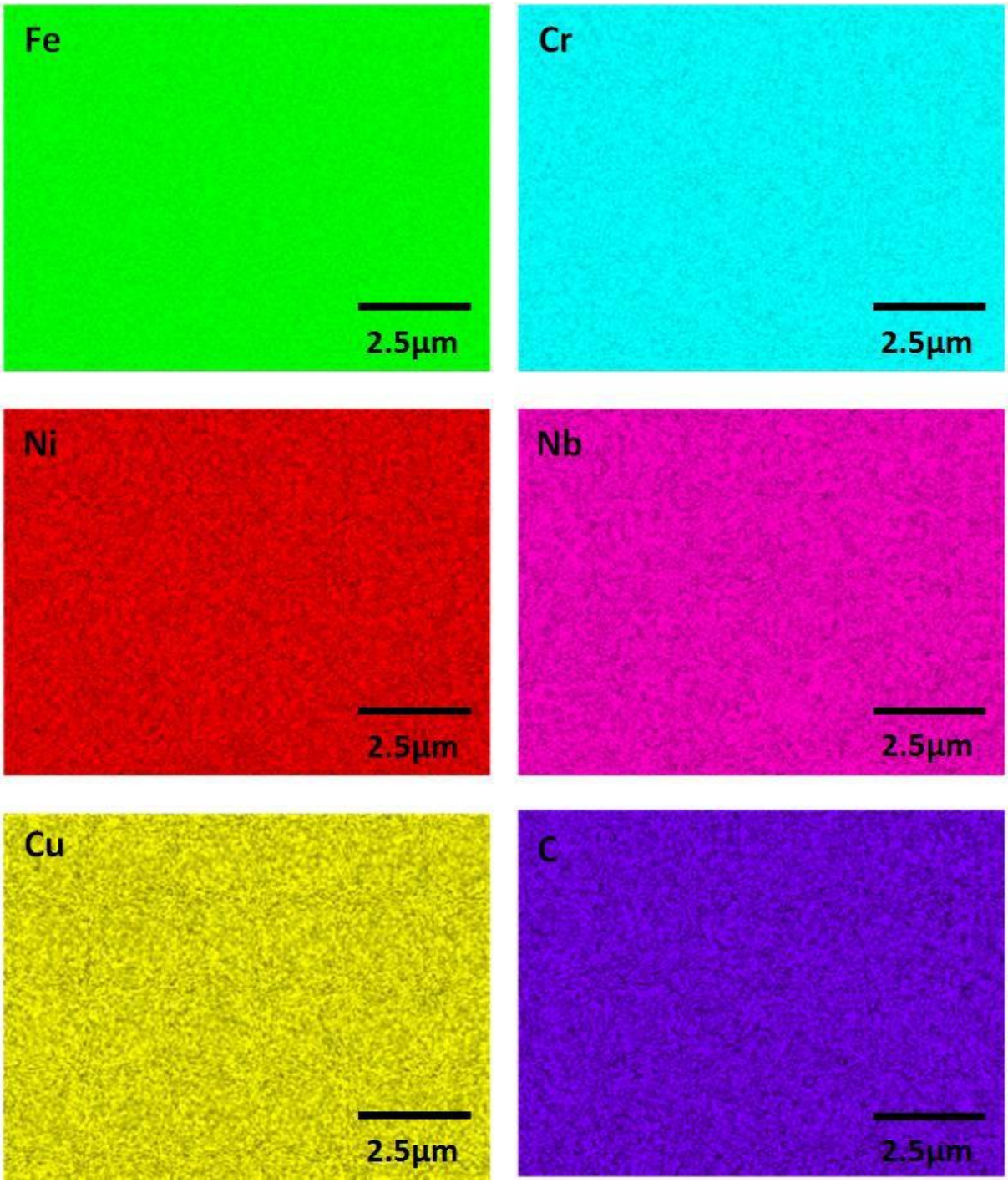

Figure 2. 9: EDS maps of Fe, Cr, Ni, Nb, Cu and C showing a uniform distribution of elements without any segregation.

2.4.4 Microstructure of as-built 17-4 PH after re-austenitization heat treatment

Figure 2. *10* depicts the EBSD orientation map in the (Y-Z) plane of as built material after a re-austenitization treatment at 1050°C i.e. in the fully austenitic domain, followed by a quench. This heat treatment succeeded to recover the martensitic structure by allowing the steel enough time at 1050°C

to be austenitized. The prior austenitic grain boundaries are not clearly detectable, probably because the initial microstructure was made of very coarse grains of ferrite that can modify the austenite nucleation and growth in comparison with an initial martensitic structure. It can also be seen that the grains exhibited a hereditary behavior by partially conserving the previous morphology of elongated grains in the (Y-Z) plane.

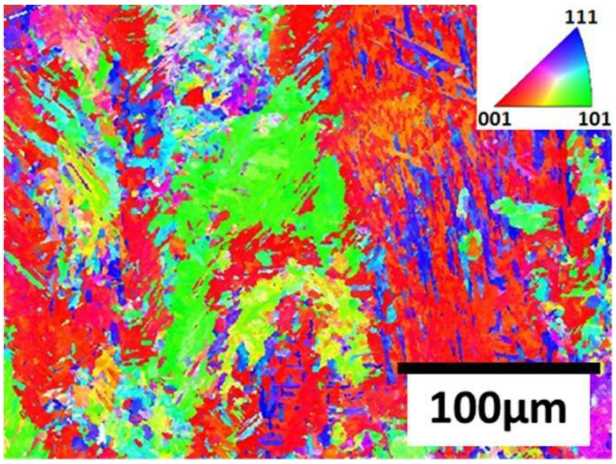

Figure 2. 10: EBSD orientation map (IPF Z) of the (Y-Z) plane after a solution heat treatment at 1050°C and water quench showing a martensitic structure.

2.4.5 Dilatometric measurements

Dilatometry was performed to investigate the austenite to δ ferrite transformation at near melting temperature. The dilation curve showing the longitudinal expansion as a function of temperature is given in **Figure 2. *11***. The wrought material was used for that experiment. During continuous heating, the typical transformation of martensite to austenite takes place above 600°C. Upon further heating, a deviation from linear expansion is detected around 1250°C, characterized by a volume expansion, indicating the beginning of the transformation of austenite to δ ferrite. This expansion related to γ → δ transformation is consistent with the observation conducted on pure iron [40]. As heating progressed, the curve resumed its linear behavior, proving the completion of the transformation γ → δ before reaching metal melting. In the cooling part, a straight line is observed corresponding to the fully formed ferrite shrinkage. Upon further cooling, the onset of the reverse transformation δ → γ occurs, identified by a deviation from this line. The austenite is then fully formed and is stable, or metastable, until ~ 130°C, where it undergoes the usual diffusionless martensitic transformation. This dilatometric measurement is an indication that 17-4 PH stainless steel is fully ferritic at high temperatures (above ~ 1320°C).

Another dilatometric test was carried out on as-built SLM-ed 17-4 PH steel to examine its transformation behavior. The initial state of this material is δ ferrite. **Figure 2.*12*** depicts the curve of dilation as a function of temperature. During heating, δ ferrite transformed normally to austenite. During cooling, the austenite to martensite transformation occurred. The identical behavior of δ ferrite and martensite regarding the phase transformation to austenite is not surprising since both phases have the same BCC structure. This result is consistent with the microstructural observation of as-built 17-4 PH steel after solution heat treatment (**Figure 2.*10***), showing that the martensitic microstructure can be recovered from the ferritic as-built material after heat treatment at 1050°C , followed by quenching.

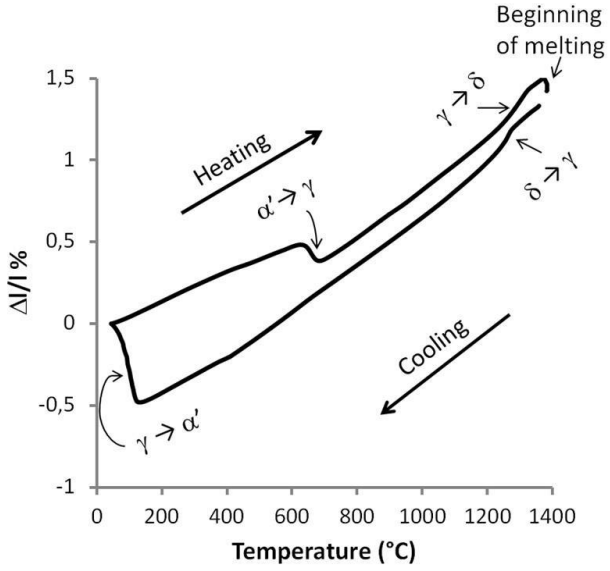

Figure 2. 11: Dilation as a function of temperature for 17-4 PH steel showing the formation of δ ferrite above 1250°C. The material used for this experiment was the conventional 17-4 PH steel.

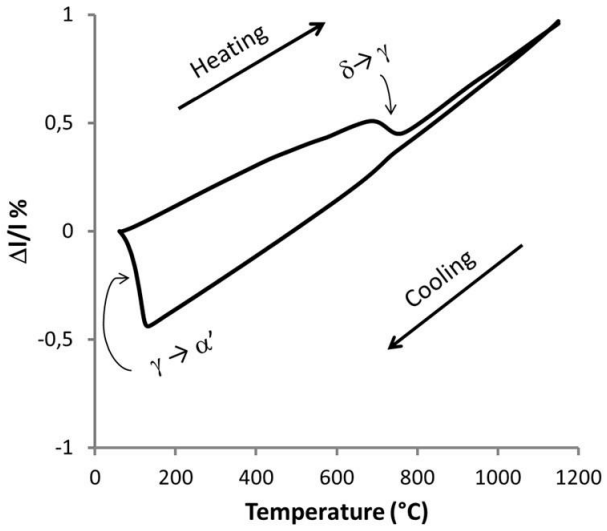

Figure 2. 12: Dilation as a function of temperature for as-built SLM-ed 17-4 PH steel showing a complete austenitization during heating and the martensitic transformation upon cooling. The initial state of the material is δ ferrite.

2.5 Conclusion

In this study, microstructural characterization was conducted on 17-4 PH steel in the as-built state produced by SLM. Several conclusions can be made about the observed microstructure:

1. Due to the high cooling and heating rates reached during SLM (10^5-10^6 K/s), the austenite phase doesn't have enough time to be formed. This means that the 17-4 PH steel, after solidification in δ ferrite, encounters no further metallurgic transformation during its thermal cycles. This results in a stable ferritic microstructure at the end of the SLM process. Complementary measurements of neutron diffraction have demonstrated that 17-4 PH steel is mainly ferritic at melting temperature (see appendix 2).
2. The large thermal gradient existing between the melt pool and the previously solidified layers promoted a highly anisotropic microstructure having coarse grains elongated along the build direction. In addition, these grains are seen to cross several layers suggesting the occurrence of an epitaxial solidification.
3. A strong fiber texture was observed with the <100> crystal orientation aligned preferentially with the build direction. The conservation of this solidification texture contradicts with the possible existence of any phase transformation in the solid state during the process.
4. A diffusionless solidification can be demonstrated from the EDS results that showed a homogeneous distribution of alloying elements inside the grains. Due to the high cooling rates, the

planar solid/liquid interface was stabilized ("absolute stability") resulting in a diffusion free solidification with solute trapping and a segregation-free microstructure.

5. Other specimens of as-built 17-4 PH steel fabricated in different SLM machines were also studied. In each case a fully ferritic microstructure was obtained, which suggests a certain generality of this result. In addition, microstructural characterization was conducted on 17-4 PH gas-atomized powder that showed also a ferritic microstructure. This was attributed to the high cooling rates experienced during atomization (see appendix 3).

2.6 References

[1] N. Guo, M.C. Leu, Additive manufacturing: technology, applications and research needs, Frontiers of Mechanical Engineering. 8 (2013) 215–243. https://doi.org/10.1007/s11465-013-0248-8.

[2] J.-P. Kruth, M.-C. Leu, T. Nakagawa, Progress in additive manufacturing and rapid prototyping, Cirp Annals. 47 (1998) 525–540. https://doi.org/10.1016/S0007-8506(07)63240-5.

[3] L.E. Murr, E. Martinez, K.N. Amato, S.M. Gaytan, J. Hernandez, D.A. Ramirez, P.W. Shindo, F. Medina, R.B. Wicker, Fabrication of Metal and Alloy Components by Additive Manufacturing: Examples of 3D Materials Science, Journal of Materials Research and Technology. 1 (2012) 42–54. https://doi.org/10.1016/S2238-7854(12)70009-1.

[4] M. Rombouts, J.-P. Kruth, L. Froyen, P. Mercelis, Fundamentals of selective laser melting of alloyed steel powders, CIRP Annals-Manufacturing Technology. 55 (2006) 187–192. https://doi.org/10.1016/S0007-8506(07)60395-3.

[5] J.P. Kruth, L. Froyen, J. Van Vaerenbergh, P. Mercelis, M. Rombouts, B. Lauwers, Selective laser melting of iron-based powder, Journal of Materials Processing Technology. 149 (2004) 616–622. https://doi.org/10.1016/j.jmatprotec.2003.11.051.

[6] A.V. Gusarov, I. Yadroitsev, Ph. Bertrand, I. Smurov, Heat transfer modelling and stability analysis of selective laser melting, Applied Surface Science. 254 (2007) 975–979. https://doi.org/10.1016/j.apsusc.2007.08.074.

[7] M. Averyanova, E. Cicala, P. Bertrand, D. Grevey, Experimental design approach to optimize selective laser melting of martensitic 17-4 PH powder: part I-single laser tracks and first layer, Rapid Prototyping Journal. 18 (2012) 28–37. https://doi.org/10.1108/13552541211193476.

[8] T. Niendorf, S. Leuders, A. Riemer, H.A. Richard, T. Tröster, D. Schwarze, Highly Anisotropic Steel Processed by Selective Laser Melting, Metallurgical and Materials Transactions B. 44 (2013) 794–796. https://doi.org/10.1007/s11663-013-9875-z.

[9] S. Dadbakhsh, B. Vrancken, J.-P. Kruth, J. Luyten, J. Van Humbeeck, Texture and anisotropy in selective laser melting of NiTi alloy, Materials Science and Engineering: A. 650 (2016) 225–232. https://doi.org/10.1016/j.msea.2015.10.032.

[10] U.K. Viswanathan, S. Banerjee, R. Krishnan, Effects of aging on the microstructure of 17-4 PH stainless steel, Materials Science and Engineering: A. 104 (1988) 181–189. https://doi.org/10.1016/0025-5416(88)90420-X.

[11] W.D. Yoo, J.H. Lee, K.T. Youn, Y.M. Rhyim, Study on the Microstructure and Mechanical Properties of 17-4 PH Stainless Steel Depending on Heat Treatment and Aging Time, Solid State Phenomena. 118 (2006) 15–20. https://doi.org/10.4028/www.scientific.net/SSP.118.15.

[12] C.N. Hsiao, C.S. Chiou, J.R. Yang, Aging reactions in a 17-4 PH stainless steel, Materials Chemistry and Physics. 74 (2002) 134–142. https://doi.org/10.1016/S0254-0584(01)00460-6.

[13] Z. Hu, H. Zhu, H. Zhang, X. Zeng, Experimental investigation on selective laser melting of 17-4PH stainless steel, Optics & Laser Technology. 87 (2017) 17–25. https://doi.org/10.1016/j.optlastec.2016.07.012.
[14] A. Yadollahi, N. Shamsaei, S.M. Thompson, A. Elwany, L. Bian, Effects of building orientation and heat treatment on fatigue behavior of selective laser melted 17-4 PH stainless steel, International Journal of Fatigue. 94 (2017) 218–235. https://doi.org/10.1016/j.ijfatigue.2016.03.014.
[15] A. Yadollahi, N. Shamsaei, S.M. Thompson, A. Elwany, L. Bian, Mechanical and microstructural properties of selective laser melted 17-4 PH stainless steel, in: ASME 2015 International Mechanical Engineering Congress and Exposition, American Society of Mechanical Engineers, 2015: p. V02AT02A014–V02AT02A014. http://proceedings.asmedigitalcollection.asme.org/proceeding.aspx?articleid=2500381 (accessed October 27, 2016).
[16] L.E. Murr, E. Martinez, J. Hernandez, S. Collins, K.N. Amato, S.M. Gaytan, P.W. Shindo, On the characterization of stainless steel 316L parts produced by selective laser melting, Journal of Materials Research and Technology. 1 (2012) 167–177. https://doi.org/10.1016/S2238-7854(12)70029-7.
[17] T. LeBrun, T. Nakamoto, K. Horikawa, H. Kobayashi, Effect of retained austenite on subsequent thermal processing and resultant mechanical properties of selective laser melted 17–4 PH stainless steel, Materials & Design. 81 (2015) 44–53. https://doi.org/10.1016/j.matdes.2015.05.026.
[18] H.K. Rafi, D. Pal, N. Patil, T.L. Starr, B.E. Stucker, Microstructure and Mechanical Behavior of 17-4 Precipitation Hardenable Steel Processed by Selective Laser Melting, Journal of Materials Engineering and Performance. 23 (2014) 4421–4428. https://doi.org/10.1007/s11665-014-1226-y.
[19] S. Cheruvathur, E.A. Lass, C.E. Campbell, Additive Manufacturing of 17-4 PH Stainless Steel: Post-processing Heat Treatment to Achieve Uniform Reproducible Microstructure, JOM. 68 (2016) 930–942. https://doi.org/10.1007/s11837-015-1754-4.
[20] P. Lacombe, B. Baroux, G. Béranger, in: Les aciers inoxydables, Ed. de physique, Les Ulis, 1991: p. 496.
[21] F. Hengsbach, P. Koppa, K. Duschik, M.J. Holzweissig, M. Burns, J. Nellesen, W. Tillmann, T. Tröster, K.-P. Hoyer, M. Schaper, Duplex stainless steel fabricated by selective laser melting - Microstructural and mechanical properties, Materials & Design. 133 (2017) 136–142. https://doi.org/10.1016/j.matdes.2017.07.046.
[22] K. Saeidi, L. Kevetkova, F. Lofaj, Z. Shen, Novel ferritic stainless steel formed by laser melting from duplex stainless steel powder with advanced mechanical properties and high ductility, Materials Science and Engineering: A. 665 (2016) 59–65. https://doi.org/10.1016/j.msea.2016.04.027.
[23] D. Peckner, I.M. Bernstein, eds., in: Handbook of Stainless Steels, McGraw-Hill, New York, 1977: p. 4.11.
[24] J.C. Lippold, D.J. Kotecki, in: Welding Metallurgy and Weldability of Stainless Steels, John Wiley, Hoboken, NJ, 2005: pp. 264–286.
[25] S. Fukumoto, W. Kurz, Solidification phase and Microstructure Selection Maps for Fe-Cr-Ni alloys, (1999). https://doi.org/10.2355/isijinternational.39.1270.
[26] E. Johnson, L. Grabak, A. Johansen, L.S. Kristensen, J.V. Wood, Microstructure of rapidly solidified stainless steel, Materials Science and Engineering. 98 (1988) 301–303. https://doi.org/10.1016/0025-5416(88)90174-7.
[27] C.R. Das, H.C. Dey, G. Srinivasan, S.K. Albert, A.K. Bhaduri, A. Dasgupta, Weldability of 17-4PH stainless steel in overaged heat treated condition, Science and Technology of Welding and Joining. 11 (2006) 502–508. https://doi.org/10.1179/174329306X148147.

[28] W. Liu, J. Ma, M.M. Atabaki, R. Pillai, B. Kumar, U. Vasudevan, H. Sreshta, R. Kovacevic, Hybrid Laser-arc Welding of 17-4 PH Martensitic Stainless Steel, Lasers in Manufacturing and Materials Processing. 2 (2015) 74–90. https://doi.org/10.1007/s40516-015-0007-2.
[29] A. Ziewiec, A. ZieliŃska-Lipiec, E. Tasak, Microstructure of Welded Joints of X5CrNiCuNb16-4 (17-4 PH) Martensitic Stainlees Steel After Heat Treatment, Archives of Metallurgy and Materials. 59 (2014). https://doi.org/10.2478/amm-2014-0162.
[30] J.W. Elmer, The influence of cooling rate on the microstructure of stainless steel alloys, 1988. https://doi.org/10.2172/5678406.
[31] G. Turichin, M. Kuznetsov, M. Sokolov, A. Salminen, Hybrid Laser Arc Welding of X80 Steel: Influence of Welding Speed and Preheating on the Microstructure and Mechanical Properties, Physics Procedia. 78 (2015) 35–44. https://doi.org/10.1016/j.phpro.2015.11.015.
[32] K. Poorhaydari, B.M. Patchett, D.G. Ivey, Estimation of Cooling Rate in the Welding of Plates with Intermediate Thickness, Welding Journal. 84 (2005) 149s–155s.
[33] R. Kapoor, I.S. Batra, On the α' to γ transformation in maraging (grade 350), PH 13-8 Mo and 17-4 PH steels, Materials Science and Engineering: A. 371 (2004) 324–334. https://doi.org/10.1016/j.msea.2003.12.023.
[34] A. Mondelin, Modélisation de l'intégrité des surfaces usinées: Application au cas du tournage finition de l'acier inoxydable 15-5PH, Ecole Centrale de Lyon, 2012. https://tel.archives-ouvertes.fr/tel-00838512/ (accessed August 30, 2017).
[35] F. Christien, M.T.F. Telling, K.S. Knight, A comparison of dilatometry and in-situ neutron diffraction in tracking bulk phase transformations in a martensitic stainless steel, Materials Characterization. 82 (2013) 50–57. https://doi.org/10.1016/j.matchar.2013.05.002.
[36] S. Suwas, R.K. Ray, in: Crystallographic Texture of Materials, Springer London, London, 2014: pp. 73–88. https://doi.org/10.1007/978-1-4471-6314-5.
[37] Doru M. Stefanescu, Roxana Ruxanda, Fundamentals of Solidification, ASM International. 9 (2004) 71–92.
[38] W. Kurz, D.J. Fisher, in: Fundamentals of Solidification, 3rd ed., Trans Tech Publications, 1992: pp. 133–161.
[39] M.E. Glicksman, in: Principles of Solidification, Springer New York, New York, NY, 2011: pp. 427–446. https://doi.org/10.1007/978-1-4419-7344-3.
[40] Z.S. Basinski, W. Hume-Rothery, A.L. Sutton, The Lattice Expansion of Iron, Proceedings of the Royal Society A: Mathematical, Physical and Engineering Sciences. 229 (1955) 459–467. https://doi.org/10.1098/rspa.1955.0102.

Chapter 3Influence of microstructure and manganese sulfides on corrosion resistance of selective laser melted 17-4 PH stainless steel in acidic chloride medium.

Table of contents

(The work presented in this chapter was submitted to Corrosion Science)

3.1 Abstract

Selective laser melting (SLM) is a technique of additive manufacturing based on powder bed fusion that allows 3D objects to be fabricated by adding material layer by layer. Because of the high cooling and heating rates experienced during fabrication the obtained materials present different microstructures from their wrought counterparts. Consequently, their corrosion behaviors will be different. In this work, the corrosion resistance of 17-4 PH stainless steel obtained by SLM was investigated in acidic chloride aqueous solutions. First, a microstructural characterization was done on the as-built and re-austenitized SLM-ed steels. It was found that, unlike the wrought material, the as-built steel didn't have a martensitic microstructure but instead was entirely ferritic; more specifically delta ferrite. This was due to the high cooling and heating rates that suppressed the austenite formation and retained the delta ferrite. After re-austenization heat treatment and quenching, the SLM-ed was fully transformed to martensite. The corrosion behavior was evaluated by open circuit potential measurements and potentiodynamic polarization scans. The SLM-ed steels in both conditions (as-built and re-austenitized) had the same general corrosion resistance which was correlated with their similar chemical composition. However, pitting resistance was lower in the re-austenitized SLM-ed steel due to its higher defect density (grain boundaries and dislocations). In addition, the re-austenitized martensitic SLM-ed steel had superior general corrosion behavior than the wrought martensitic steel. This was due to the nearly absence of MnS inclusions in the re-austenitized steel, while their presence in the wrought steel induced a destabilization of the passive film.

3.2 Introduction

Stainless steels are widely used in a variety of applications such as food processing, petrochemical plants and transportation industries, due to their high strength and good corrosion resistance. Their favorable corrosion properties are due to the presence of more than 11% chromium content by mass which allows for an adherent protective chromium oxide surface film to be formed [1]. 17-4 PH is a precipitation hardenable stainless steel that contains 15-17.5 wt.% of Cr and 3-5 wt.% of Ni. It usually has a martensitic microstructure and can be hardened by copper precipitates through aging treatments [2–4]. The corrosion resistance of this steel has been a subject of several studies that dealt with general corrosion, pitting, hydrogen embrittlement, and stress corrosion cracking. It was found that 17-4 PH steel was susceptible to both general and pitting corrosion in aqueous environment [5–7]. Pitting corrosion induced by a sulfuric and chloride acidic medium initiated at the MnS inclusions [6,7].

MnS inclusions have been known to be preferential sites for pit initiation in stainless steels in chloride containing solutions. They form weak points at the surface of a stainless steel because they are not protected by a passive oxide film [8]. Thus, chloride ions are adsorbed onto the sulfide inclusions, leading to the dissolution of the sulfide ions. The dissolution occurs according to the following reactions [9,10]:

$MnS + 3H_2O \rightarrow Mn^{2+} + HSO_3^- + 5H^+ + 6e^-$

$HSO_3^- + 5H^+ + 4e^- \rightarrow S + 3H_2O$

The resulting sulfur species released from the reaction are deposited in the vicinity of the inclusion. The dissolution of the MnS inclusion is accompanied by a decrease in pH, formation of a salt film and deposition of a sulfur layer. As a result, re-passivation will be impeded and acceleration of pit propagation will take place [8,10–15]. It has been reported that the stability of the pit is mainly related to the size, shape and orientation of the sulfide inclusions [14–16]. Furthermore, E. William *et al.* [17] demonstrated that a chromium depleted zone developed in the region adjacent to the MnS inclusion. In his analysis, this zone contributed to the increase of the dissolution rate. However, this Cr-depleted zone was not observed by other authors [18,19] and leaves the question of its presence ambiguous. On these bases, MnS inclusions must be controlled in stainless steels in order to minimize the pitting attacks. Indeed, an enhancement of pitting resistance after a laser surface melting treatment has been reported. This was attributed to the redistribution, or elimination, of MnS inclusions caused by the surface treatment [15,20,21]. It is important to note that the majority of these studies focused on the effect of MnS inclusions on the corrosion resistance in austenitic stainless steel. Little attention was paid to their effect in ferritic and martensitic stainless steels.

Recently, stainless steels have been produced by additive manufacturing (AM) techniques, in particular the selective laser melting (SLM) process. AM consists of adding material layer by layer according to a computer-aided design (CAD) in order to create a three-dimensional object [22–24]. The microstructures of stainless steels obtained from AM have been the subject of much research [25–29]. It has been shown that their microstructures can be very different from their wrought counterparts which present an anisotropic structure exhibiting dissimilar phase compositions. Such discrepancy was correlated to the high cooling rates that can be achieved during fabrication (10^5-10^6 K/s). Since the properties of the passive film vary with both composition and microstructure, the material is expected to have different corrosion behavior. In addition, AM stainless steels were free from MnS inclusions due to insufficient time for nucleation [30]. The absence of inclusions has been proven to be beneficial for the corrosion resistance of stainless steels. This was confirmed by authors who studied the

corrosion behavior of austenitic stainless steel fabricated by AM. The AM material exhibited better electrochemical properties than the wrought steel [30–32]. In addition, M. R. Stoudt *et al.* reported an improved pitting corrosion of the AM 17-4 PH steel after a solution heat treatment. This improvement was associated with finer martensite lath, redistributed NbC precipitates and a more stable passive film [33]. However, it has also been reported that the enhanced corrosion of the AM 17-4 PH steel is due to the presence of porosity [34].

There have been limited number of studies concerning the corrosion behavior of AM 17-4 PH steel. As a result, and to further current understanding, this study focuses on the electrochemical characteristics of 17-4 PH steel fabricated by SLM in chloride containing acidic medium. A correlation between the corrosion behavior and the microstructure was made. Moreover, a comparison was also made with respect to the wrought material.

3.3 Experimental procedure

3.3.1 Materials

The materials used in this study were wrought and SLM-ed 17-4 PH stainless steels. The wrought material was a commercial bar from UGINE (cast # 818025). It was studied after a solution heat treatment at 1050°C for 1 hour followed by a water quench. Concerning the SLM-ed 17-4 PH steel, parts were cut from cylinders having 16 mm diameter and 105 mm length. They were fabricated in an SLM machine of type EOS M270. The fabrication was done in an argon purging environment. The longitudinal axis of the cylinder was horizontal perpendicular to the building direction Z. The SLM-ed material was studied both in the as-built condition and after a re-austenitization heat treatment at 1050°C for 1 hour and a water quench. The plane used in the corrosion experiments was the (Y-Z) plane which is parallel to the build direction, Z. The chemical composition of both materials is given in **Table 3. *1***. The full composition of the wrought material is indicated (data from the steel provider) in the first line of table 1. Additional measurements were conducted on both wrought and SLM-ed materials (lines 2 and 3 of **Table 3. *1***). These measurements were carried out using X-ray fluorescence (XRF) (FISCHERSCOPE X-Ray XAN-FD) for elements Ni, Cr and Cu, and using combustion elemental analysis (CEA) for C, S (LECO CS 444/LS), N and O (LECO TC-436).

Table 3. 1: Chemical composition (wt. %) of wrought and SLM-ed 17-4 PH stainless steels.

17-4 PH		C	Ni	Si	P	Mn	Cr	Cu	S	N	O	Nb	e
												F	
Wrought	Provider Data sheet	0.031	4.82	0.31	0.016	0.81	15.61	3.12	0.02	-	-	0.21	Bal.
	XRF/CEA	0.026	4.95	-	-	-	16.18	3.09	0.021	0.033	0.007	-	Bal.
SLM-ed	XRF/CEA	0.03	4.16	-	0.008	-	16.11	3.73	0.003	0.033	0.046	0.3	Bal.

3.3.2 Microstructural characterization

For microstructural characterization, scanning electron microscopy (SEM Zeiss SUPRA55VP) was used for both electron backscatter diffraction (EBSD) and energy dispersive spectroscopy (EDS). For both modes, the SEM was operating at 20 kV. For the EBSD preparation, samples were polished down to 1200 grit, followed by electropolishing using 94% ethanol + 6% perchloric acid as electrolyte at 25 V for 60 s. For the EDS preparation, samples were only polished up to a 0.25 µm diamond finish.

The size, density and volume fraction of MnS inclusions and porosities were estimated from the EDS maps and the optical micrographs respectively, by using the image processing program ImageJ.

Neutron diffraction was performed using the high-resolution powder diffractometer, HRPD, at the ISIS neutron and muon spallation facility, Rutherford Appleton Laboratory (RAL), UK [35]. Using the instrument's standard 30-130 ms time-of-flight measurement window, the range of interplanar distances, or d-spacings, examined with highest-resolution backscattering detectors was between 0.65 and 2.65 Å. Data were normalized to the incident spectrum and corrected for instrumental efficiency using V:Nb null-scattering standard. Patterns were acquired at room temperature for the three studied materials. The dislocation density ρ can be correlated to the average peak broadening Δ /$\square$(where d is the interplanar spacing) using the following Stibitz equation (eq.1) [36,37]:

$$\rho = \frac{\square\square}{\mu\square\square(\square+} (\Delta\ /\square^{\square} \qquad \text{(eq.1)}$$

$\square\upsilon^{\square})$

here E is the Young's modulus, μ is the shear modulus with $\mu \approx 2.5$ for the materials studied here. The burger vector b is approximately equal to 2.49 Å and the Poisson's coefficient υ is equal to 0.25.

The peak broadening Δ was determined using a deconvolution method. The determination of Δ / θ was done on four peaks corresponding to the crystallographic planes (220), (211), (200) and (110) and then their average was computed. This is the same methodology that was already used on 17-4 PH steel in a previous study by Christien *et al* [38]. Furthermore, the mass fraction of the austenite present in the three studied materials was determined by the Rietveld structure refinement method applied to the neutron powder diffraction data using GSAS/Expgui [39,40].

Surface analyses were performed using X-Ray Photoelectron Spectroscopy (XPS) with a Thermo VG Thetaprobe spectrometer instrument. Analyses were carried out with a focused monochromatic AlKα source (hν = 1486.68 eV, 400 µm spot size) and a concentric hemispherical analyzer operating in constant ΔE mode. The energy scale was calibrated with sputter-cleaned pure reference samples of Au, Ag and Cu with Au4f7/2, Ag3d5/2 and Cu3p3/2 positioned at binding energies of 83.98, 386.26 and 932.67 eV respectively. In order to detect the presence of chemical species containing sulfur at the surface of samples, narrow scans were recorded for S2p peak with a step size of 0.1 eV and a pass energy of 50 eV. This pass energy gives a width of the Ag3d5/2 peak measured on a sputter cleaned pure Ag sample of 0.55 eV. These scans were performed with the analyzer operating in standard mode but also in angle resolved mode using the ability of the spectrometer to collect simultaneously several photo-electron emission angles over a 60° range without tilting the sample. The S2p experimental curves were adjusted with components using lineshapes consisting of a convolution product of a Gaussian function (75%) and Lorentzian function (25%) for components associated with the sulfate and sulfite species and asymmetric lineshapes for components associated with sulfide species.

3.3.3 Electrochemical measurements

Electrochemical measurements were performed on the three materials using a VoltaLab PST 006 potentiostat. They were carried out using a typical three-electrode cell. The working electrodes were wrought and SLM-ed ((Y-Z) plane in the as-built and re-austenitized condition) materials. The counter electrode used to provide the applied current is made of platinum. Potentials were measured with reference to the saturated calomel reference electrode (SCE). Specimens were polished with a 0.25 µm diamond paste to produce a mirror like surface finish. They were rinsed and cleaned with water and ethanol. In order to have the same surface condition at the beginning of each test, the specimens were left after polishing for one day in air to form a similar passive film. The surface exposed to the solution had an area of 0.5 - 0.8 cm^2. The test solution was deionized water with 30g/l NaCl. It was deaerated using a continuous flux of N_2 gas 24 hours before introducing the specimen and throughout the experiment. The studied pH were varied between 1.5, 2.5 and 3.5 with an error of ± 0.05. They were adjusted by adding some droplets of hydrochloric acid and sodium hydroxide in the solution. The

temperature was maintained at room temperature (20°C ± 2°C). The open circuit potential was measured for an immersion time of 5 hours. The anodic scans were repeated 3 times on each specimen, and at each condition, to ensure the good reproducibility of the experiments. The polarization curves shown in this paper are the mean of the three curves measured (the raw data of each curve are provided as supplementary material). The scans started from -600 mV vs. SCE, slightly in the cathodic region, and continued until an anodic current of 1 mA was reached. The scan rate applied during testing was 0.1 mV/min.

3.4 Results and discussion

3.4.1 Microstructure

The wrought 17-4 PH steel was studied after a solution heat treatment at 1050°C for 1 hour followed by a water quench. The microstructure obtained was a fully martensitic structure, as shown by the EBSD map in ***Figure 3. 1.a***. The laths of martensite are gathered into different packets inside the same prior austenitic grain. The average martensitic grain size was measured using the intercept method and is given in **Table 3. *2***. In addition, a reconstruction of the former austenitic grains was applied to the EBSD map using an automatic iterative method based on the austenite/martensite orientation relationships developed by T. Nyyssönen [41]. ***Figure 3. 1.d*** reveals the map of the reconstructed former austenite grains. Their average size was measured using the same intercept method and was found to be approximately 19.8 µm. The EDS measurements in **Figure 3. 2*.a*** reveal a homogeneous distribution of elements and the presence of circular MnS inclusions of approximately 1 µm in diameter, as well as some oxides. **Table 3. *2*** indicates the inclusions density, size and volume fraction estimated from the EDS maps. In addition, NbC precipitates are also present in this material. These observations are typically found in the wrought 17-4 PH steel after this heat treatment.

The as-built 17-4 PH steel microstructure is given in ***Figure 3. 1.b*** In contrast to the wrought steel, it consists of coarse grains having an average grain size of 9.2 µm. No martensite laths can be observed. Since the majority phase has a BCC structure, it is deduced that the as-built SLM-ed 17-4 PH steel has a ferritic microstructure, more specifically δ ferrite. This is due to the high cooling and heating rates experienced during SLM which do not allow the austenite phase time to be formed. Thus, the δ ferrite formed during solidification doesn't undergo any further metallurgical transformation. This can be described as if delta ferrite has by-passed the austenite phase. In addition, during SLM construction the steel will exhibit multiple thermal cycles and the temperatures can reach the austenite phase stability range. Thus, there might be a possibility for the austenite to form. However, due to the extremely high thermal rates the austenite formation will also be suppressed and the same by-passing

phenomenon will occur. Thus, the delta ferrite will be maintained during the SLM process until the building of the part is completed. More details on this by-passing phenomenon are given in a previous paper [29]. **Figure 3. 2.*b*** depicts the EDS measurements of the as-built material. It reveals a homogeneous distribution of elements. This homogeneity of elements is correlated to a planar solidification front characteristic of very high cooling rates, as is the case with SLM fabrication. The planar interface between solid and liquid state is an indication of a diffusionless solidification. Unlike the wrought material, no MnS inclusions or NbC precipitates were visible. This can be due to the high cooling and heating kinetics that suppressed their nucleation and growth. Only widely-spaced oxides can be observed.

After re-austenization (at 1050°C for 1 hour followed by a water quench), the SLM-ed material presents a martensitic microstructure, as shown in the EBSD map in ***Figure 3. 1.c***. This implies that the delta ferrite-to-austenite transformation took place during heating and subsequent holding for 1 hour at 1050°C, and that the austenite-to-martensite transformation occurred during cooling, resulting in the observed microstructure. From the EBSD map, it can be seen that the laths of martensite are gathered into packets inside prior austenitic grains. The martensitic grain size was measured using the intercept method and is given in **Table 3. *2***. ***Figure 3. 1.e*** shows the map of the reconstructed former austenitic grains. The reconstruction was applied to the EBSD map by using the same automatic iterative method that was applied to the EBSD map of the wrought steel. The average former austenitic grain size was approximated to be 12.5 µm by using the intercept method. From **Table 3. *2***, it can be seen that the martensitic re-austenitized SLM-ed steel has the smallest grain size. **Figure 3. 2.*c*** shows a homogeneous distribution of elements. In addition to rare oxides particles found initially in this steel, MnS and NbS inclusions, as well as NbC precipitates, are formed during this treatment. Since these inclusions and precipitates were able to form during re-austenization, this confirms that the high cooling and heating rates have indeed inhibited their formation during the SLM process. **Table 3. *2*** shows the MnS inclusions density, size and volume fraction. It can be seen that their density and size are less in the re-austenitized SLM-ed steel when compared to the wrought steel.

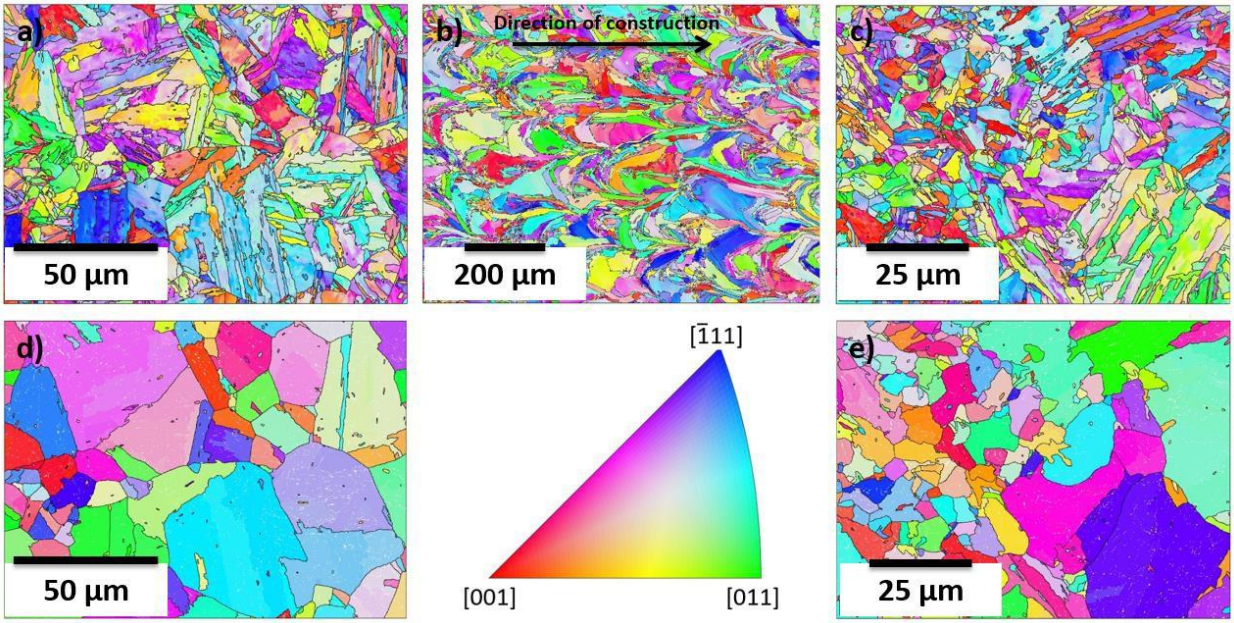

Figure 3. 1: EBSD orientation map of (a) wrought 17-4 PH steel showing a typical martensitic microstructure, (b) as-built 17-4 PH SLM-ed steel in the (Y-Z) plane showing coarse grain ferritic microstructure and (c) re-austenitized 17-4 PH SLM-ed steel showing martensitic microstructure. Prior austenitic grains reconstruction using the EBSD maps is presented in (d) for the wrought steel and in (e) for the re-austenitized SLM-ed steel (IPF coloring).

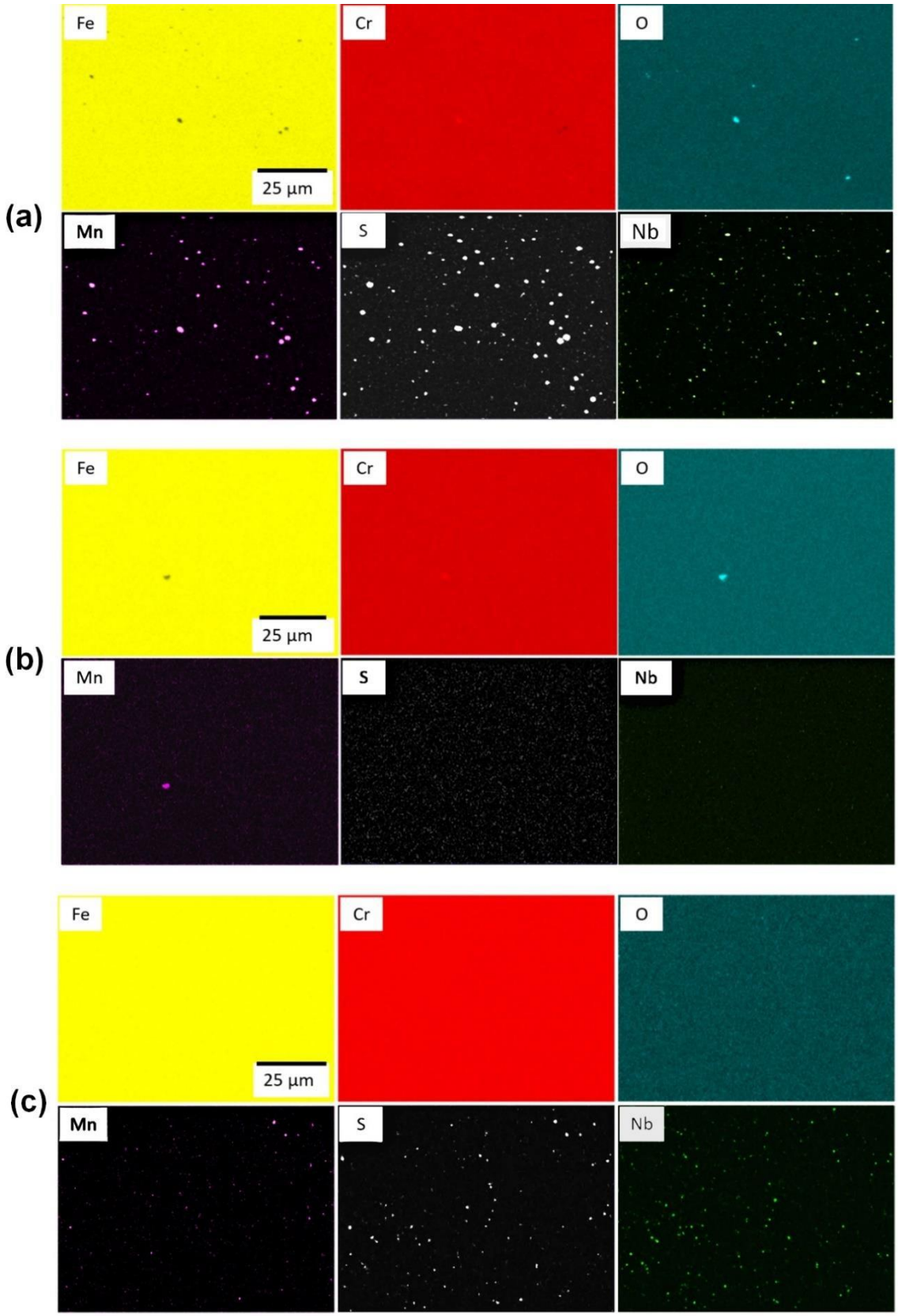

Figure 3. 2: **EDS maps of Fe, Cr, Mn, S, O and Nb showing (a) homogeneous distribution with MnS inclusions, oxides and NbC precipitates for wrought 17-4 PH steel, (b) homogeneous distribution with oxides for as-built 17-4 PH SLM-ed steel and (c) homogeneous distribution with MnS and NbS inclusions, oxides and NbC precipitates for re-austenitized 17-4 PH SLM-ed steel.**

Figure 3. 3 depicts the neutron diffraction pattern of the BCC plane (110) peak (ferrite and martensite) at room temperature for the three steels. It is seen that the BCC peak is larger in area for both martensitic steels (wrought and re-austenitized SLM-ed steels) in comparison with the ferritic as-built SLM-ed steel. From (eq.1), the dislocation density was approximated and is given in **Table 3. *2***. The dislocation density is almost the same for the martensitic steels (wrought and re-austenitized SLM-ed steels). These martensitic steels have higher dislocation density than the as-built SLM-ed steel. This observation is in agreement with several studies showing that the martensitic transformation results in a high dislocation density in the quenched state [42–44]. Furthermore, the austenite mass fraction of the three studied materials was approximated by applying Rietveld refinement method on the neutron diffraction data (**Table 3. *2***). The as-built SLM-ed steel had the highest austenite content. While the wrought and re-asustenized steels had less than a 1% austenite mass fraction. The porosity in the materials was also measured and is given in **Table 3. *2***. The wrought steel was free of porosity while both SLM-ed steels had a similar porosity characteristics.

Table 3. 2: Microstructural features (grain size, MnS inclusions, dislocation density, porosity, austenite) of the three studied steels.

		Wrought	**SLM as-built**	**SLM re-austenitized**
Grain size (µm)		Martensitic: 3.3 Former austenitic: 19.8	Ferritic: 9.2	Martensitic: 2 Former austenitic: 12.5
MnS inclusions	Density: number/area (m^{-2})	$7.6\ 10^{9}$	0	$3.7\ 10^{9}$
	Size (µm)	1.0	0	0.5
	Volume fraction (%)	0.7	0	0.1
Dislocation density (m^{-2})		$\sim 6.0\ 10^{15}$	$\sim 1.0\ 10^{15}$	$\sim 7.0\ 10^{15}$
Porosity	Density: number/area (m^{-2})	0	$1.1\ 10^{8}$	$1.1\ 10^{8}$
	Size (µm)	0	4.4	4.4
	Volume fraction (%)	0	0.1	0.1
Austenite (%)		<1.0	9.2	<1.0

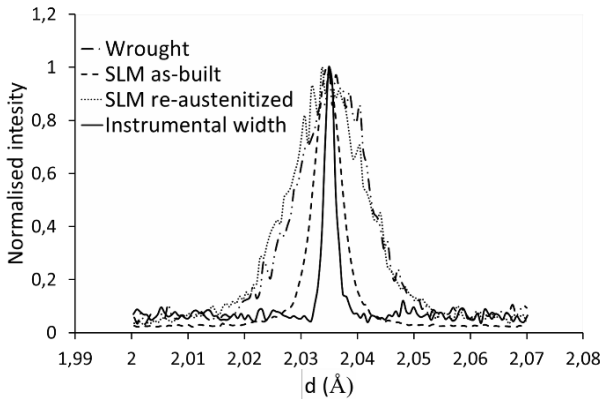

Figure 3. 3: Neutron diffraction pattern of the three studied materials showing a larger BCC (110) peak for both martensitic wrought steel and re-austenitized SLM-ed steels in comparison with the ferritic as-built steel. (d is the interplanar spacing).

3.4.2 Potentiodynamic measurements

Figure 3. 4 depicts the potentiodynamic plots of the SLM-ed steels in the as-built and re-austenitized conditions for different pH in deaerated 30 g/l NaCl solution. The polarization scan starts immediately at the immersion of the working electrode from -600 mV/ SCE (slightly cathodic potential) at 0.1 mV/min scan rate. For each pH, the corrosion potential for both SLM-ed steels is similar and varies between -405 and -455 mV/SCE. At this potential, the anodic dissolution and the cathodic reduction rates at the surface of the electrode are balanced and the sum of their respective density current is equal to zero. As the potential increases, the dissolution of the metal takes place characterized by an increase in current. This region is called the active region. For pH higher than 2.5, the anodic peak current density for both SLM-ed steels is smaller than 10 µA/cm^2 and the metal is considered passivated. The value of 10 µA/cm^2 is the critical active peak value above which the metal is considered as no longer passivated. This arbitrary value corresponds to a corrosion rate of 0.1 mm/year and is taken as the onset of a significant corrosion rate [45,46]. For pH equal to 1.5, the active peaks for the SLM-ed in the as-built and re-austenitized conditions were 45 µA/cm^2 and 60 µA/cm^2 respectively. These peaks are higher than 10 µA/cm^2 and the materials are no longer considered passivated in this potential range.

It can be concluded that the general corrosion behavior of the two steels is very similar (same corrosion potential and same pH of passivation). It should be noted that the two steels have different microstructures: the as built SLM-ed steel is ferritic, while the re-austenitized SLM-ed steel is martensitic. This leads to the conclusion that the microstructure didn't have any effect on the general corrosion behavior. This similar corrosion behavior can be correlated to the identical chemical composition of the two steels that controlled the composition of the passive film and consequently its stability in the acidic chloride medium.

Concerning the pitting corrosion behavior at higher potential, the two steels had different pitting potentials. For all the pH, the pitting potential was higher for the as built SLM-ed steel than the re-austenitized one. Thus, the as built SLM-ed steel is more resistant to the pitting corrosion. The pitting corrosion normally initiates at some microstructural defects or discontinuities in the passive film caused by inclusions, grain boundaries and dislocations [47,48]. Since the re-austenitized SLM-ed steel has a martensitic structure, it has higher dislocation and grain boundary densities than the as-built SLM-ed steel (shown in **Table 3. *2***) which will increase the probability of pit initiation. It is worth mentioning that there have been many studies concerning the effect of grain size on corrosion resistance. However, their results are not conclusive. For ferrous alloys, in some cases, the refinement of grains was considered beneficial for pitting corrosion [49,50]. In other cases, it was detrimental [51–53]. Furthermore, to the author's knowledge, no work has been done concerning the effect of grain size on pitting corrosion in a martensitic stainless steel. In addition, the MnS inclusions present in the re-austenitized SLM-ed steel, which have been proven to be preferential sites for pitting, could be also the cause of the lower pitting potential. However, this assumption is questionable because, as it will be shown later, the MnS inclusions didn't have any effect on the pitting potential of the wrought steel. On the other hand, since the porosity content is the same for both steels, it cannot account for the difference in pitting potential. As shown in **Table 3. *2***, the austenite content was higher in the as-built SLM-ed steel. Thus, it seems that the austenite didn't have any detrimental effect on the observed pitting potential.

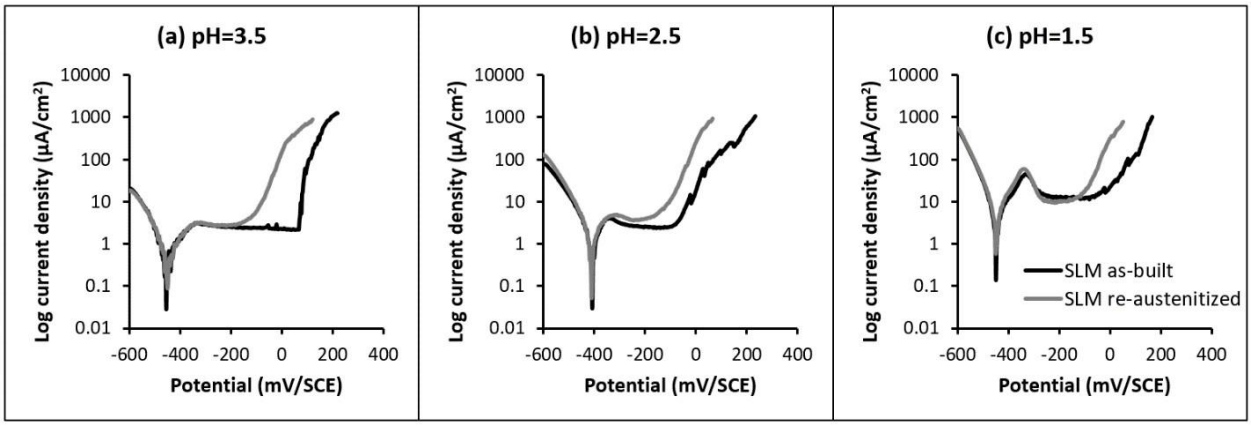

Figure 3. 4: Comparison of the electrochemical behavior of the as-built SLM-ed steel and the re-austenitized SLM-ed steel in 30g/l NaCl solution at (a) pH=3.5, (b) pH=2.5 and (c) pH=1.5.

Figure 3. 5 shows the polarization curves of the re-austenitized SLM-ed and the wrought steels at different pH in deaerated 30g/l NaCl solution. Similarly to **Figure 3. *4*** the polarization scan starts immediately at the immersion of the working electrode from -600 mV/ SCE (slightly cathodic potential) at 0.1 mV/min scan rate. The corrosion potential is different for the two steels. It tends to more noble values for the re-austenitized SLM-ed steel. In addition, it is noticed that at the corrosion potential the current density is almost ten times higher for the wrought steel. Furthermore, the general corrosion characterized by the anodic peak current density was more pronounced in the wrought steel. At pH=3.5, both steels had an activation peak lower than 10 µA/cm^2 which means that they can be considered as passivated even close to the corrosion potential. At pH=2.5, the re-austenitized SLM-ed steel was still passivated while this wasn't the case for the wrought steel. The latter exhibited a very large active peak. As the pH decreased to 1.5, both steels were depassivated. However, the peak current density was significantly higher in intensity and much larger for the wrought steel.

It should be noted that both steels have almost similar martensitic structure. However, the sulfur content is much higher in the wrought steel (**Table 3. *1***), which results in higher density and size of MnS inclusions (**Table 3. *2***). Actually, MnS inclusions are not only possible preferential sites for pit initiation but also destabilize the passive film. This was proven by several studies, where authors found anodic activity in the vicinity of the MnS inclusions corresponding to the breakdown of passivity. It was explained by the deposition of sulfur species in the adjacent region that were liberated from the MnS dissolution. The deposited sulfur promoted the destabilization of the passive film [54–59]. Oudar *et al.* [59] studied the active/passive behavior of pure nickel related to the amount of adsorbed sulfur. They have found that the adsorbed sulfur had a catalytic effect on the rate of dissolution of metal in the

active region of the anodic curve. Furthermore, they showed that there was a critical concentration of adsorbed sulfur, slightly lower than a monolayer, which totally inhibit the passivation of nickel alloy.

On the other hand, the pitting potential was not significantly different; it was even slightly higher in the wrought steel. This result was unexpected since the MnS content was far higher in the wrought steel and would imply that the MnS inclusions didn't have any strong influence on the pitting behavior. Since the anodic scan rate used during these tests was slow, it is possible that there was enough time for the MnS inclusions to dissolve completely and for its exposed surface to passivate before reaching the pitting potential. As a result, these inclusions didn't affect the pitting resistance. Indeed, some authors reported that a preliminary electrochemical treatments were successful in removing the MnS inclusions leading to an improved pitting resistance [60,61]. One possible explanation for the slightly lower pitting potential for the re-austenitized SLM-ed steel would be its higher grain boundary density, since it has smaller grains, and the presence of porosities as shown in **Table 3. *2***. This suggests that the grain boundaries and porosities could be sites for pit initiation in these steels.

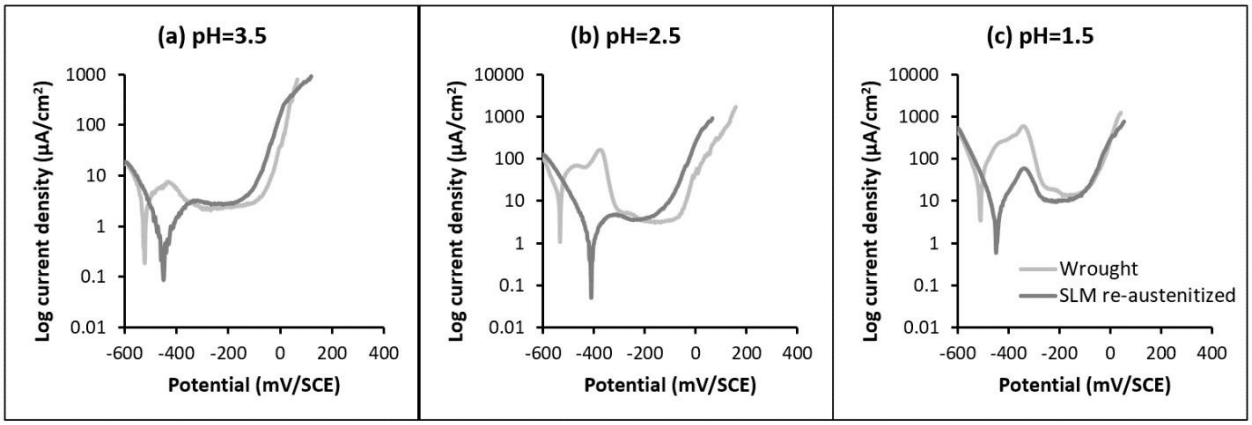

Figure 3. 5: Comparison of the electrochemical behavior of the wrought steel and the re-austenitized SLM-ed steel in 30g/l NaCl solution at (a) pH=3.5, (b) pH=2.5 and (c) pH=1.5.

3.4.3 Open circuit potential

The open circuit potential (OCP) of the three steels at pH equal to 2.5 is given in ***Figure 3. 6***. The OCP was measured for 5 hours. It is shown that at the beginning of immersion there is a sharp decrease of the OCP for all the steels. This is correlated to the dissolution of the passive film formed in contact with air [62]. After the sharp decrease of the OCP, the potential for both SLM-ed steels (as-built and re-austenitized) exhibit a slight increase with time of immersion. This increase of the OCP is an indication of a growing stable passive film and its enrichment in chromium oxide [63]. However, the wrought steel doesn't exhibit this increase of the OCP and the potential stabilizes after half an hour to a less

noble potential than the SLM-ed steels. This indicates that an unstable oxide film developed that doesn't have a protective property.

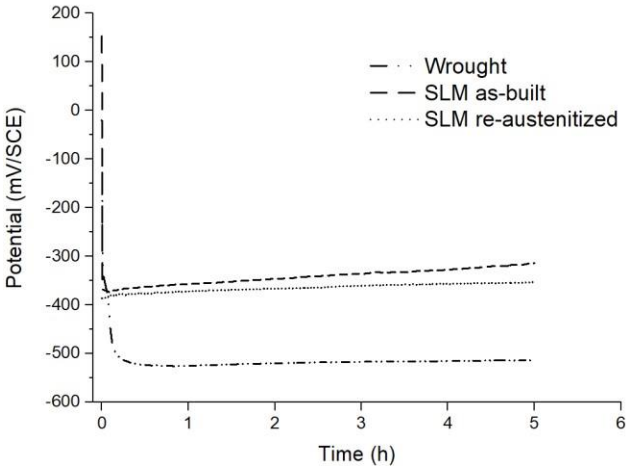

Figure 3. 6: OCP measurement over 5 hour period at pH=2.5 for the three steels. The data shows a slight increase in OCP for the SLM-ed steels and a stabilisation at less noble potential for the wrought steel.

After the test at OCP for 5 hours at pH equal to 2.5, the exposed surfaces were studied by optical microscopy ***(Figure 3. 7***). ***Figure 3. 7.b and.c*** show the exposed surfaces of as-built and re-austenitized steels. They both present an intact surface with no evidence of generalized corrosion. Some porosities can be seen that were initially present in the SLM-ed steels before corrosion. In contrast, the exposed surface of the wrought steel in ***Figure 3. 7.a*** was subjected to general corrosion. Small dark points that cover all the surface correspond to the dissolved MnS inclusions. The dissolution of MnS in stainless steels under free corrosion was reported by multiple authors [11,55,63]. According to Eklund [64], MnS inclusions can only exist between pH 4.8 and 13.8. Therefore, it is expected that MnS inclusions would dissolve at pH 2.5. These observations along with the OCP measurements confirm the results of the potentiodynamic scans at pH 2.5 that showed that the SLM-ed steels were passivated in contrast to the wrought steel.

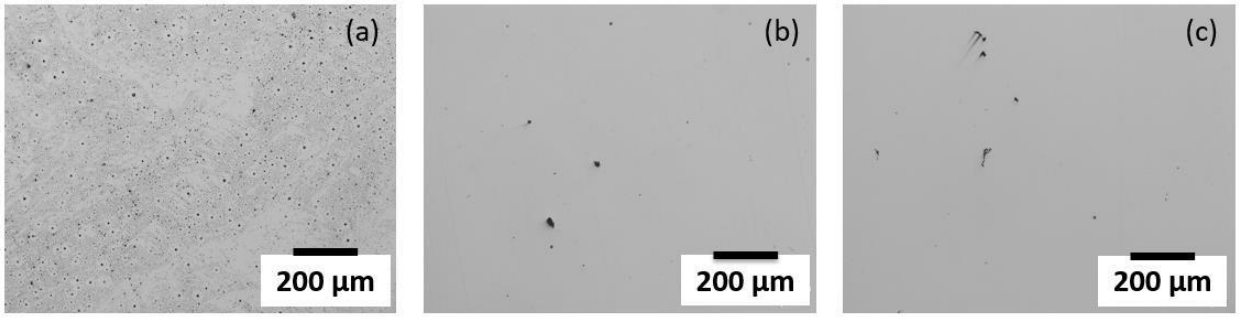

Figure 3. 7: Optical micrographs showing the exposed surface after OCP for 5 hours of (a) the wrought steel, (b) as-built SLM-ed steel and (c) re-austenitized SLM-ed steel.

3.4.4 XPS measurements

XPS measurements were performed in order to confirm the presence of a sulfur enrichment on the surface resulting from MnS dissolution. Only, the wrought steel was studied here. The surface states were studied in two conditions: after polishing to a mirror finish (polished) and after 24 hours of immersion at OCP in a deaerated solution containing 30 g/l NaCl at pH=2.5 (exposed). ***Figure 3. 8.a*** depicts the S 2p spectrum for both conditions. The polished surface had a small S2p peak at 161.55 eV. According to the literature, this component corresponds to MnS inclusions [65,66]. After immersion for 24 hours, the total sulfur signal became higher by a factor of six compared to the initial polished surface. This indicates that a large part of the surface was covered by sulfur containing species. Thus, the corrosion of this steel (OCP for 24 hours) resulted in an enrichment of sulfur species on the surface. In addition, three peaks, related to the S 2p level, can be identified on the exposed surface. The peak at 161.7 eV corresponds to the sulfur deposited on the surface that formed sulfides like FeS, CrS and Cu_2S [67–70]. The peak at 166.6 eV is a typical value for sulfite ions, more specifically ferrous sulfite $FeSO_3$ [68,71]. The peak at 168.26 eV was found to correspond to ferrous sulfate $FeSO_4$ [55,69,72]. ***Figure 3. 8.b*** shows the three components of S2p spectra of the exposed surface recorded in XPS angle resolved mode. For each component the ratio of the intensity at photoelectrons take-off angle of 25° to the one at 65° indicates how close chemical species are to the extreme surface. A "relative depth" d* of each component can be estimated using eq.2:

$$d^* = \frac{d}{\lambda} = \ln\left(\frac{I_{25°}}{I_{65°}}\right) \quad \text{(eq.2)}$$

Where d is the depth of a given layer, λ is the electron inelastic mean free path (considered the same in all the layers), and $I_{25°}$ and $I_{65°}$ are the intensities of a given component at 25° and 65° take-off angle

respectively. The relative depth, d*, is a dimensionless parameter that allows the localization of the

different layers with respect to each other. This relative depth is presented in ***Figure 3. 8.c*** and indicates that the sulfate component seems to be located at the extreme surface. The sulfide is the deepest component and the sulfite is at an intermediate depth. This is in agreement with previous studies that demonstrated that the sulfate is located in the outer part of the passive film [55], while the sulfide is more profound [67]. Based on these observations, a schematic distribution of the sulfur species is proposed in ***Figure 3. 8.d*** . ***Figure 3. 9*** shows the secondary electron micrograph of the exposed surface of the wrought 17-4 PH steel along with its EDS maps of manganese and sulfur. The EDS maps don't show any MnS inclusions indicating their complete dissolution after 24 hours of immersion at OCP in a deaerated solution containing 30 g/l NaCl at pH=2.5. These observations confirm that during immersion, the MnS inclusions dissolve and the sulfur liberated from the dissolution is deposited on the surface and changes the chemical composition of the passive film. Thus, it leads to a destabilization of the passive film, which is in agreement with previous studies on austenitic stainless steels [54–57]. This destabilization will result in the occurrence of general corrosion.

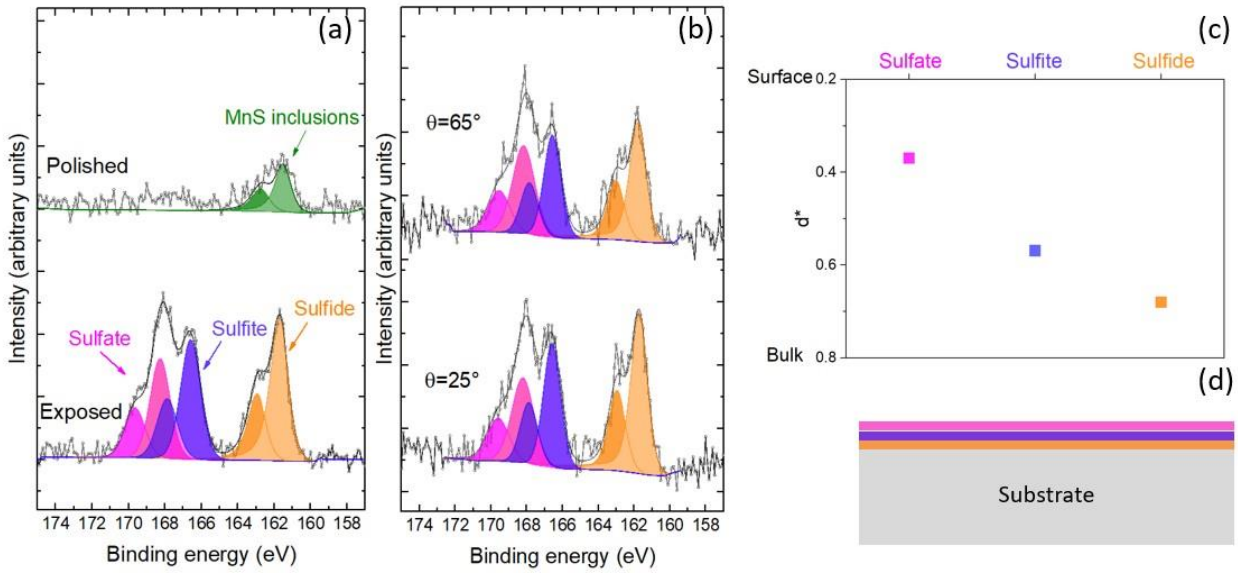

Figure 3. 8: (a) S2p spectra determined from XPS of the polished and exposed (24 hour at OCP in 30 g/l NaCl at pH=2.5) surfaces of the wrought 17-4 PH steel (b) S2p angle-resolved XPS analyses of the exposed surface at two photoelectron escape angles (Θ=25° and Θ=65°), (c) depth plot based on the ratio of intensities at Θ=25° and Θ=65° using equation 2, (d) schematic distribution of the sulphur species related to each component.

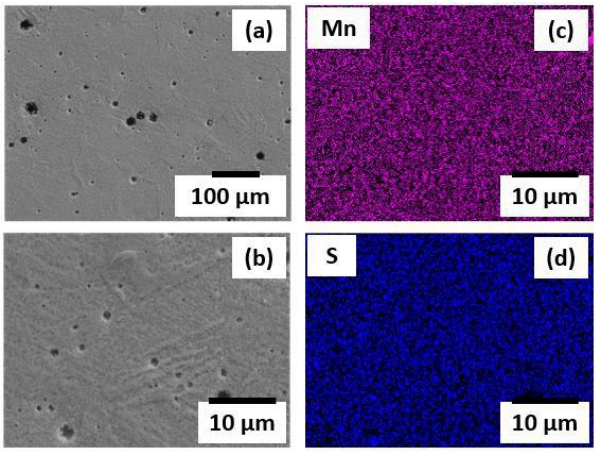

Figure 3. 9: (a) and (b) Secondary electron micrographs of the exposed surface of the wrought 17-4 PH steel. EDS maps of (c) manganese and (d) sulfur elements corresponding to image (b) showing a complete dissolution of MnS inclusions after 24 hours at OCP in 30 g/l NaCl at pH=2.5.

3.5 Conclusion

The aim of this study was to determine the corrosion behavior of SLM-ed 17-4 PH steel by electrochemical characterization. A series of potentiodynamic scans were performed at three different pH in deaerated 30 g/l NaCl solution. Measurements were conducted on the SLM-ed steel in the as-built condition and after re-austenitization treatment (both in the (Y-Z) plane) and on the wrought steel. The microstructure of the SLM-ed steel in the as-built condition was mostly ferritic and was due to the high cooling and heating rates that didn't allow enough time for the austenite to be formed. As a result, the delta ferrite formed during solidification didn't undergo any metallurgical transformation and was retained at room temperature. After re-austenization heat treatment, the SLM-ed steel was completely transformed to martensite. In addition, the wrought steel had a typical martensitic structure. The sulfur content that had a significant influence on the obtained results was higher in the wrought steel compared with the SLM-ed steels. Potentiodynamic measurements showed that:

1. The pH of depassivation was the same for the SLM-ed steel in the two conditions (as-built and re-austenitized) regardless of their microstructures. This suggests that the difference in microstructures had little effect on general corrosion resistance for both steels.
2. The pitting potential was higher in the as-built condition than the re-austenitized one. This was associated with the higher grain boundaries and dislocation densities.
3. The re-austenitized SLM-ed steel had a remarkably superior general corrosion resistance than the wrought steel. This was associated with the lower sulfur content, more specifically the lower MnS inclusion content in the re-austenitized SLM-ed steel. In the wrought steel, the dissolution of MnS inclusions led to a deposition of a sulfur rich layer in the adjacent regions

that promoted the destabilization of the passive film and thus deteriorated the general corrosion resistance. The XPS measurements confirmed the formation of sulfur species on the surface of the wrought steel.

4. Regarding the pitting corrosion behavior, although the MnS content was higher in the wrought steel, it was slightly more resistant than the re-austenitized SLM-ed steel. Thus, the MnS inclusions didn't have any effect on the pitting corrosion. The higher grain boundary density and the presence of porosities in the re-austenitized martensitic steel could contribute to this behavior.

3.6 References

[1] J.R. Davis, ASM International, eds., in: Stainless Steels, ASM International, Materials Park, Ohio, 1994: pp. 3–5.

[2] C.N. Hsiao, C.S. Chiou, J.R. Yang, Aging reactions in a 17-4 PH stainless steel, Materials Chemistry and Physics. 74 (2002) 134–142. https://doi.org/10.1016/S0254-0584(01)00460-6.

[3] W.D. Yoo, J.H. Lee, K.T. Youn, Y.M. Rhyim, Study on the Microstructure and Mechanical Properties of 17-4 PH Stainless Steel Depending on Heat Treatment and Aging Time, Solid State Phenomena. 118 (2006) 15–20. https://doi.org/10.4028/www.scientific.net/SSP.118.15.

[4] U.K. Viswanathan, S. Banerjee, R. Krishnan, Effects of aging on the microstructure of 17-4 PH stainless steel, Materials Science and Engineering: A. 104 (1988) 181–189. https://doi.org/10.1016/0025-5416(88)90420-X.

[5] B.C. Syrett, R. Viswanathan, S.S. Wing, J.E. Wittig, Effect of Microstructure on Pitting and Corrosion Fatigue of 17-4 PH Turbine Blade Steel in Chloride Environments, CORROSION. 38 (1982) 273–282. https://doi.org/10.5006/1.3577350.

[6] D. Nakhaie, M.H. Moayed, Pitting corrosion of cold rolled solution treated 17-4 PH stainless steel, Corrosion Science. 80 (2014) 290–298. https://doi.org/10.1016/j.corsci.2013.11.039.

[7] U.K. Mudali, A.K. Bhaduri, J.B. Gnanamoorthy, Localised corrosion behaviour of 17–4 PH stainless steel, Materials Science and Technology. 6 (1990) 7. https://doi.org/10.1179/mst.1990.6.5.475.

[8] G. Wranglen, Pitting and sulfide inclusion in steel, Corrosion Science. 14 (1974) 331–349.

[9] J.E. Castle, R. Ke, Studies by auger spectroscopy of pit initiation at the site of inclusions in stainless steel, Corrosion Science. 30 (1990) 409–428. https://doi.org/10.1016/0010-938X(90)90047-9.

[10] J.H. Park, Y. Kang, Inclusions in Stainless Steels – A Review, Steel Research International. 88 (2017) 1700130. https://doi.org/10.1002/srin.201700130.

[11] M.A. Baker, J.E. Castle, The initiation of pitting corrosion at MnS inclusions, Corrosion Science. 34 (1993) 667–682. https://doi.org/10.1016/0010-938X(93)90279-P.

[12] E.G. Webb, R.C. Alkire, Pit Initiation at Single Sulfide Inclusions in Stainless Steel, Journal of The Electrochemical Society. 149 (2002) B272. https://doi.org/10.1149/1.1474430.

[13] D.E. Williams, Elucidation of a Trigger Mechanism for Pitting Corrosion of Stainless Steels Using Submicron Resolution Scanning Electrochemical and Photoelectrochemical Microscopy, Journal of The Electrochemical Society. 145 (1998) 2664. https://doi.org/10.1149/1.1838697.

[14] R. Ke, Surface Analysis of Corrosion Pits Initiated at MnS Inclusions in 304 Stainless Steel, Journal of The Electrochemical Society. 139 (1992) 1573. https://doi.org/10.1149/1.2069458.

[15] J. Stewart, D.E. Williams, The initiation of pitting corrosion on austenitic stainless steel: on the role and importance of sulphide inclusions, Corrosion Science. 33 (1992) 457–474. https://doi.org/10.1016/0010-938X(92)90074-D.

[16] E.G. Webb, T. Suter, R.C. Alkire, Microelectrochemical Measurements of the Dissolution of Single MnS Inclusions, and the Prediction of the Critical Conditions for Pit Initiation on Stainless Steel, Journal of The Electrochemical Society. 148 (2001) B186. https://doi.org/10.1149/1.1360205.
[17] D.E. Williams, Y.Y. Zhu, Explanation for Initiation of Pitting Corrosion of Stainless Steels at Sulfide Inclusions, Journal of The Electrochemical Society. 147 (2000) 1763. https://doi.org/10.1149/1.1393431.
[18] Q. Meng, G.S. Frankel, H.O. Colijn, S.H. Goss, Stainless-steel corrosion and MnS inclusions, Nature. 424 (2003) 389–390. https://doi.org/10.1038/424389b.
[19] Q. Meng, G.S. Frankel, H.O. Colijn, S.H. Goss, High-Resolution Characterization of the Region Around Manganese Sulfide Inclusions in Stainless Steel Alloys, CORROSION. 60 (2004) 346–355. https://doi.org/10.5006/1.3287741.
[20] C.T. Kwok, H.C. Man, F.T. Cheng, Cavitation erosion and pitting corrosion of laser surface melted stainless steels, Surface and Coatings Technology. 99 (1998) 295–304. https://doi.org/10.1016/S0257-8972(97)00624-5.
[21] C. Carboni, P. Peyre, G.B.E. Ranger, C. Lemaitre, Influence of high power diode laser surface melting on the pitting corrosion resistance of type 316L stainless steel, Journal of Materials Science. (2002) 3715–3723.
[22] N. Guo, M.C. Leu, Additive manufacturing: technology, applications and research needs, Frontiers of Mechanical Engineering. 8 (2013) 215–243. https://doi.org/10.1007/s11465-013-0248-8.
[23] J.-P. Kruth, M.-C. Leu, T. Nakagawa, Progress in additive manufacturing and rapid prototyping, Cirp Annals. 47 (1998) 525–540. https://doi.org/10.1016/S0007-8506(07)63240-5.
[24] L.E. Murr, E. Martinez, K.N. Amato, S.M. Gaytan, J. Hernandez, D.A. Ramirez, P.W. Shindo, F. Medina, R.B. Wicker, Fabrication of Metal and Alloy Components by Additive Manufacturing: Examples of 3D Materials Science, Journal of Materials Research and Technology. 1 (2012) 42–54. https://doi.org/10.1016/S2238-7854(12)70009-1.
[25] T. Niendorf, S. Leuders, A. Riemer, H.A. Richard, T. Tröster, D. Schwarze, Highly Anisotropic Steel Processed by Selective Laser Melting, Metallurgical and Materials Transactions B. 44 (2013) 794–796. https://doi.org/10.1007/s11663-013-9875-z.
[26] S. Dadbakhsh, B. Vrancken, J.-P. Kruth, J. Luyten, J. Van Humbeeck, Texture and anisotropy in selective laser melting of NiTi alloy, Materials Science and Engineering: A. 650 (2016) 225–232. https://doi.org/10.1016/j.msea.2015.10.032.
[27] H.K. Rafi, D. Pal, N. Patil, T.L. Starr, B.E. Stucker, Microstructure and Mechanical Behavior of 17-4 Precipitation Hardenable Steel Processed by Selective Laser Melting, Journal of Materials Engineering and Performance. 23 (2014) 4421–4428. https://doi.org/10.1007/s11665-014-1226-y.
[28] S. Cheruvathur, E.A. Lass, C.E. Campbell, Additive Manufacturing of 17-4 PH Stainless Steel: Post-processing Heat Treatment to Achieve Uniform Reproducible Microstructure, JOM. 68 (2016) 930–942. https://doi.org/10.1007/s11837-015-1754-4.
[29] M. Alnajjar, F. Christien, K. Wolski, C. Bosch, Evidence of austenite by-passing in a stainless steel obtained from laser melting additive manufacturing, Additive Manufacturing. (2018). https://doi.org/10.1016/j.addma.2018.11.004.
[30] Q. Chao, V. Cruz, S. Thomas, N. Birbilis, P. Collins, A. Taylor, P.D. Hodgson, D. Fabijanic, On the enhanced corrosion resistance of a selective laser melted austenitic stainless steel, Scripta Materialia. 141 (2017) 94–98. https://doi.org/10.1016/j.scriptamat.2017.07.037.
[31] M.J.K. Lodhi, K.M. Deen, W. Haider, Corrosion behavior of additively manufactured 316L stainless steel in acidic media, Materialia. (2018). https://doi.org/10.1016/j.mtla.2018.06.015.
[32] S.-H. Sun, T. Ishimoto, K. Hagihara, Y. Tsutsumi, T. Hanawa, T. Nakano, Excellent mechanical and corrosion properties of austenitic stainless steel with a unique crystallographic lamellar

microstructure via selective laser melting, Scripta Materialia. 159 (2019) 89–93. https://doi.org/10.1016/j.scriptamat.2018.09.017.
[33] M.R. Stoudt, R.E. Ricker, E.A. Lass, L.E. Levine, Influence of Postbuild Microstructure on the Electrochemical Behavior of Additively Manufactured 17-4 PH Stainless Steel, JOM. 69 (2017) 506–515. https://doi.org/10.1007/s11837-016-2237-y.
[34] R.F. Schaller, J.M. Taylor, J. Rodelas, E.J. Schindelholz, Corrosion Properties of Powder Bed Fusion Additively Manufactured 17-4 PH Stainless Steel, CORROSION. 73 (2017) 796–807. https://doi.org/10.5006/2365.
[35] F. Christien, D. Fortes, M. Alnajjar, M. Telling, Solid state phase transformations at very high temperature in a martensitic stainless steel, STFC ISIS Neutron and Muon Source. (2018). https://doi.org/10.5286/ISIS.E.90682570.
[36] G.R. Stibitz, Energy of lattice distortion, Physical Review. 49 (1936) 859–891.
[37] F.E. Haworth, Energy of Lattice Distortion in Cold Worked Permalloy, Phys. Rev. 52 (1937) 613–620. https://doi.org/10.1103/PhysRev.52.613.
[38] F. Christien, M.T.F. Telling, K.S. Knight, R. Le Gall, A method for the monitoring of metal recrystallization based on the in-situ measurement of the elastic energy release using neutron diffraction, Review of Scientific Instruments. 86 (2015) 053901. https://doi.org/10.1063/1.4919414.
[39] A.C. Larson, R.B. Von Dreele, General structure analysis system, Los Alamos National Laboratory Report, 1994.
[40] B.H. Toby, EXPGUI , a graphical user interface for GSAS, J Appl Crystallogr. 34 (2001) 210–213. https://doi.org/10.1107/S0021889801002242.
[41] T. Nyyssönen, M. Isakov, P. Peura, V.-T. Kuokkala, Iterative Determination of the Orientation Relationship Between Austenite and Martensite from a Large Amount of Grain Pair Misorientations, Metall and Mat Trans A. 47 (2016) 2587–2590. https://doi.org/10.1007/s11661-016-3462-2.
[42] F. Christien, M.T.F. Telling, K.S. Knight, Neutron diffraction in situ monitoring of the dislocation density during martensitic transformation in a stainless steel, Scripta Materialia. 68 (2013) 506–509. https://doi.org/10.1016/j.scriptamat.2012.11.031.
[43] R. Coppola, P. Lukáš, P. Mikula, M. Vrána, Neutron-diffraction line broadening in a tempered martensitic steel for fusion reactors, Physica B: Condensed Matter. 241–243 (1997) 1261–1263. https://doi.org/10.1016/S0921-4526(97)00841-7.
[44] K. Macek, P. Lukáš, J. Janovec, P. Mikula, P. Strunz, M. Vrána, M. Zaffagnini, Austenite content and dislocation density in electron-beam welds of a stainless maraging steel, Materials Science and Engineering: A. 208 (1996) 131–138. https://doi.org/10.1016/0921-5093(95)10047-4.
[45] A.U. Malik, S.A. Fozan, Crevice corrosion behavior of AISI 316L SS in arabian gulf seawater, 1993.
[46] B. Baroux, Y. Bréchet, J. Charles, La corrosion des métaux passivité et corrosion localisée, L'Usine nouvelle : Dunod, Paris, 2014.
[47] M.B. Ives, Metallography of pitting corrosion, Materials Characterization. 28 (1992) 257–270. https://doi.org/10.1016/1044-5803(92)90015-A.
[48] V. Vignal, S. Ringeval, S. Thiébaut, K. Tabalaiev, C. Dessolin, O. Heintz, F. Herbst, R. Chassagnon, Influence of the microstructure on the corrosion behaviour of low-carbon martensitic stainless steel after tempering treatment, Corrosion Science. 85 (2014) 42–51. https://doi.org/10.1016/j.corsci.2014.03.036.
[49] S.G. Wang, C.B. Shen, K. Long, H.Y. Yang, F.H. Wang, Z.D. Zhang, Preparation and Electrochemical Corrosion Behavior of Bulk Nanocrystalline Ingot Iron in HCl Acid Solution, J. Phys. Chem. B. 109 (2005) 2499–2503. https://doi.org/10.1021/jp046297v.
[50] B. Hadzima, M. Janeček, Y. Estrin, H.S. Kim, Microstructure and corrosion properties of ultrafine-grained interstitial free steel, Materials Science and Engineering: A. 462 (2007) 243–247. https://doi.org/10.1016/j.msea.2005.11.081.

[51] K.D. Ralston, N. Birbilis, Effect of Grain Size on Corrosion: A Review, CORROSION. 66 (2010) 075005-075005–13. https://doi.org/10.5006/1.3462912.
[52] M. Pisarek, P. Kędzierzawski, M. Janik-Czachor, K.J. Kurzydłowski, Effect of hydrostatic extrusion on passivity breakdown on 303 austenitic stainless steel in chloride solution, J Solid State Electrochem. 13 (2009) 283–291. https://doi.org/10.1007/s10008-007-0488-9.
[53] Y. Hao, B. Deng, C. Zhong, Y. Jiang, J. Li, Effect of surface mechanical attrition treatment on corrosion behavior of 316 stainless steel, J. Iron Steel Res. Int. 16 (2009) 68–72. https://doi.org/10.1016/S1006-706X(09)60030-3.
[54] B. Vuillemin, X. Philippe, R. Oltra, V. Vignal, L. Coudreuse, L.C. Dufour, E. Finot, SVET, AFM and AES study of pitting corrosion initiated on MnS inclusions by microinjection, Corrosion Science. 45 (2003) 1143–1159. https://doi.org/10.1016/S0010-938X(02)00222-6.
[55] H. Krawiec, V. Vignal, O. Heintz, R. Oltra, J.-M. Olive, Influence of the Chemical Dissolution of MnS Inclusions on the Electrochemical Behavior of Stainless Steels, Journal of The Electrochemical Society. 152 (2005) B213. https://doi.org/10.1149/1.1924172.
[56] S.-T. Kim, Y.-S. Park, Effect of Sulfur Content of Copper-Containing Austenitic Stainless Steels on Corrosion Behavior in Concentrated Sulfuric Acid—Part 2, CORROSION. 64 (2008) 496–508. https://doi.org/10.5006/1.3278486.
[57] A. Elbiache, P. Marcus, The role of molybdenum in the dissolution and the passivation of stainless steels with adsorbed sulphur, Corrosion Science. 33 (1992) 261–269. https://doi.org/10.1016/0010-938X(92)90150-2.
[58] P. Marcus, A. Teissier, J. Oudar, The influence of sulphur on the dissolution and the passivation of a nickel-iron alloy—I. electrochemical and radiotracer measurements, Corrosion Science. 24 (1984) 259–268. https://doi.org/10.1016/0010-938X(84)90012-X.
[59] J. Oudar, P. Marcus, Role of adsorbed sulphur in the dissolution and passivation of nickel and nickel-sulphur alloys, Applications of Surface Science. 3 (1979) 48–67. https://doi.org/10.1016/0378-5963(79)90060-6.
[60] N. Hara, K. Hirabayashi, Y. Sugawara, I. Muto, Improvement of Pitting Corrosion Resistance of Type 316L Stainless Steel by Potentiostatic Removal of Surface MnS Inclusions, International Journal of Corrosion. 2012 (2012) 1–6. https://doi.org/10.1155/2012/482730.
[61] S. Hastuty, E. Tada, A. Nishikata, Y. Tsutsumi, T. Hanawa, Improvement of Pitting Corrosion Resistance of Type 430 Stainless Steel by Electrochemical Treatments in a Concentrated Nitric Acid, ISIJ Int. 54 (2014) 199–205. https://doi.org/10.2355/isijinternational.54.199.
[62] N. Alonso-Falleiros, S. Wolynec, Correlation between Corrosion Potential and Pitting Potential for AISI 304L Austenitic Stainless Steel in 3.5% NaCl Aqueous Solution, Materials Research. 5 (2002) 77–84. https://doi.org/10.1590/S1516-14392002000100013.
[63] E.A. Ferreira, R.D. Noce, C.S. Fugivara, A.V. Benedetti, Evaluation of 316L Stainless Steel Corrosion Resistance in Solution Simulating the Acid Hydrolysis of Biomass, Journal of The Electrochemical Society. 158 (2011) C95. https://doi.org/10.1149/1.3554728.
[64] G.S. Eklund, Initiation of Pitting at Sulfide Inclusions in Stainless Steel, J. Electrochem. Soc. 121 (1974) 467. https://doi.org/10.1149/1.2401840.
[65] H. Franzen, C. Sterner, The X-ray photoelectron spectra of MnS, MnSe, and MnTe, Journal of Solid State Chemistry. 25 (1978) 227–230. https://doi.org/10.1016/0022-4596(78)90107-X.
[66] P. Tiwari, G. Malik, R. Chandra, Phase-dependent structural and electrochemical properties of single crystalline MnS thin films deposited by DC reactive sputtering, Journal of Applied Physics. 124 (2018) 195106. https://doi.org/10.1063/1.5053875.
[67] C. Duret-Thual, D. Costa, W.P. Yang, P. Marcus, The role of thiosulfates in the pitting corrosion of Fe-17Cr alloys in neutral chloride solution: Electrochemical and XPS study, Corrosion Science. 39 (1997) 913–933. https://doi.org/10.1016/S0010-938X(97)81158-4.

[68] W.Y. Lai, W.Z. Zhao, Z.F. Yin, J. Zhang, EIS and XPS studies on passive film of AISI 304 stainless steel in dilute sulfuric acid solution: Passive film of AISI 304 stainless steel, Surf. Interface Anal. 44 (2012) 418–425. https://doi.org/10.1002/sia.3819.

[69] P. Marcus, J.M. Grimal, The antagonistic roles of chromium and sulphur in the passivation of Ni□Cr□Fe alloys studied by XPS and radiochemical techniques, Corrosion Science. 31 (1990) 377–382. https://doi.org/10.1016/0010-938X(90)90134-Q.

[70] M.C. Biesinger, B.R. Hart, R. Polack, B.A. Kobe, R.St.C. Smart, Analysis of mineral surface chemistry in flotation separation using imaging XPS, Minerals Engineering. 20 (2007) 152–162. https://doi.org/10.1016/j.mineng.2006.08.006.

[71] A. Galtayries, C. Cousi, S. Zanna, P. Marcus, SO2 adsorption at room temperature on Ni(111) surface studied by XPS, Surf. Interface Anal. 36 (2004) 997–1000. https://doi.org/10.1002/sia.1821.

[72] Comparative XPS analyses of passive layers composition formed on Duplex 2205 SS after standard and high-current-density electropolishing, Teh. Vjesn. 23 (2016). https://doi.org/10.17559/TV-20141107094438.

Chapter 4A comparative study of hydrogen embrittlement of selective laser melted and wrought 17-4 PH stainless steel

Table of contents

(The work presented in this chapter will be submitted to Materials Science Engineering A.)

4.1 Abstract

In this study, the hydrogen embrittlement of 17-4 PH stainless steel produced by selective laser melting (SLM) was investigated. The microstructure of SLM-ed 17-4 PH stainless steel was found to be fully ferritic, in contrast to the wrought martensitic steel. This finding was correlated to the high cooling and heating rates that suppressed the austenite formation and retained the delta ferrite to room temperature. The hydrogen embrittlement was evaluated by performing slow strain rate tensile tests under cathodic charging. Both wrought and SLM-ed steels were aged at 580°C for 4 hours. It was found that SLM-ed 17-4 PH steel was more susceptible to hydrogen embrittlement compared to its wrought counterpart. This was due to the difference in microstructures, more specifically grain size. The crack initiation and propagation was much easier in the ferritic SLM-ed steel than in the martensitic wrought steel. The fracture in both steels was due to a significant subcritical crack growth followed by an overload fracture. The fracture surface of the wrought steel showed a brittle intergranular fracture mode at the borders and a ductile mode at the center. The brittle fracture mode was associated with the slow subcritical crack growth, while the ductile mode was due to the overload fracture. On the other hand, in the SLM-ed steel, both the subcritical crack growth and the final overload fracture were obtained by transgranular cleavage. For the SLM-ed steel, the crack initiation occurs through a purely decohesive mechanism in which the brittle crack initiation stress is decreased when the hydrogen concentration beneath the surface is increased. For the wrought steel, plastic deformation is needed to initiate the intergranular crack. It is suggested that the crack initiation requires a certain hydrogen concentration in the grain boundary, which is achieved through the dragging of hydrogen by mobile dislocations to the grain boundaries.

4.2 Introduction

Precipitation hardenable (PH) stainless steels are widely used in a variety of applications such as chemical plants, oil and gas industry and marine environment due to their combined high strength and good corrosion resistance [1–4]. 17-4 PH is a precipitation hardenable stainless steel that contains 15-17.5 wt.% of chromium, 3-5 wt.% of nickel and 3-5 wt.% of copper. This steel exhibits a martensitic microstructure after a solution heat treatment and quenching. A subsequent aging treatment is usually applied in the temperature range 480-620°C, which results in strengthening due to the precipitation of copper rich particles in the martensitic matrix [4–6]. 17-4 PH is the most popular grade among the precipitation hardenable stainless steels because it possesses a relatively high tensile strength, fracture toughness and corrosion resistance [3,4].

Although this steel has good corrosion properties, it can still be susceptible to hydrogen embrittlement [7–10]. Chiang *et al.* [7] found that the solution treated steel had better resistance to hydrogen embrittlement than the peak aged steel. This was attributed to copper precipitation in the latter that induced its brittle fracture. In contrast, Hayashi *et al.* [8] showed that solution treated and sub-aged steels were more susceptible than peak-aged and over-aged steels to hydrogen embrittlement under low hydrogen content. In this study, the copper precipitation had a beneficial effect by hydrogen trapping. However, this effect disappeared when the hydrogen was trapped both at the precipitates and the martensitic matrix. Shen *et al.* [9] studied the effect of solution treatment temperature on hydrogen susceptibility of 17-4 PH steel. They found that susceptibility decreases and then increases as the solution-treatment temperature increased. This behavior was due to the combined effect of prior austenitic grain size and the state of copper precipitation. Based on these findings, the copper effect on hydrogen susceptibility of this steel is still unclear. Furthermore, the strength level might have an effect but was not considered. Murray *et al.* [10] investigated the hydrogen embrittlement of a precipitation hardenable stainless steel similar to 17-4 PH steel and found that the hydrogen susceptibility increased with the increase in strength. For all these studies, the hydrogen embrittlement was evaluated by a loss in ductility and reduction of fracture stress. In addition, fracture surfaces changed from ductile mode for the hydrogen free specimens to brittle mode, such as quasi-cleavage or intergranular, for the hydrogen charged specimens.

Recently, stainless steels have been produced by additive manufacturing (AM). This process has been gaining increased attention because it allows objects, usually having a complex geometry, to be directly fabricated layer by layer according to a computer-aided design (CAD) model [11,12]. Selective laser melting (SLM) is a technique of AM that consists of producing metallic components by laser melting of metallic powders [13–15]. Many researches have been conducted on the microstructure of stainless steels obtained by SLM. They have shown that their microstructures were highly anisotropic and in some cases had different phase constitution from their wrought counterparts [16–20]. Consequently, the corrosion properties of AM stainless steels, in particular their hydrogen embrittlement susceptibility, are expected to be different from their wrought counterparts.

The corrosion properties of AM stainless steels need to be investigated in order to prevent the failure of components during service. In this study, the hydrogen embrittlement of 17-4 PH stainless steel produced by SLM was investigated. Tensile tests were performed on charged and uncharged specimens. Furthermore, the effect of the strain rate on the hydrogen embrittlement was investigated. In addition, a comparison of the hydrogen embrittlement behavior between wrought and SLM-ed

steels was made. The same ageing treatment was conducted on the two steels so as to obtain similar yield strength.

4.3 Experimental procedures

4.3.1 Material

The materials used in this study were wrought and SLM-ed 17-4 PH steels. The wrought material was a commercial bar from UGINE (cast # 818025). It was studied after a solution heat treatment at 1050°C for 1 hour followed by a water quench, then aged at 580°C for 4 hours. The SLM-ed steel was fabricated in an SLM machine of type EOS M270. The fabrication was done in an argon purging environment. Cylinders were fabricated horizontally, i.e. with their axis perpendicular to building direction Z. Tensile specimens were machined from the cylinders and then aged at 580°C for 4 hours. The chemical composition of both materials is given in **Table 4. *1***. The full composition of the wrought material is indicated (data from the steel provider) in the first line of **Table 4. *1***. Additional measurements were conducted on both wrought and SLM-ed materials (lines 2 and 3 of **Table 4. *1***). These measurements were carried out using X-ray fluorescence (XRF) (FISCHERSCOPE X-Ray XAN-FD) for elements Ni, Cr and Cu, and using combustion elemental analysis (CEA) for C, S (LECO CS 444/LS), N and O (LECO TC-436).

Table 4. 1: Chemical composition (wt. %) of wrought and SLM-ed 17-4 PH stainless steels.

17-4 PH		C	Ni	Si	P	Mn	Cr	Cu	S	N	O	Nb F	e
Wrought	Provider Data sheet	0.031	4.82	0.31	0.016	0.81	15.61	3.12	0.02	-	-	0.21	Bal.
	XRF/CEA	0.026	4.95	-	-	-	16.18	3.09	0.021	0.033	0.007	-	Bal.
SLM-ed	XRF/CEA	0.03	4.16	-	0.008	-	16.11	3.73	0.003	0.033	0.046	0.3	Bal.

4.3.2 Microstructural characterization

SEM Zeiss SUPRA55VP was used at 20 kV for microstructural observations, including electron backscatter diffraction (EBSD). For the EBSD preparation, samples were polished up to 1200 grit, followed by electropolishing using 94% ethanol + 6% perchloric acid as electrolyte at 25 V for 60 s.

4.3.3 Tensile tests in air

Two specimen geometries were used for tensile tests in air: smooth axisymmetric specimens with a gage length of 10 mm and a diameter of 5 mm and notched axisymmetric specimens with a 1 mm deep circumferential notch having a root radius of 0.4 mm and an angle of 35°, which was cut in the center of the gage length. The notched specimens were used in order to study the effect of the notch on the fracture mode. Both smooth and notched specimens were tested at room temperature. The displacement rate used during testing was 10^{-5} mm/s.

4.3.4 Tensile tests under cathodic charging

Some specimens were only hydrogen charged during the slow strain rate tensile tests until fracture (without any pre-charging) and will be denoted as "charged" specimens. Other specimens were hydrogen pre-charged for 24 hours before the slow strain rate tensile test was started. Then, the hydrogen charging was maintained during the tensile test until specimen fracture. These specimens will be denoted as "pre+charged" specimens. All specimens were cathodically charged at -800 mV versus the saturated calomel electrode (SCE) using a PGP201 potentiostat. The charging was done in (30 g/l NaCl + 0.4 g/l sodium acetate) solution at pH 1.5. The solution was deaerated continuously by a nitrogen flux. A platinum plate was used as a counter electrode. The specimens were polished up to 1 µm diamond finish. They were rinsed with water and cleaned with ethanol before each test. The specimen was then installed in the electrochemical cell on the tensile machine. The cell was purged for 10 min with nitrogen gas before introducing the solution. Once the three electrodes were immerged the cathodic potential was directly applied. The displacement rates applied were 10^{-6} mm/s, 10^{-5} mm/s and 10^{-4} mm/s. This gives real strain rates of approximately $9\ 10^{-9}$ /s, $2\ 10^{-7}$ /s and $3\ 10^{-6}$ /s (see appendix 4). These strain rates were estimated from the ratio of elongation at fracture to fracture time. The tensile machine used for both charged and uncharged specimens was of type SCHENCK coupled with the Wavematrix software. The recorded parameters are the load and the displacement using linear variable differential transformer (LVDT) sensor. Since the LVDT sensor was placed outside the electrochemical cell, a correction of the raw data was applied so as to obtain the correct deformation in the elastic domain (Appendix 5). After the SSRT test was finished, the specimen was unmounted and cleaned with ethanol. The fracture surface was then examined by scanning electron microscopy.

4.3.5 Electrochemical permeation test

Electrochemical permeation was used to investigate the hydrogen diffusion in the studied materials. The method used is that developed by Devanathan and Stachurski [21]. The specimen was cathodically

charged by applying a potential of -1200 mV/SCE on the entry side to maintain a constant hydrogen concentration. The potential applied on the exit side was 0 mV/SCE, which allowed complete oxidation of hydrogen. This corresponds to a zero hydrogen concentration condition on the exit side. The equipment used for applying the required potentials were VoltaLab PGP201 potentiostats. The solution used in both entry and exit cells was 0.1 M NaOH continuously deaerated with nitrogen. The permeation tests were performed at room temperature. The auxiliary electrodes were platinum plates and the reference electrodes used were saturated calomel electrodes (SCE). The working electrode was a thin sample of the tested steels. The two sides of the sample were polished down to 0.25 µm diamond finish. After preparation, the obtained thickness was between 200 and 400 µm. The sample was then placed and sealed between the two electrochemical cells. A circular area of 0.785 cm^2 (1 cm of diameter) was exposed to the solution on both sides.

The effective hydrogen diffusivity, D_{eff} (m^2/s), was estimated by the time lag method applied on the rising permeation current transient for these boundary conditions [21]:

$$D_{eff} = \frac{e^2}{6 t_L}$$

where e is the specimen thickness and t_L is the time lag corresponding to the point on the hydrogen permeation curve where the current density at the exit side I is equal to 0.63 I_{ss}, I_{ss} being the steady-state current density. The permeation curves presented in this paper represent the normalized intensity (I/I_{ss}) on the exit side versus the normalized time (t/e^2).

4.4 Results and discussion

4.4.1 Microstructural analysis

Figure 4. 1.a shows the EBSD orientation map of the wrought 17-4 PH steel obtained after a solution heat treatment at 1050°C for 1 hour and a water quench, then followed by an aging heat treatment at 580°c for 4 hours. It shows a well-defined martensitic microstructure with lathes of martensite gathered into blocks and the latter into packets inside a prior austenitic grain. The average prior austenitic grain size is approximately 20 µm. It is expected that this steel has undergone complete martensitic transformation upon water quenching from the solutionizing temperature.

Figure 4. 1.b and.c shows the EBSD maps of the SLM-ed 17-4 PH steel in the (X-Z) and (X-Y) planes respectively. The (X-Z) and (X-Y) planes are respectively the planes parallel and perpendicular to the building direction Z. It is also noted here that the direction X is that of stress for tensile tests. In contrast to the wrought steel, the EBSD maps reveal a coarse grain microstructure with no evidence of lathes

of martensite. It has been shown in a previous paper [16] that this SLM-ed steel in the as-built state has a ferritic microstructure, more specifically δ ferrite. This is due to the high heating and cooling rates experienced during SLM construction that suppressed the transformation of δ ferrite to austenite at high temperature. Thus, the δ ferrite formed during solidification does not undergo any metallurgical transformation during the numerous heating and cooling stages of the construction. This process can be visualized as if δ ferrite had by-passed the austenite phase. As a result, the δ ferrite was retained until the end of the fabrication. More details of this by-passing phenomenon are given in [16]. This mechanism has been recently observed by Vunnam *et al.* [22] on the same material. The EBSD maps also show that the grain morphology is different in the (X-Z) plane (***Figure 4. 1.b***) and the (X-Y) plane (***Figure 4. 1.c***), which is related to the laser scanning strategy [20,23]. This difference in grain morphology between the planes might play a role in the hydrogen diffusion during tensile tests under hydrogen charging and will be discussed later. Microstructural changes resulting from the tempering heat treatment at 580°C for 4 hours, namely cooper-rich nanometer-size precipitation and potentially a small amount of reverted austenite, can't be observed at this magnification.

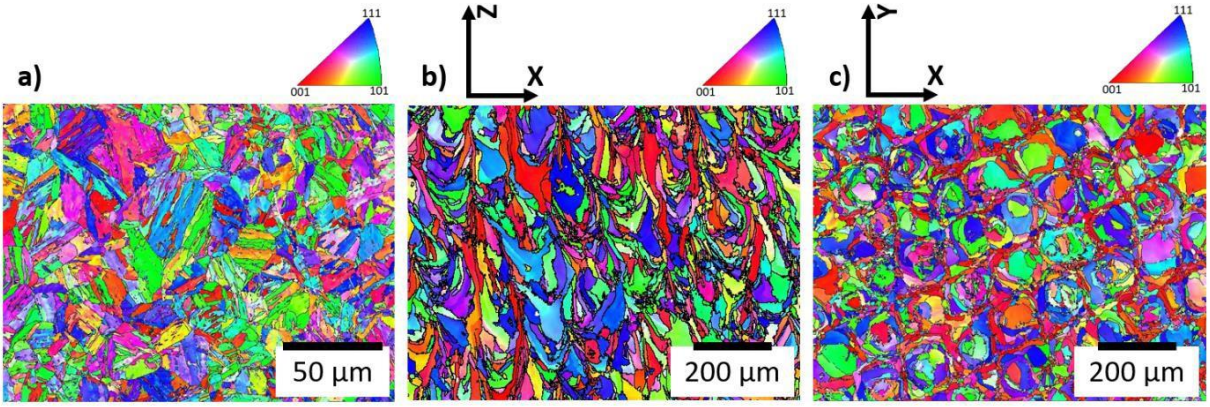

Figure 4. 1: EBSD orientation map of (a) wrought 17-4 PH steel showing a typical martensitic microstructure, (b) and (c) SLM-ed 17-4 PH steel showing coarse grain ferritic microstructure in the (X-Z) plane (b) and in the (X-Y) plane (c). Z is the building direction.

4.4.2 Tensile properties in air

Tensile tests in air were performed at room temperature on both smooth and notched specimens of wrought and SLM-ed steels. ***Figure 4. 2*** shows the engineering stress-strain curves obtained. The engineering stress was calculated from the ratio of load to minimum surface perpendicular to the load axis. The minimum diameter is approximately 5 mm for the smooth specimens and 3 mm at the notch root for the notched specimens. For the smooth specimens, both wrought and SLM-ed steels show a

significant elongation (21 to 26 %). The SLM-ed smooth specimen has slightly lower yield strength, ultimate tensile strength and strain to fracture. Nonetheless, the two steels can still be considered of comparable strength and "satisfactory" elongation. Since the ferritic SLM-ed steel has similar strength as the martensitic wrought steel, this implies that the martensitic structure has little effect on strengthening for this type of steel. This tends to show that the strength of this steel is mainly determined by the copper precipitation. ***Figure 4. 3*** shows the fracture surfaces of the wrought and SLM-ed steels obtained on smooth tensile specimens. Dimples were observed on the whole area of the fracture surface, which are typical ductile failure mode at room temperature. However, the dimples seem to be deeper and larger for the wrought steel. The wrought steel shows a typical ductile cup-and-cone fracture surface with three distinct regions: fibrous zone in the middle where the fracture initiated, the radial zone that shows a rough surface with radial marks diverging from the fibrous region and the shear lip zone. On the other hand, the SLM-ed steel doesn't show a typical ductile fracture. The main fracture mode observed on the entire surface is still ductile. However, some small brittle cleavage zones can be observed.

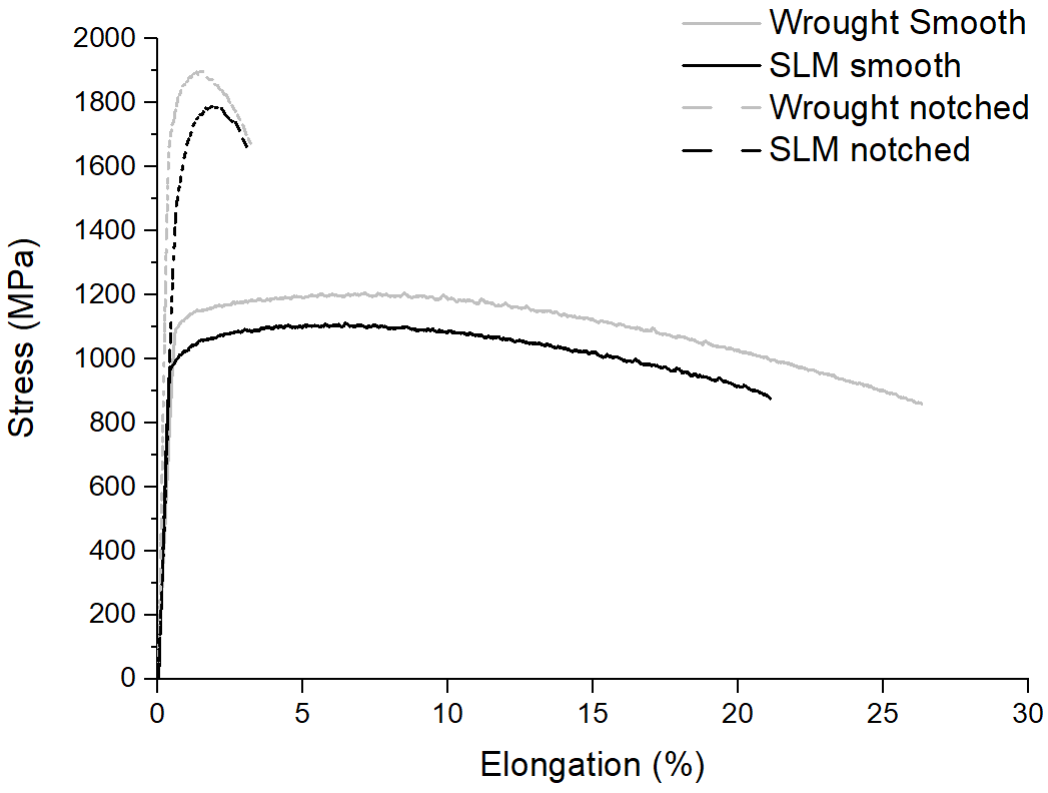

Figure 4. 2: Stress-strain curves of tensile tests in air of smooth and notched specimens of wrought and SLM-ed steels. The displacement rate used for all the tensile tests in air is 10-5 mm/s.

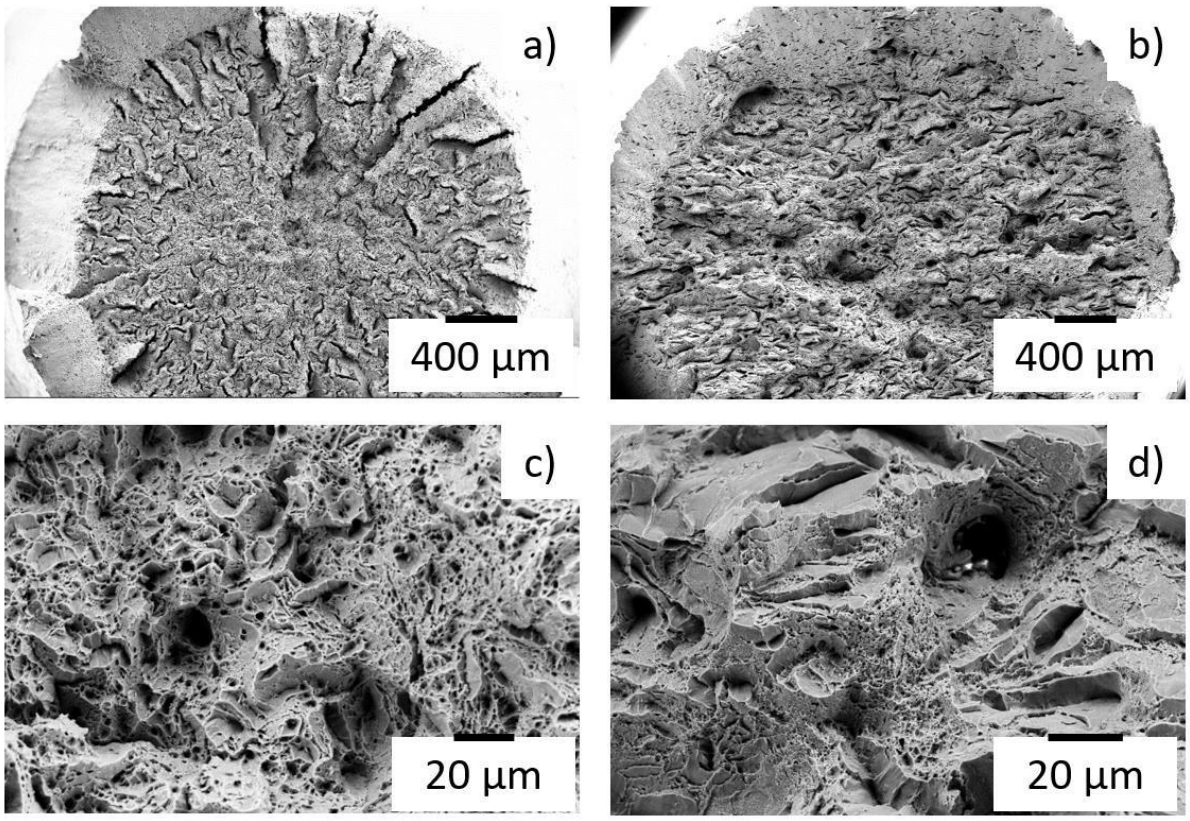

Figure 4. 3: Fracture surfaces after tensile tests in air of smooth specimens of: (a), (c) wrought steel showing a typical ductile cup-and-cone fracture and (b), (d) SLM-ed steel showing ductile behavior with small brittle cleavage zones.

The notched specimens showed a pronounced increase in the engineering tensile stress (calculated as uniaxial with respect to a reduced section at a notch) and reduction in elongation for the same strain as the smooth specimens. This was observed for both wrought and SLM-ed specimens and results from the stress triaxiality that develops ahead of the notch. In addition, the SLM-ed specimen had slightly lower yield strength and ultimate tensile strength than the wrought specimen, which is consistent with the observations on the smooth specimens. The fracture surfaces of the notched specimens are shown in ***Figure 4. 4***. The macroscopic fracture surface of the notched wrought steel, shown in ***Figure 4. 4.a***, reveals a ductile fracture mode with the three typical zones (fibrous, radial and shear lip zones). At higher magnification (***Figure 4. 4.c***), the radial zone shows a mixture of approximately 80% ductile and 20% brittle intergranular fracture. The intergranular fracture is along the prior austenitic grain boundaries. This observation implies that the martensitic wrought steel is only slightly notch sensitive because the fracture mode remained mostly ductile. On the other hand, the overall fracture surface of the SLM-ed notched steel in ***Figure 4. 4.b*** does not show a ductile fracture mode. At higher

magnification (***Figure 4. 4.d***), mainly brittle transgranular cleavage is observed. It appears that the notch had a drastic effect on the fracture mode for the ferritic SLM-ed steel.

It is well known that brittle fracture occurs in three stages: initiation of a crack, the initial extension of the crack and the crossing of the first obstacle, usually a grain boundary. The stress needed to overcome each stage is inversely proportional to the square root of the grain size d. Thus, the brittle

fracture stress $\sigma_{\blacklozenge}$ is inversely proportional to the square root of the grain size ($\sigma_{\blacklozenge} \propto \blacklozenge^{-1/2}$) [24]. This was demonstrated in the frame of dislocation theory of fracture and is described in details in ref. [25–27]. Considering the two studied steels, it can be seen from the EBSD maps in **Figure 4. *1*** that the α' grain size (martensitic grain size) for the wrought steel is much smaller than the δ grain size for the

SLM-ed steel. Thus, the brittle fracture stress $\sigma_{\blacklozenge}$ is much lower for the SLM-ed steel in comparison to the wrought steel. This implies that the SLM-ed ferritic steel requires lower stress to fracture in brittle mode than the martensitic wrought steel. The effect of the notch was to produce a higher tensile stress level that exceeded the brittle fracture stress in the SLM-ed steel. As a result, the fracture surface had mostly cleavage-like fracture mode. However, it seems that the stress level didn't reach the brittle fracture stress for the wrought steel. This resulted in a mostly ductile fracture mode.

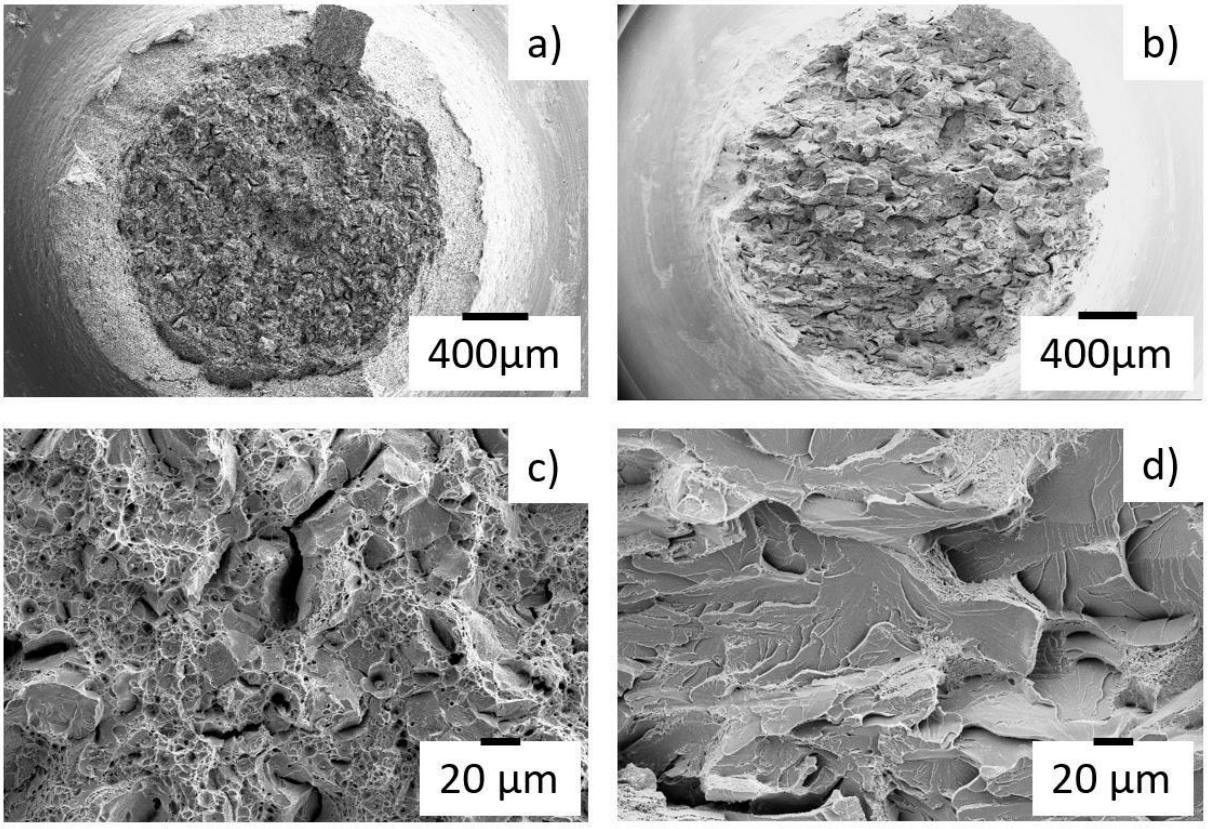

Figure 4. 4: Fracture surfaces after tensile tests in air of notched specimens of: (a), (c) wrought steel showing mainly ductile behavior with dimples and (b), (d) SLM-ed steel showing brittle behavior with cleavage.

4.4.3 Hydrogen permeation behavior

The permeation tests were conducted in order to study the hydrogen diffusion in the two steels. ***Figure 4. 5*** shows the hydrogen permeation curves of the wrought steel along an arbitrary direction and SLM-ed steel along two directions, parallel and perpendicular to the building direction Z. During tensile tests under hydrogen charging of cylindrical specimens, hydrogen charging occurs along multiple directions. For the wrought steel, the microstructure, and hence, the hydrogen diffusion is isotropic, i.e. the same for all directions. Thus, one permeation test is enough to determine the hydrogen diffusion of this steel. However, for the SLM-ed steel, ***Figure 4. 1.b and .c*** show that the microstructure is not isotropic. According to the literature, the hydrogen diffusion might differ for the same steel with changes of microstructure such as grain shape and size [28–30]. Therefore, two directions were studied to check if the hydrogen diffusion is isotropic, i.e. the same in the two directions. In ***Figure 4. 5***, the normalized current density is plotted as a function of the normalized time. All the curves consisted of three stages: incubation stage preceding the breakthrough time, which corresponds to the time needed for the first hydrogen atoms to diffuse across the specimen's thickness, the transient stage where the permeation current increases and the steady-state stage where a constant hydrogen flux is reached. From these curves, the effective hydrogen diffusion coefficient can be calculated using the time lag method as explained previously. The results are listed in **Table 4. *2***. The diffusion coefficient was almost similar for the two directions of the SLM-ed steel. Thus, it can be considered that the hydrogen diffusion in the SLM-ed steel is isotropic. On the other hand, the hydrogen diffusion coefficient is about three times lower in the wrought steel than in the SLM-ed steel. This is correlated to its martensitic microstructure that presents more hydrogen trapping sites (dislocations and grain boundaries) than the ferritic microstructure of the SLM-ed steel [31]. However, it should be noted that the diffusion coefficient found for the ferritic SLM-ed steel is approximately two to three orders of magnitude lower than that of a typical ferritic microstructure: $1.19\,10^{-10}$ m^2/s in [32], $\sim 2\,10^{-10}$ m^2/s [33], $1.81\,10^{-10}$ m^2/s [34]. This could be due to additional trapping sites, possibly correlated to the formation of Cu-rich precipitates by the aging heat treatment (580°C-4 hours).

By using the effective diffusion coefficient calculated from the permeation tests, it is possible to estimate the hydrogen diffusion distance λ from the surface of the charged tensile specimens according to the equation $\lambda = \sqrt{2Dt}$. The value of t corresponds to the test duration from the onset of charging up to the specimen's fracture, which includes the 24 hours of pre-charging, if any. For example, the diffusion distance is 220 µm for the wrought pre+charged specimen tested at 10^{-4} mm/s. The diffusion distance is 365 µm for the SLM-ed pre+charged specimen tested at 10^{-4} mm/s. This simple

calculation shows that the specimens are not necessarily completely hydrogen charged (the hydrogen didn't reach the center of the specimens).

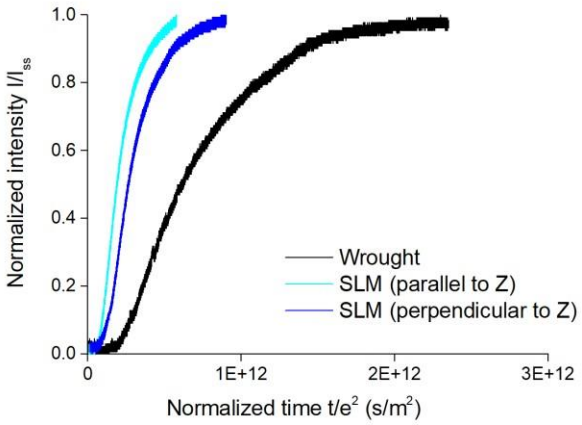

Figure 4. 5: Electrochemical hydrogen permeation curves at room temperature showing slightly faster diffusion for the SLM-ed steel.

Table 4. 2: The effective diffusion coefficient of hydrogen in wrought and SLM-ed steels determined from electrochemical permeation at room temperature.

Materials	D_{eff} (m^2 s^{-1})
Wrought	$2.3\ 10^{-13}$
SLM (parallel to Z)	$7.3\ 10^{-13}$
SLM (perpendicular to Z)	$5.1\ 10^{-13}$

4.4.4 Tensile tests under hydrogen charging

The tensile stress-strain curves obtained for the smooth specimens of both wrought and SLM-ed steels under hydrogen charging are given in ***Figure 4. 6*** and ***Figure 4. 7***. In order to compare the hydrogen susceptibility of each steel, the tensile stress-strain curves in air of smooth specimens were added to ***Figure 4. 6*** and ***Figure 4. 7***. A pronounced effect of hydrogen charging can be observed for the two steels that is characterized by a large decrease in elongation to fracture. It can also be seen that the

decrease in strain rate mainly leads to a decrease in fracture stress and elongation for the SLM-ed steel and a decrease in elongation only for the wrought steel. It is thus deduced that the decrease in strain rate enhances the hydrogen embrittlement, in agreement with the literature [35–40]. It is well known that hydrogen not only assists crack propagation but is also involved in its initiation. In order for a crack to initiate under a static stress, a certain hydrogen concentration must be accumulated on a certain distance below the surface. This phenomenon is time dependent [41,42]. Thus, by decreasing the strain rate, the charging time is increased leading to a higher hydrogen concentration for the same stress level. Consequently, the cracking will be initiated prematurely for the lower strain rate. Furthermore, the H-pre+charged specimens had higher reduction in elongation compared to simply H-charged specimens for both wrought and SLM-ed steels. The pre-charging increases the H concentration in the steel leading to premature cracking and enhanced hydrogen embrittlement.

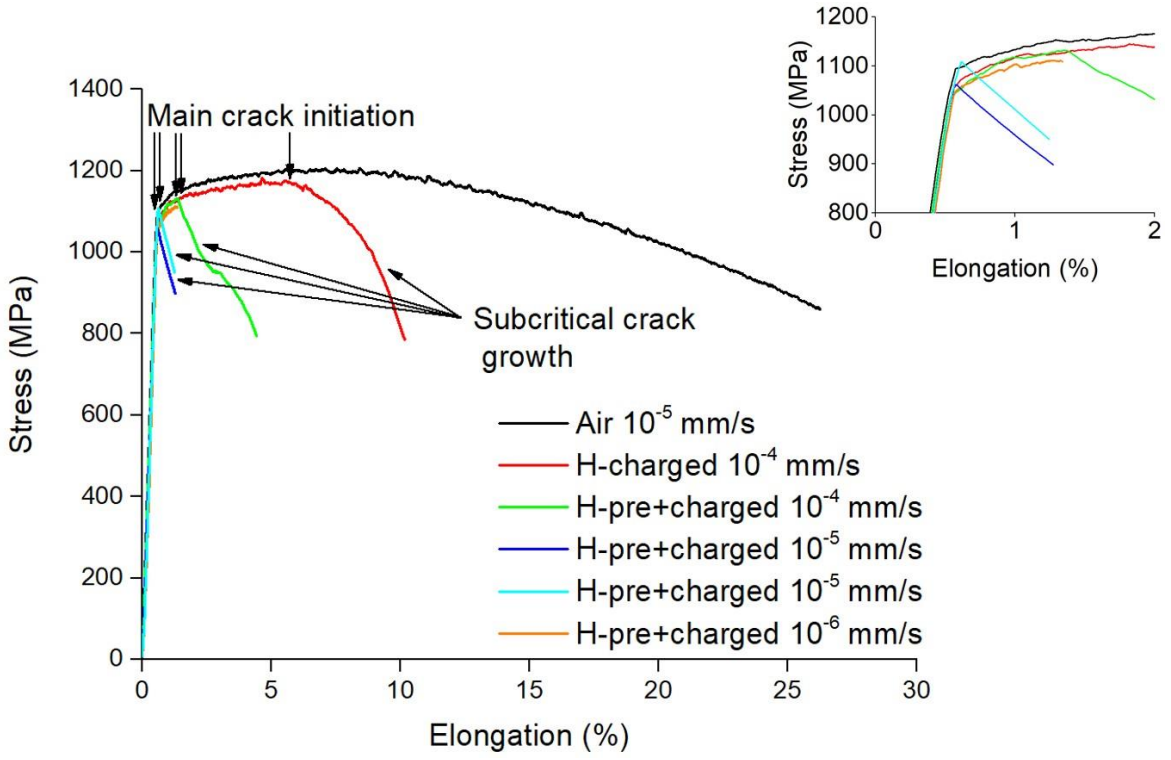

Figure 4. 6: Stress-strain curves of wrought smooth specimens in air and under hydrogen charging showing a reduction in elongation to fracture for the specimens under hydrogen charging.

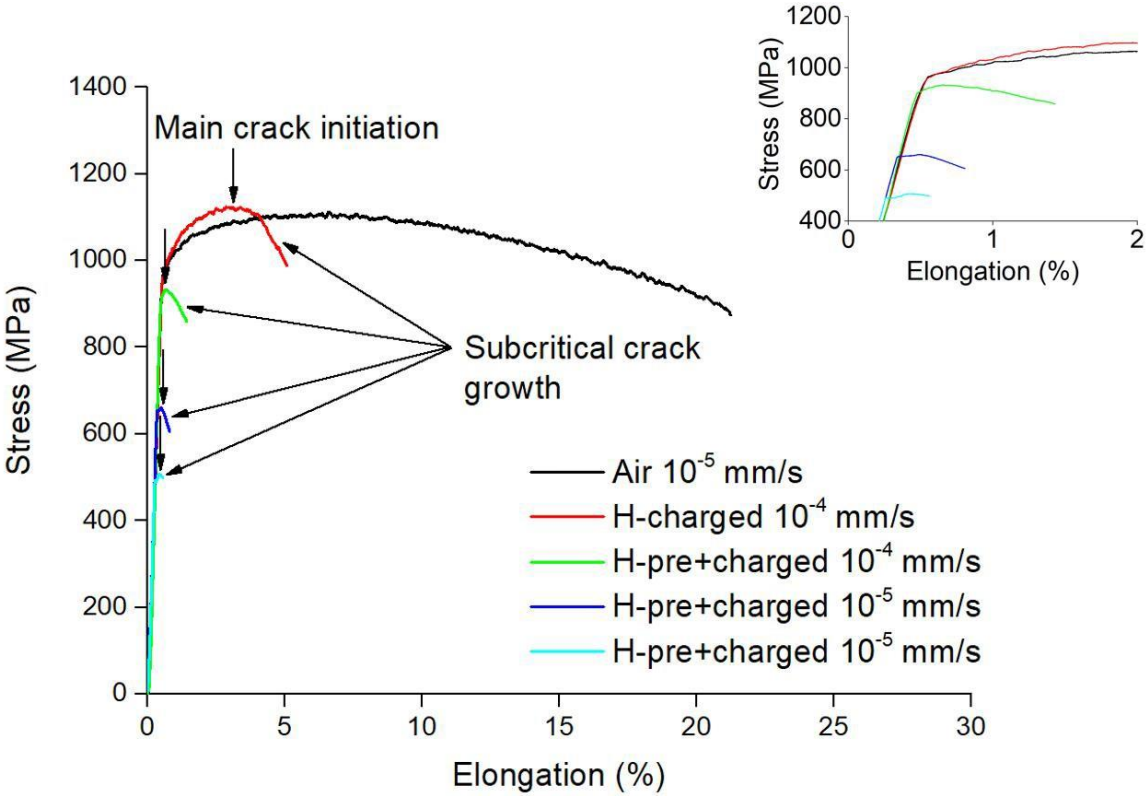

Figure 4. 7: Stress-strain curves of SLM-ed smooth specimens in air and under hydrogen charging showing a reduction in elongation to fracture for the specimens under hydrogen charging.

Figure 4. 8 shows a side view of wrought H-charged specimen tested at 10^{-4} mm/s and SLM-ed H-charged specimen tested at 10^{-4} mm/s. Both specimens show a considerable number of small secondary cracks that initiated and slightly propagated but didn't induce the final fracture. The direction of propagation is perpendicular to the tensile axis. These cracks present evidence of subcritical crack growth regime occurring in the two steels. Thus, the fracture in the two steels can be described by these successive steps: subcritical multi-cracking, then the coalescence of some of the cracks to form the main crack that propagates up to a critical length, which then takes the step until the final fracture by overloading on the remaining ligament. Stress-strain curves under hydrogen charging in **Figure 4. *6*** and **Figure 4. *7*** also show evidence of subcritical crack growth as a decrease in load is observed before the onset of necking. In the following, it will be assumed that the main crack initiation corresponds to the point where the curve deviates from the stress-strain curve in air [43]. What follows the initiation point is a gradual decrease in stress that can be correlated to the main crack propagation. Since the main crack propagates slowly, hydrogen have sufficient time to interact at the crack tip and induce a hydrogen-assisted cracking phenomenon. It should be noted that for the H-pre+charged wrought specimen tested at 10^{-6} mm/s, the gradual decrease in load is not visible. In this

particular case of very low strain rate, the subcritical crack propagation was probably faster than the acquisition time interval selected (3 s). On the other hand, the overload crack propagation occurs at very high speed (almost equal to half of the speed of sound) [44]. This prevents any crack/hydrogen interaction during overload fracture.

Figure 4. *6* shows that for the wrought steel, subcritical cracks initiate always in the plastic domain. In contrast, **Figure 4. *7*** shows that for the SLM-ed steel, initiation occurs earlier in the elastic domain. Thus, it can be concluded that the ferritic SLM-ed steel is more susceptible to hydrogen embrittlement than the martensitic wrought steel. This is due to the difference in microstructures. As mentioned earlier the stress needed to overcome the crack initiation, initial extension and the crossing of its first obstacle is inversely proportional to the grain size, which is still true under hydrogen. Thus, since the ferritic SLM-ed steel has higher grain size, the hydrogen assisted crack initiation and propagation is easier in this steel than in the martensitic wrought steel.

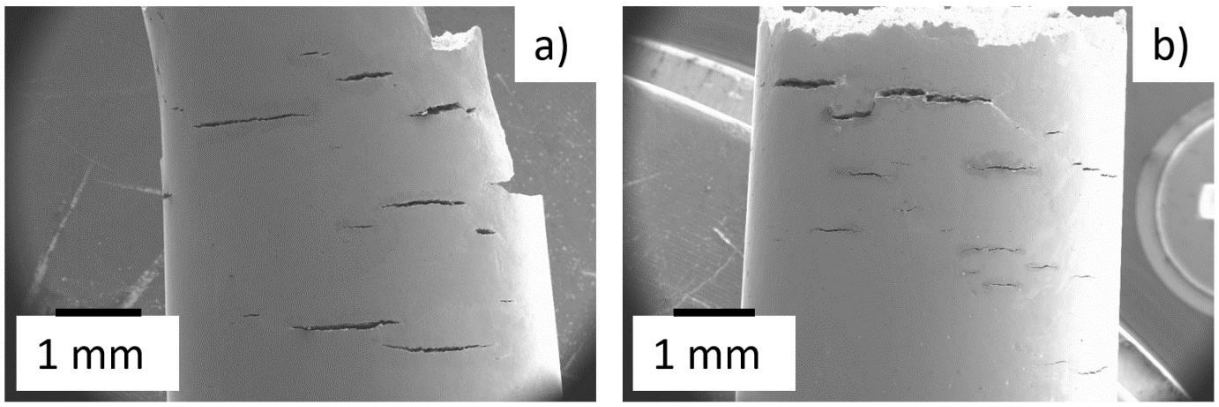

Figure 4. 8: Evidence of subcritical crack growth in (a) wrought charged specimen at 10-4 mm/s and (b) SLM-ed charged specimen at 10-4 mm/s.

The fracture surface of the H-pre+charged wrought specimen at 10^{-4} mm/s strain rate is given in ***Figure 4. 9.a and .c***. It is also representative of the fracture surface of the charged and pre+charged wrought specimens tested at all rates. The overall surface is essentially composed of two different zones: a brittle zone located close to the surface, followed by a ductile zone with dimples located mainly in the center. The brittle zone is mainly intergranular along the prior austenitic grain boundaries [45]. As mentioned earlier, the fracture in this steel is due to the coalescence of some subcritical cracks that formed the main crack. The latter propagated to a critical length, which consequently led to an overload fracture. During subcritical crack propagation, hydrogen assisted cracking occurs. It is thus expected that the main crack propagation region corresponds to a hydrogen affected brittle zone at

the border. Here, this zone has a brittle intergranular fracture mode. The size of this zone is approximately 800-900 µm, which is larger than the hydrogen diffusion distance calculated from permeation in the previous section (220 µm). This supports the assumption of local effects of hydrogen at the crack tip. On the other hand, since the overload fracture occurs at a critical speed, no hydrogen interaction can occur. Thus, the overload fracture region should correspond to a hydrogen unaffected zone. Furthermore, the propagated main crack can be pictured as a severe notch at the surface of the specimen. Thus, at the overload fracture, the specimen can be considered to be notched. As seen in the previous section, the notched wrought specimen tested in air exhibited mainly a ductile fracture mode. Consequently, the overload fracture occurs by ductile mode, and thus corresponds to the ductile zone with dimples located mainly in the center [41,46].

The fracture surface of the H-pre+charged SLM-ed specimen tested at 10^{-4} mm/s strain rate is given in ***Figure 4. 9.b and d***. It is also similar to the fracture surfaces of the charged and pre+charged SLM-ed specimens tested at all strain rates. Unlike the wrought steel, the overall surface shows a brittle bright surface. At higher magnification, the whole surface exhibited a transgranular cleavage mode. Similarly to the wrought steel, the specimen fracture in the SLM-ed steel is due to subcritical multi-cracking, then some of the cracks coalesce and form the main crack that propagates up to critical length and leads to the overload fracture. Thus, the main crack propagation region should correspond to a hydrogen affected brittle zone close to the surface. Here, the brittle zone has a transgranular cleavage morphology. On the other hand, a hydrogen unaffected zone corresponding to the overload fracture should be present. Similarly to the wrought steel, the propagating main crack can be considered as a severe small notch at the surface of the specimen. As shown in the previous section, the notched specimen tested in air exhibited a brittle transgranular cleavage fracture mode. It is thus expected that the overload fracture will occur by transgranular cleavage mode. Since the two zones (hydrogen affected and unaffected zones) have the same fracture mode (transgranular cleavage), their boundary cannot be distinguished on the fracture surface.

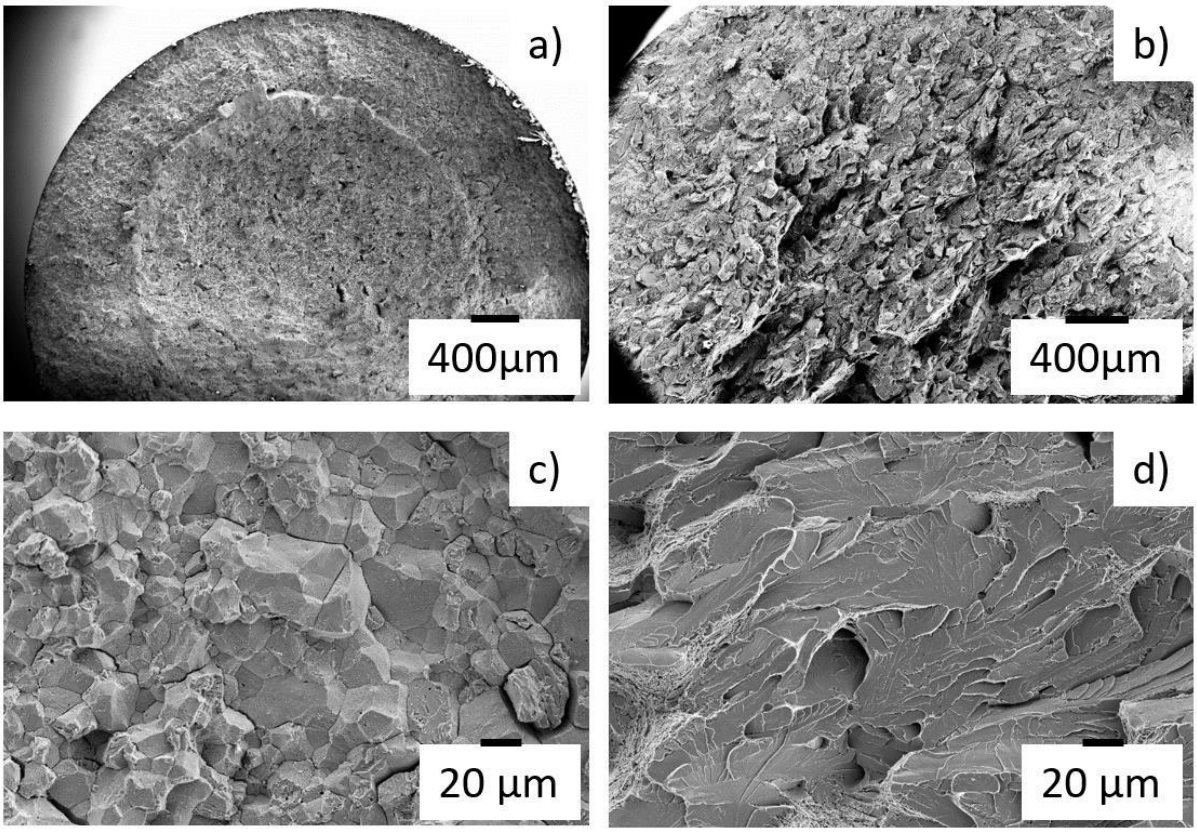

Figure 4. 9: Fracture surfaces after tensile test under hydrogen charging of smooth specimens of (a), (c) wrought steel at 10^{-4} mm/s showing intergranular fracture mode at the borders and (b), (d) SLM-ed steel at 10^{-4} mm/s showing brittle behavior with cleavage on the entire surface.

As mentioned earlier, it is assumed that the main subcritical crack initiates when the stress-strain curves deviate from the curve measured in air. Thus, the time at initiation t_{ini} can be determined. From this time, the severity of hydrogen charging can be estimated as $\sqrt{2D t_{ini}}$ which is the diffusion distance of hydrogen into the material at t_{ini}. It should be noted that this value is proportional to the amount of hydrogen (in at.m^{-2} for example) introduced into the material.

From the stress-strain curves of **Figure 4. *6*** and **Figure 4. *7***, the values of t_{ini}, time at crack initiation, and σ_{ini}, stress at crack initiation were extracted for the two materials at the different charging conditions. ***Figure 4. 10*** shows the stress at crack initiation versus $\sqrt{2Dt_{ini}}$, which represents the severity of hydrogen charging. The two materials show very different behaviors. For the SLM-ed ferritic steel, a decrease of the initiation stress is observed when the H charging conditions become more severe. This suggests that crack initiates through a purely decohesive mechanism in which the brittle crack initiation stress is decreased when the hydrogen concentration beneath the surface is increased. However, for the wrought martensitic steel, the initiation stress is found practically independent of

the H charging severity. This suggests that in contrast to what was observed for the ferritic SLM-ed steel, the stress level and H concentration below the surface are not the only parameters controlling the crack initiation. Instead, it is suggested that plastic deformation is needed here to initiate the crack. This would explain why the initiation stress for the wrought martensitic steel is practically always the same: as soon as plastic deformation is involved, the stress is necessarily in the range 1100-1200 MPa considering the flow behavior of the material (i.e. practically no work-hardening). This has to be related to the crack path observed: the subcritical crack in the wrought material is essentially intergranular. This tends to show that plastic deformation is needed to initiate any intergranular crack. This is in agreement with the work of Nagao *et al.* [46] who demonstrated a hydrogen-enhanced-plasticity mechanism involved in the intergranular fracture of lath martensitic steels. The crack initiation would require a certain hydrogen concentration in the grain boundary. This amount is reached through the dragging of hydrogen by mobile dislocations [47–53] to the grain boundaries. As this mechanism is possible only when dislocations are mobile, it can be active only above the yield strength of the material (or possibly just below it in case of local micro-plasticity), which is consistent with the present observations.

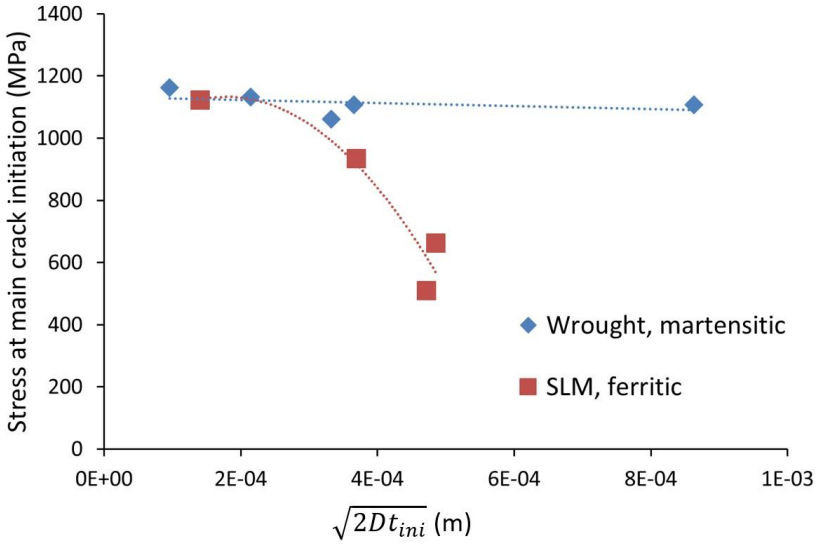

Figure 4. 10: Stress at main crack initiation versus $\sqrt{2Dt_{ini}}$, showing similar stress level for the different hydrogen concentration for the wrought specimen and a decrease in stress with increasing hydrogen concentration for the SLM-ed steel.

4.5 Conclusion

This study focused on the hydrogen embrittlement of 17-4 PH stainless steel fabricated by SLM compared with the wrought steel. A microstructural characterization was first performed on both

wrought and SLM-ed steels. The wrought steel showed a typical martensitic microstructure with lathes. However, the SLM-ed steel exhibited a δ ferritic microstructure with coarse grains. This was due to the high cooling and heating rates experienced during SLM that suppressed the austenite formation and retained the δ ferrite down to room temperature.

The hydrogen embrittlement tests consisted of slow strain rate tensile tests in acidic chloride medium at room temperature under cathodic charging. The degree of hydrogen susceptibility of each steel was assessed by comparing the stress-strain curves of uncharged, charged and pre+charged smooth specimens. In addition, a study of the fracture surfaces was conducted in order to fully understand the hydrogen effect on the fracture mode. The main conclusions that can be drawn are:

1. Wrought and SLM-ed steels were both susceptible to hydrogen embrittlement under slow strain rates. They exhibited a remarkable decrease in elongation to fracture compared with the uncharged steels.
2. The SLM-ed steel was more susceptible to hydrogen embrittlement than the wrought steel. This was due to the difference in grain sizes: the crack initiation and propagation was much easier in the ferritic SLM-ed steel than in the martensitic wrought steel.
3. The fracture in both steels was correlated the coalescence of subcritical cracks to form the main crack that propagated to a critical length and consequently led to an overload fracture.
4. The fracture surface of the wrought steel showed two zones: an intergranular brittle fracture zone close to the surface and a ductile zone in the center. The intergranular fracture zone corresponds to the subcritical crack propagation. The ductile zone is correlated to the overload fracture, which is consistent with the fracture mode of wrought notched specimen tested in air.
5. On the other hand, in the SLM-ed steel, both the subcritical crack growth and the final overload fracture were obtained by transgranular cleavage mode. This overload fracture mode is consistent with the fracture mode of SLM-ed notched specimen tested in air.
6. For the SLM-ed steel, stress and H concentration are the only factors needed to initiate the crack. The crack initiation occurs through a purely decohesive mechanism in which the brittle crack initiation stress is decreased when the hydrogen concentration beneath the surface is increased.
7. For the wrought steel, in addition to the stress and H concentration, plastic deformation is also needed to initiate the intergranular crack. It is suggested that the crack initiation requires a certain hydrogen concentration in the grain boundary, which is achieved through the dragging of hydrogen by mobile dislocations to the grain boundaries.

4.6 References

[1] J.C.M. Farrar, in: The Alloy Tree: A Guide to Low-Alloy Steels, Stainless Steels, and Nickel-Base Alloys, CRC Press ; Woodhead Pub, Boca Raton : Cambridge, Eng, 2004: pp. 44–45.

[2] L.E. Murr, E. Martinez, J. Hernandez, S. Collins, K.N. Amato, S.M. Gaytan, P.W. Shindo, On the characterization of stainless steel 316L parts produced by selective laser melting, Journal of Materials Research and Technology. 1 (2012) 167–177. https://doi.org/10.1016/S2238-7854(12)70029-7.

[3] M. Murayama, K. Hono, Y. Katayama, Microstructural evolution in a 17-4 PH stainless steel after aging at 400 C, Metallurgical and Materials Transactions A. 30 (1999) 345–353.

[4] C.N. Hsiao, C.S. Chiou, J.R. Yang, Aging reactions in a 17-4 PH stainless steel, Materials Chemistry and Physics. 74 (2002) 134–142. https://doi.org/10.1016/S0254-0584(01)00460-6.

[5] U.K. Viswanathan, S. Banerjee, R. Krishnan, Effects of aging on the microstructure of 17-4 PH stainless steel, Materials Science and Engineering: A. 104 (1988) 181–189. https://doi.org/10.1016/0025-5416(88)90420-X.

[6] W.D. Yoo, J.H. Lee, K.T. Youn, Y.M. Rhyim, Study on the Microstructure and Mechanical Properties of 17-4 PH Stainless Steel Depending on Heat Treatment and Aging Time, Solid State Phenomena. 118 (2006) 15–20. https://doi.org/10.4028/www.scientific.net/SSP.118.15.

[7] W.C. Chiang, C.C. Pu, B.L. Yu, J.K. Wu, Hydrogen susceptibility of 17-4 PH stainless steel, Materials Letters. 57 (2003) 2485–2488. https://doi.org/10.1016/S0167-577X(02)01298-3.

[8] Y. Hayashi, T. Ito, Y. Nishimura, K. Takai, The states of hydrogen and hydrogen embrittlement susceptibility of precipitation hardened SUS630 stainless steel, IOP Conf. Ser.: Mater. Sci. Eng. 461 (2018) 012023. https://doi.org/10.1088/1757-899X/461/1/012023.

[9] S. Shen, X. Li, P. Zhang, Y. Nan, G. Yang, X. Song, Effect of solution-treated temperature on hydrogen embrittlement of 17-4 PH stainless steel, Materials Science and Engineering: A. 703 (2017) 413–421. https://doi.org/10.1016/j.msea.2017.06.078.

[10] C.T. Murray, Hydrogen Embrittlement of 15-5 PH Stainless Steels, MTA. 12 (1981) 2138–2141. https://doi.org/10.1007/BF02644189.

[11] P.K. Gokuldoss, S. Kolla, J. Eckert, Additive Manufacturing Processes: Selective Laser Melting, Electron Beam Melting and Binder Jetting—Selection Guidelines, Materials. 10 (2017) 672. https://doi.org/10.3390/ma10060672.

[12] T.D. Ngo, A. Kashani, G. Imbalzano, K.T.Q. Nguyen, D. Hui, Additive manufacturing (3D printing): A review of materials, methods, applications and challenges, Composites Part B: Engineering. 143 (2018) 172–196. https://doi.org/10.1016/j.compositesb.2018.02.012.

[13] C.Y. Yap, C.K. Chua, Z.L. Dong, Z.H. Liu, D.Q. Zhang, L.E. Loh, S.L. Sing, Review of selective laser melting: Materials and applications, Applied Physics Reviews. 2 (2015) 041101. https://doi.org/10.1063/1.4935926.

[14] M. Rombouts, J.-P. Kruth, L. Froyen, P. Mercelis, Fundamentals of selective laser melting of alloyed steel powders, CIRP Annals-Manufacturing Technology. 55 (2006) 187–192. https://doi.org/10.1016/S0007-8506(07)60395-3.

[15] J.P. Kruth, L. Froyen, J. Van Vaerenbergh, P. Mercelis, M. Rombouts, B. Lauwers, Selective laser melting of iron-based powder, Journal of Materials Processing Technology. 149 (2004) 616–622. https://doi.org/10.1016/j.jmatprotec.2003.11.051.

[16] M. Alnajjar, F. Christien, K. Wolski, C. Bosch, Evidence of austenite by-passing in a stainless steel obtained from laser melting additive manufacturing, Additive Manufacturing. (2018). https://doi.org/10.1016/j.addma.2018.11.004.

[17] T. Niendorf, S. Leuders, A. Riemer, H.A. Richard, T. Tröster, D. Schwarze, Highly Anisotropic Steel Processed by Selective Laser Melting, Metallurgical and Materials Transactions B. 44 (2013) 794–796. https://doi.org/10.1007/s11663-013-9875-z.

[18] H.K. Rafi, D. Pal, N. Patil, T.L. Starr, B.E. Stucker, Microstructure and Mechanical Behavior of 17-4 Precipitation Hardenable Steel Processed by Selective Laser Melting, Journal of Materials

Engineering and Performance. 23 (2014) 4421–4428. https://doi.org/10.1007/s11665-014-1226-y.
[19] F. Hengsbach, P. Koppa, K. Duschik, M.J. Holzweissig, M. Burns, J. Nellesen, W. Tillmann, T. Tröster, K.-P. Hoyer, M. Schaper, Duplex stainless steel fabricated by selective laser melting - Microstructural and mechanical properties, Materials & Design. 133 (2017) 136–142. https://doi.org/10.1016/j.matdes.2017.07.046.
[20] K. Saeidi, L. Kevetkova, F. Lofaj, Z. Shen, Novel ferritic stainless steel formed by laser melting from duplex stainless steel powder with advanced mechanical properties and high ductility, Materials Science and Engineering: A. 665 (2016) 59–65. https://doi.org/10.1016/j.msea.2016.04.027.
[21] M.A.V. Devanathan, Z. Stachurski, The adsorption and diffusion of electrolytic hydrogen in palladium, Proc. R. Soc. Lond. A. 270 (1962) 90–102. https://doi.org/10.1098/rspa.1962.0205.
[22] S. Vunnam, Effect of powder chemical composition on the as-built microstructure of 17-4 PH stainless steel processed by selective laser melting, Additive Manufacturing. (2019) 12.
[23] O. Andreau, I. Koutiri, P. Peyre, J.-D. Penot, N. Saintier, E. Pessard, T. De Terris, C. Dupuy, T. Baudin, Texture control of 316L parts by modulation of the melt pool morphology in selective laser melting, Journal of Materials Processing Technology. 264 (2019) 21–31. https://doi.org/10.1016/j.jmatprotec.2018.08.049.
[24] G.E. Dieter, in: Mechanical Metallurgy, McGraw-Hill Education, 1961: pp. 190–220.
[25] C. Zener, The micro-mechanism of fracture, in: Fracturing of Metals, American Society for Metals, Metals Park, Ohio, 1948.
[26] A.N. Stroh, The Formation of Cracks as a Result of Plastic Flow, Proceedings of the Royal Society of London. Series A, Mathematical and Physical Sciences. 223 (1954) 404–414.
[27] A.N. Stroh, CXI. Brittle fracture and yielding, The London, Edinburgh, and Dublin Philosophical Magazine and Journal of Science. 46 (1955) 968–972. https://doi.org/10.1080/14786440908520617.
[28] A. Oudriss, J. Creus, J. Bouhattate, E. Conforto, C. Berziou, C. Savall, X. Feaugas, Grain size and grain-boundary effects on diffusion and trapping of hydrogen in pure nickel, Acta Materialia. 60 (2012) 6814–6828. https://doi.org/10.1016/j.actamat.2012.09.004.
[29] A.J. Haq, K. Muzaka, D.P. Dunne, A. Calka, E.V. Pereloma, Effect of microstructure and composition on hydrogen permeation in X70 pipeline steels, International Journal of Hydrogen Energy. 38 (2013) 2544–2556. https://doi.org/10.1016/j.ijhydene.2012.11.127.
[30] Y. Cao, H. Li, J.A. Szpunar, W.T. Shmayda, Anisotropic Hydrogen Permeation in Nano/Poly Crystalline-Nickel Membranes, MRS Proc. 752 (2002) AA12.4. https://doi.org/10.1557/PROC-752-AA12.4.
[31] S.L.I. Chan, Hydrogen trapping ability of steels with different microstructures, Journal of the Chinese Institute of Engineers. 22 (1999) 43–53. https://doi.org/10.1080/02533839.1999.9670440.
[32] C.H. Tseng, W.V. Wei, J.K. Wu, Electrochemical methods for studying hydrogen diffusivity, permeability, and solubility in AISI 420 and AISI 430 stainless steels, 5 (1989) 4.
[33] J. Svoboda, G. Mori, A. Prethaler, F.D. Fischer, Determination of trapping parameters and the chemical diffusion coefficient from hydrogen permeation experiments, Corrosion Science. 82 (2014) 93–100. https://doi.org/10.1016/j.corsci.2014.01.002.
[34] T. Si, Y. Liu, Q. Zhang, D. Liu, Y. Li, Effect of Microstructure on Hydrogen Permeation in EA4T and 30CrNiMoV12 Railway Axle Steels, Metals. 9 (2019) 164. https://doi.org/10.3390/met9020164.
[35] B. Bal, M. Koyama, G. Gerstein, H.J. Maier, K. Tsuzaki, Effect of strain rate on hydrogen embrittlement susceptibility of twinning-induced plasticity steel pre-charged with high-pressure hydrogen gas, International Journal of Hydrogen Energy. 41 (2016) 15362–15372. https://doi.org/10.1016/j.ijhydene.2016.06.259.

[36] T. Hojo, R. Kikuchi, H. Waki, F. Nishimura, Y. Ukai, E. Akiyama, Effect of Strain Rate on the Hydrogen Embrittlement Property of Ultra High-strength Low Alloy TRIP-aided Steel, ISIJ International. 58 (2018) 751–759. https://doi.org/10.2355/isijinternational.ISIJINT-2017-576.
[37] Y. Momotani, A. Shibata, D. Terada, N. Tsuji, Effect of strain rate on hydrogen embrittlement in low-carbon martensitic steel, International Journal of Hydrogen Energy. 42 (2017) 3371–3379. https://doi.org/10.1016/j.ijhydene.2016.09.188.
[38] Y. Momotani, A. Shibata, D. Terada, N. Tsuji, Hydrogen Embrittlement Behavior at Different Strain Rates in Low-carbon Martensitic Steel, Materials Today: Proceedings. 2 (2015) S735–S738. https://doi.org/10.1016/j.matpr.2015.07.387.
[39] H.K. Birnbaum, Hydrogen effects on deformation — Relation between dislocation behavior and the macroscopic stress-strain behavior, Scripta Metallurgica et Materialia. 31 (1994) 149–153. https://doi.org/10.1016/0956-716X(94)90166-X.
[40] M. Hashimoto, R.M. Latanision, The role of dislocations during transport of hydrogen in hydrogen embrittlement of iron, MTA. 19 (1988) 2799–2803. https://doi.org/10.1007/BF02645814.
[41] H.H. Johnson, A.R. Troiano, Crack Initiation in Hydrogenated Steel, Nature. 179 (1957) 777.
[42] N.J. Petch, P. Stables, Delayed Fracture of Metals under Static Load, Nature. 169 (1952) 842–843.
[43] M. Koyama, E. Akiyama, K. Tsuzaki, D. Raabe, Hydrogen-assisted failure in a twinning-induced plasticity steel studied under in situ hydrogen charging by electron channeling contrast imaging, Acta Materialia. 61 (2013) 4607–4618. https://doi.org/10.1016/j.actamat.2013.04.030.
[44] G.A. Pantazopoulos, A Short Review on Fracture Mechanisms of Mechanical Components Operated under Industrial Process Conditions: Fractographic Analysis and Selected Prevention Strategies, (2019) 20.
[45] A. Nagao, M. Dadfarnia, B.P. Somerday, P. Sofronis, R.O. Ritchie, Hydrogen-enhanced-plasticity mediated decohesion for hydrogen-induced intergranular and "quasi-cleavage" fracture of lath martensitic steels, Journal of the Mechanics and Physics of Solids. 112 (2018) 403–430. https://doi.org/10.1016/j.jmps.2017.12.016.
[46] A.R. Troiano, The Role of Hydrogen and Other Interstitials in the Mechanical Behavior of Metals: (1959 Edward De Mille Campbell Memorial Lecture), Metallogr. Microstruct. Anal. 5 (2016) 557–569. https://doi.org/10.1007/s13632-016-0319-4.
[47] J. Tien, A.W. Thompson, I.M. Bernstein, R.J. Richards, Hydrogen transport by dislocations, MTA. 7 (1976) 821–829. https://doi.org/10.1007/BF02644079.
[48] J.A. Donovan, Accelerated evolution of hydrogen from metals during plastic deformation, Metallurgical Transactions A. (1976) 1677–1683. https://doi.org/10.1007/BF02817885.
[49] C. Hwang, I.M. Bernstein, Dislocation transport of hydrogen in iron single crystals, Acta Metallurgica. 34 (1986) 1001–1010. https://doi.org/10.1016/0001-6160(86)90209-9.
[50] J. Chêne, A.M. Brass, Hydrogen transport by mobile dislocations in nickel base superalloy single crystals, Scripta Materialia. 40 (1999) 537–542. https://doi.org/10.1016/S1359-6462(98)00451-5.
[51] G.S. Frankel, R.M. Latanision, Hydrogen transport during deformation in nickel: Part II. Single crystal nickel, Metallurgical Transactions A. 17A (1986) 869–875. https://doi.org/10.1007/BF02643863.
[52] H. Shoda, H. Suzuki, K. Takai, Y. Hagihara, Hydrogen Desorption Behavior of Pure Iron and Inconel 625 during Elastic and Plastic Deformation, ISIJ Int. 50 (2010) 115–123. https://doi.org/10.2355/isijinternational.50.115.
[53] D. Guedes, A. Oudriss, S. Cohendoz, J. Creus, J. Bouhattate, X. Feaugas, F. Thebault, D. Koschel, The Influence of Hydrogen Flux on Crack Initiation in Martensitic Steels, Procedia Materials Science. 3 (2014) 2024–2029. https://doi.org/10.1016/j.mspro.2014.06.326.

General conclusions and perspectives

The present thesis focuses on the corrosion properties of 17-4 PH stainless steel fabricated by Selective Laser Melting (SLM). Microstructural characterization on wrought and as-built SLM-ed steels was done using optical microscopy, X-ray diffraction (XRD) and scanning electron microscopy equipped with electron backscatter diffraction (EBSD) and energy-dispersive X-ray spectroscopy (EDS). In addition, dilatometry was used to study the phase transformation in both steels. The optical micrographs showed a typical martensitic microstructure with lathes for the wrought steel, while it showed no evidence of lathes of martensite for the SLM-ed steel. XRD showed that SLM-ed steel had a BCC structure. EBSD maps confirmed the optical micrographs observations and showed that the microstructure of the as-built SLM-ed steel is completely ferritic. This was interpreted as a result of the high thermal rates experienced during SLM (105-106 K/s) that didn't allow the austenite phase sufficient time to form. Thus, the solidified delta ferrite doesn't encounter any metallurgical transformation during the numerous thermal cycles during SLM. This resulted in ferritic microstructure of the SLM-ed 17-4 PH steel at the end of fabrication. Other specimens of as-built 17-4 PH steel fabricated in different SLM machines were also studied. In each case a fully ferritic microstructure was observed, which suggests a certain generality of this result. After solution treatment, the microstructure of the SLM-ed steel recovers its martensitic microstructure with lathes. The dilatometry measurements confirmed the transformation of delta ferrite to austenite during heating and the austenite to martensite transformation during cooling. The neutron diffraction measurements also showed the austenite to δ ferrite transformation at high temperatures, which proved that the SLM-ed steel is mainly ferritic at melting temperature.

The corrosion behavior of the 17-4 PH SLM-ed steel was then investigated. The material used in this study was wrought steel (martensitic), as-build (ferritic) and re-austenitized SLM-ed steels (martensitic). The electrochemical characterization consisted of anodic scans in chloride acidic solution. Both SLM-ed (as-built and re-austenitized) had similar general corrosion resistance regardless of their different microstructures. Their similar chemical composition controlled the chemical composition of the passive film and thus its stability. The re-austenitized SLM-ed steel had a remarkably superior general corrosion resistance than the wrought steel. This was associated with the high sulfur content, more specifically the MnS inclusion content in the wrought steel. The dissolution of MnS inclusions led to a deposition of a sulfur rich layer in the adjacent regions that promoted the destabilization of the passive film and thus deteriorated the general corrosion resistance. The XPS measurements confirmed the formation of sulfur species on the surface of the wrought steel.

The hydrogen embrittlement of SLM-ed 17-4 PH was investigated. The materials studied were SLM-ed (ferritic) and wrought (martensitic) steels. They were both subjected to an overaging treatment at

580°C for 4 hours, which led to similar strength of the both steels. The hydrogen embrittlement tests consisted of slow strain rate tensile tests in acidic chloride medium at room temperature under in-situ cathodic charging. The degree of hydrogen susceptibility of each steel was assessed by comparing the stress-strain curves of uncharged, charged and precharged+charged smooth specimens. In addition, a study of the fracture surfaces was conducted in order to fully understand the hydrogen effect on the fracture mode. It was found that the SLM-ed steel was more susceptible to hydrogen embrittlement than the wrought steel. This was due to the difference in grain sizes: the crack initiation and propagation was much easier in the ferritic SLM-ed steel than in the martensitic wrought steel. The fracture in both steels was correlated with the coalescence of subcritical cracks to form the main crack that propagated to a critical length and consequently led to an overload fracture. The fracture surface of the wrought steel showed two zones: an intergranular brittle fracture zone close to the surface and a ductile zone in the center. The intergranular fracture zone corresponds to the subcritical crack propagation. On the other hand, in the SLM-ed steel, both the subcritical crack growth and the final overload fracture were obtained by transgranular cleavage. For the SLM-ed steel, stress and H concentration are the only factors needed to initiate the crack. The crack initiation occurs through a purely decohesive mechanism. For the wrought steel, in addition to the stress and H concentration, plastic deformation is also needed to initiate the intergranular crack. The crack initiation require a certain hydrogen concentration in the grain boundary, which is achieved through the dragging of hydrogen by mobile dislocations to the grain boundaries.

One of the main results of the microstructural study conducted in this work is that the as-built microstructure of the SLM-ed 17-4 PH steel is essentially δ ferritic. A possible perspective of this work would be to adjust the chemical composition of the steel and/or the process parameters to obtain the desired martensitic microstructure in the as-built state. The neutron diffraction study has shown that the temperature range of δ ferrite at high temperature is strongly dependent on the chemical composition. This was observed in appendix 2, where a slight change in nickel content induced a change in primary solidification phases. Increasing the nickel content could allow a solidification in austenite, rather than in δ ferrite, which would give a martensitic microstructure once cooled to room temperature. However the nickel content should not be too high, so as not to retain too much austenite in the final microstructure.

On the other hand, the process parameters can affect the cooling and heating rates. A decrease of those rates might facilitate the transformation of δ ferrite to austenite in the solid state and thus lead

to a martensitic microstructure in the final state. In addition, the effect of the atmosphere used in powder atomization and SLM fabrication on the stabilization of a certain phases can also be investigated. For example, the nitrogen environment can stabilize the austenite phase and play the same role as nickel as mentioned above.

For more understanding of the SLM-ed microstructures, further studies on the phase transformations in this steel should be conducted, specifically, the effect of heating and cooling rates on the onset and finish temperatures of phase transformations at very high temperatures, i.e. close to the melting temperature. In order to do so, dilatometry or diffraction measurements can be done at various heating and cooling rates. The variation of phase transformation (onset and finish temperatures) with thermal rates can be assessed. Consequently, the possibility of phase transformations at the thermal rates experienced by SLM can be determined.

The electrochemical corrosion study has shown a critical effect of the manganese sulfide inclusions on the general corrosion of the material: the as-built SLM-ed material, free of any MnS inclusions, has a much better corrosion resistance. One of the reasons for the absence of MnS inclusions in the as-built SLM material is that the MnS have dissolved at high temperature and the very high cooling and heating rates do not allow their reformation in the solid state. This suggests that laser melting could be used as a surface treatment process of steels to suppress the MnS inclusions and increase the corrosion resistance. One perspective of this work would be to process the surface of "high" sulfur steels using laser melting to see if it is possible to completely suppress the MnS inclusions.

The hydrogen embrittlement study has shown that the SLM-ed steel was very sensitive. This was essentially due to its unique δ ferritic microstructure. It would be interesting to investigate the HE of this SLM-ed steel after solution heat treatment that will allow recovering the martensitic microstructure. Some preliminary work has actually already been done in this PhD thesis, but was not included in this manuscript. It showed a difference in behavior between as-built and re-austenitized SLM-ed 17-4 PH steels. The HE resistance of re-austenitized martensitic SLM-ed steel was improved compared to the as-built ferritic steel. In other words, the re-austenitized SLM-ed material behaves very closely to the conventional wrought material. This might be due to the recovering of the martensitic microstructure. In addition, the fracture surfaces showed a change from transgranular mode for the as-built SLM-ed steel to intergranular mode for the re-austenitized SLM-ed steel. This is in agreement with the literature review that concluded that the one of the main characteristics of the HE in martensitic steels is the occurrence of intergranular fracture. This work on the re-austenitized

SLM-ed steel could be pursued, including among other topics a focus on the role of porosity on HE of those material.

From a more fundamental point of view, the hydrogen embrittlement study has suggested that the intergranular fracture observed in the wrought material results from hydrogen dragging by moving dislocations from the bulk to the grain boundaries. Few experimental studies in the literature have focused on the transport of hydrogen by moving dislocations. We think that this topic would deserve more systematic experimental work in the future, including materials of industrial interest, to assess the effect of strain rate and preexisting dislocation density on that mechanism. The studies existing in the literature focused on the dislocation dragging of hydrogen to the surface. One step further would be to demonstrate the same mechanisms toward the grain boundaries, which is much more challenging. The recently developed Scanning Kelvin Probe Force Microscopy method for the local detection of hydrogen might be of interest to investigate such phenomena.

Acknowledgments

The staff of the Pressure and Furnace Section at the ISIS facility, namely Chris Goodway, Paul McIntyre and Adam Sears, are kindly acknowledged for their work in preparing and setting-up the equipment for the neutron diffraction tests. Tuomo Nyyssönen at Tampere University of Technology is acknowledged for supplying the code for the austenite grain reconstruction. The authors would like to acknowledge financial support from Institut CARNOT M.I.N.E.S (project #60678) and from LABEX MANUTECH-SISE (ANR-10-LABX-0075) of Université de Lyon, within the program "Investissements d'Avenir" (ANR-11-IDEX-0007) operated by the French National Research Agency (ANR).

Appendixes

Appendix 1: List of the materials used in this thesis

In this thesis, different SLM-ed 17-4 PH steels (fabricated in different SLM machines with different process parameters and powders) were studied, while only one wrought steel was studied. ***Table.1*** presents the numbering of all the materials studied in this thesis. ***Table.2*** shows the materials studied in each chapter.

Table 1: List of all the materials used in this thesis.

Material number	Material type	SLM machine
1	Wrought 17-4 PH	-
2	SLM-ed 17-4 PH	SLM solution 280
3	SLM-ed 17-4 PH	SLM solution 280 HL
4	SLM-ed 17-4 PH	Concept Laser M2
5	SLM-ed 17-4 PH	EOS M270

Table 2: List of the materials used in each chapter.

Chapter number	Material number
2	1, 2, 3, 4
3	1, 5
4	1, 5
Appendix 2 (neutron diffraction)	1, 5

Appendix 2: Neutron diffraction study of phase transformations in steel 17-4PH

A neutron diffraction study was conducted during a four day experiment in November 2018 at Diamond synchrotron, ISIS Facility, Rutherford Appleton Laboratory, Chilton, UK. The experiment was performed on the HRPD (High Resolution Powder Diffraction) instrument in collaboration with Dr Dominic Fortes and Dr Mark Telling. The objective of this study was to determine the temperature stability range of the δ ferrite phase, if any, and to correlate it with the chemical composition of the materials available for this study. This experiment was undertaken because no precise phase stability measurements are available in the literature for the 17-4PH steel at very high temperature (i.e. close to the melting temperature). Preliminary thermodynamics calculations conducted using Thermo-Calc indicated the possible existence of δ ferrite above 1300°C but experimental validation was needed. Neutron diffraction was chosen, rather than the conventional X-ray diffraction method available in the laboratory, to obtain a genuinely bulk analysis of the material.

Cylindrical specimens 50 mm in length, 5 mm in diameter were cut from each material. The neutron diffraction measurement was conducted while in-situ heating the specimen under high vacuum to avoid any surface oxidation. For accurate temperature control, a thermocouple was inserted directly into a hole drilled into the sample. Typical temperature gradients expected along the sample's 50 mm vertical axis during measurement had been ascertained prior to the neutron experiment using offline test apparatus. Above 1300°C, the temperature was found to be homogeneous within 15 to 20°C along the axis.

Three materials were studied: wrought, as-built SLM-ed and re-austenitized SLM-ed steels. The composition of the materials are recalled in ***Table.1***. The three materials were heated to 1340°C (near melting temperature ~1370°C) at a rate of 5 K/min. The acquisition time was 1 min per pattern. From the neutron diffraction data, it was directly possible to retrieve the neutron diffraction pattern (intensity as a function of the interplanar spacing d). The range of interplanar d spacings probed during a measurement was ~0.65 to 2.65 Å allowing the detection of the main diffraction peaks of the BCC and FCC phases. A complete multiphase Rietveld refinement was conducted to extract the BCC and FCC phase mass fractions. Considering the large number of diffraction patterns obtained, this refinement procedure was not possible for all of them. Instead, only specific patterns were chosen for refinement (about 10 patterns for each experiment). For the rest of the patterns, a more simple procedure was used: the phase mass fractions were estimated using Eq. 1 and 2.

$$\%\ = \frac{}{} \times \qquad \text{Eq.1}$$

$$+$$

$$\% = - \% \qquad \text{Eq.2}$$

where $A_{(110)}$ and $A_{(111)}$ are the peak intensities (peak areas) of the BCC (110) and the FCC (111) lines respectively, *a* and *b* are constants that were adjusted so as to agree with the complete Rietveld refinement when available.

Table 1: Chemical composition (wt. %) of wrought and SLM-ed 17-4 PH stainless steels used for the neutron diffraction study.

17-4 PH		C	Ni	Si	P	Mn	Cr	Cu	S	N	O	Nb F	e
Wrought	Provider Data sheet	0.031	4.82	0.31	0.016	0.81	15.61	3.12	0.02	-	-	0.21	Bal.
	Other analyses	0.026	4.95	-	-	-	16.18	3.09	0.021	0.033	0.007	-	Bal.
SLM-ed		0.03	4.16	-	0.008	-	16.11	3.73	0.003	0.033	0.046	0.3	Bal.

Figure.1 shows the mass fraction variations of the BCC phase with temperature during heating to 1340°C for wrought steel, as-built SLM-ed steel and re-austenitized SLM-ed steel. ***Table.2*** summarizes the BCC (martensite or ferrite) and FCC (austenite) phase fractions at room temperature for the three materials. According to the microstructural characterization done at room temperature using EBSD, the wrought steel is martensitic, the as-built SLM-ed steel is ferritic and the re-austenitized SLM-ed steel is martensitic. ***Figure.1*** shows similar tendencies for the two SLM-ed materials (as-built and re-austenitized). The stability range of austenite is roughly between 1050°C and 1200°C. The fraction of δ ferrite at the 1340°C is about 75% and extrapolation to the melting temperature (1370°C) gives a fraction of approximately 90%. It is then confirmed that this material is mainly δ ferritic at the melting temperature. In addition the similarity shown in ***Figure .1*** for the two SLM-ed materials suggests that the initial microstructure (martensite or δ ferrite) has little effect on the phase transformations upon

heating. Martensite and δ ferrite show the same stability over upon heating, which from thermodynamics is expected.

The wrought material however shows a different behavior from the SLM-ed ones. The austenite stability range is larger (~970 - 1300°C) and the fraction of δ ferrite is much lower: 20% at 1340°C, about 40% after extrapolation at the melting temperature (1370°C). Considering the respective compositions of the two materials (***Table.1***), this difference could be due to nickel which is a strong austenite stabilizer and whose content is higher in the wrought material.

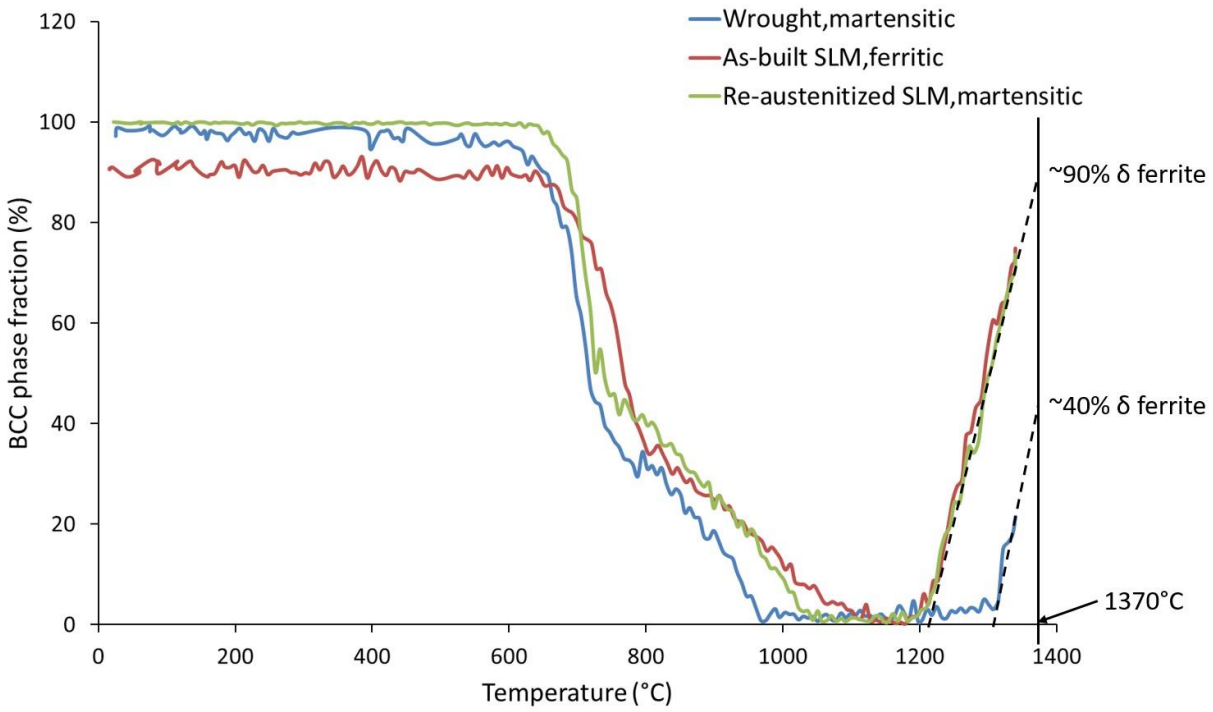

Figure 1: BCC phase fraction in 17-4PH steel obtained using neutron diffraction as a function of temperature during heating to 1340°C at 5K/s.

Table 2: BCC and FCC phase fractions in 17-4PH steel obtained using neutron diffraction at room temperature for the wrought, as-built and re-austenitized SLM-ed steels.

	Wrought	As-built SLM	Re-austenitized SLM
BCC (%)	98-99 (martensite)	90-91 (ferrite)	99-100 (martensite)
FCC (%)	1-2	9-10	<1

Appendix 3: EBSD analysis of a 17-4 PH gas-atomized powder

In this appendix, we present an example of microstructural analysis conducted on 17-4 PH steel powder gas-atomized under nitrogen environment. It should be noted that these powders are not among those used to fabricate the SLM specimens studied in the different chapters of this PhD work.

The atomization process is illustrated in ***Figure.1***: molten metal is poured into the atomization chamber and high pressure and high velocity gas jet comes in contact with the liquid melt, which undergoes fragmentation into droplets. The droplets subsequently spheroidize, cool and freeze into metal powder particles ranging from 1 µm to 1 mm in diameter [1,2].

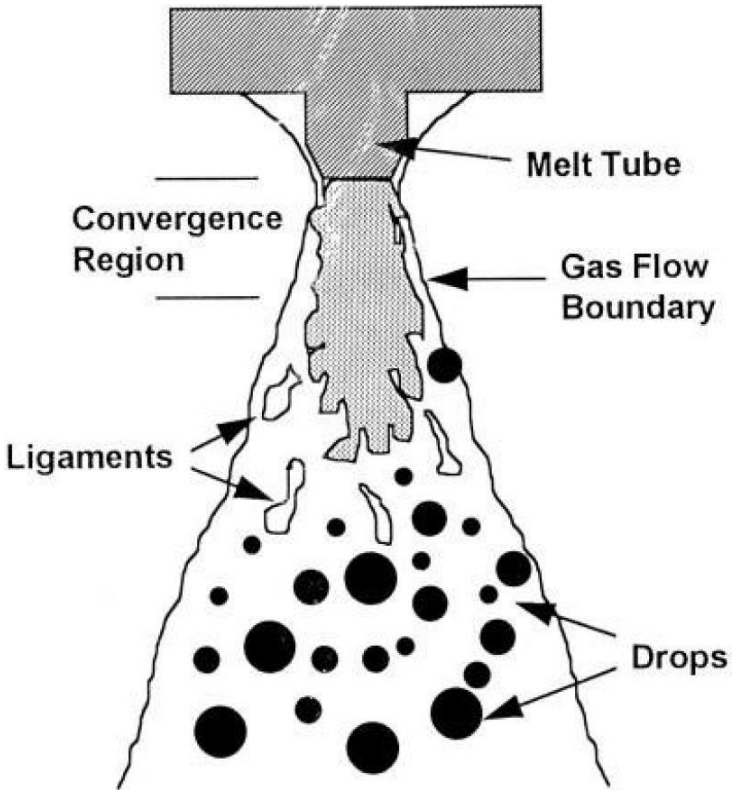

Figure 1: Schematic illustration of gas-atomization [3].

The initial cooling rate experienced during powder atomization process is inversely proportional to the diameter of the droplet according to the following equation:

$$\dot{T} = \frac{6h(T_1 - T_{\square})}{\rho_1 \square_{p,1} \square_1}$$

where $\dot{T}$ is the cooling rate, T_1 the droplet temperature, $T_{\square}$ the gas temperature, ρ_1 the density of the melt droplet, $\square_{p,1}$ the heat capacity of the melt, $\square_1$ the diameter of the droplet and h the convective

heat transfer coefficient [1,4]. Here, the 17-4 PH powder was gas-atomized under nitrogen environment. The corresponding values of the variables are given in [1]. ***Figure.2*** shows the calculated cooling rate as a function of powder size for gas-atomized 17-4 PH stainless steel particles under nitrogen environment [1]. For example, the cooling rate for a droplet of 10 µm in diameter is 1.46 10^7 K/s, while that for a droplet of 90 µm is 3.10 10^5 K/s. This shows that the cooling rates experienced by the metal during gas-atomization are in the same range as those of SLM, even possibly slightly higher.

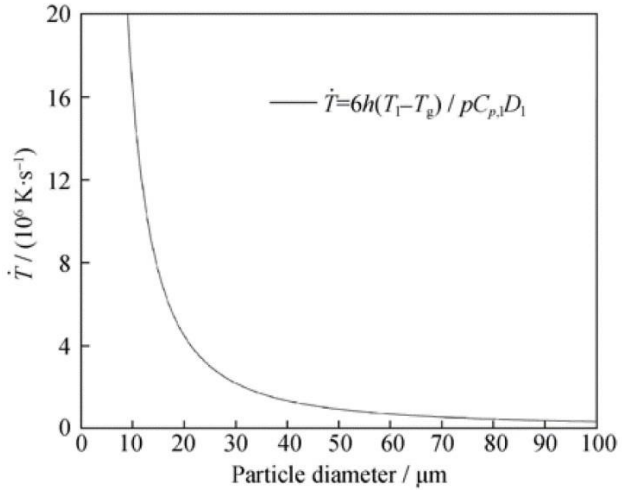

Figure 2: Calculated cooling rate as a function of particle size for gas-atomized 17-4 PH stainless steel powder under nitrogen environment [1].

A microstructural characterization of 17-4 PH powder gas-atomized under nitrogen was conducted using EBSD. The orientation maps obtained are shown in ***Figure.3***. Each particle consists of several grains. The grains don't show any evidence of lathes of martensite or large misorientaions, which is characteristic of a martensitic microstructure. However, low angle misorientaions can be seen inside the grains (slight difference in color). Furthermore, the phase has a BCC structure. No austenite was found in this EBSD analysis. This finding is not in agreement with previous results [5] showing evidence of austenite in 17-4 PH powders gas-atomized under nitrogen. Thus, it is suggested that the microstructure of 17-4 PH gas-atomized powders is ferritic, specifically δ ferrite. As mentioned in the previous paragraph, the cooling rates experienced during powder gas-atomization are very high (10^5-10^7 K/s), which are similar to the ones experienced during the SLM fabrication. Thus, due to the high cooling rates experienced during gas-atomization, the austenite doesn't have sufficient time to form. The powder will solidify primarily as δ ferrite. The latter won't experience any metallurgical transformation and will be retained to room temperature. This is the same "by-passing" phenomenon experienced by the SLM-ed 17-4 PH steel (see Chapter 2).

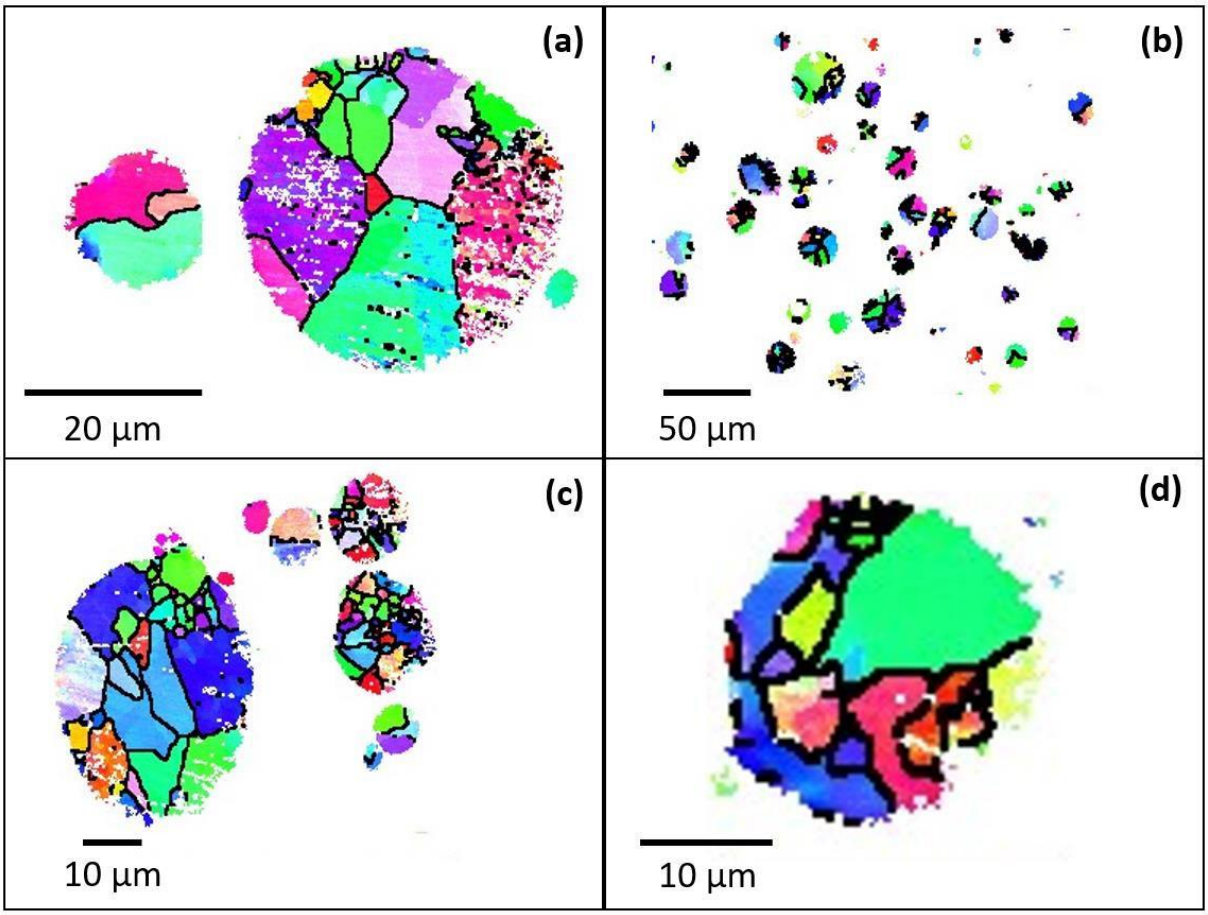

Figure 3: (a), (b), (c) and (d) EBSD orientation maps (IPF Z) at different magnification of 17-4 PH powders gas-atomized under nitrogen environment.

References

[1] X. Zhao, J. Xu, X. Zhu, S. Zhang, W. Zhao, G. Yuan, Characterization of 17-4PH stainless steel powders produced by supersonic gas atomization, Int J Miner Metall Mater. 19 (2012) 83–88. https://doi.org/10.1007/s12613-012-0519-0.

[2] G.S.E. Antipas, Review of gas atomisation and spray forming phenomenology, Powder Metallurgy. 56 (2013) 317–330. https://doi.org/10.1179/1743290113Y.0000000057.

[3] G.S.E. Antipas, Liquid Column Deformation and Particle Size Distribution in Gas Atomization, MSA. 02 (2011) 87–96. https://doi.org/10.4236/msa.2011.22012.

[4] M.A. Otooni, Elements of Rapid Solidification: Fundamentals and Applications, Springer Berlin Heidelberg, Berlin, Heidelberg, 1998. http://books.google.com/books?id=ZeRTAAAAMAAJ (accessed October 25, 2019).

[5] L.E. Murr, E. Martinez, J. Hernandez, S. Collins, K.N. Amato, S.M. Gaytan, P.W. Shindo, Microstructures and Properties of 17-4 PH Stainless Steel Fabricated by Selective Laser Melting, Journal of Materials Research and Technology. 1 (2012) 167–177. https://doi.org/10.1016/S2238-7854(12)70029-7.

Appendix 4: Conventional and real strain rates during tensile testing

The constant displacement rates applied during the tensile tests in air and under hydrogen charging are 10^{-6}, 10^{-5} and 10^{-4} mm/s, which correspond respectively to the "conventional" strain rates of 10^{-7}, 10^{-6} and 10^{-5} /s ($\dot{\varepsilon} = \frac{\text{displacement rate}}{\text{gage length}}$, gage length = 10 mm). ***Figure.1*** depicts the schematic representation of the tensile machine during a test in air. The displacement rate is applied on the moving crosshead. The crosshead displacement includes not only the specimen elongation, but also additional device-related deformation (grips, fixing systems). However, the LVDT sensor will measure the displacements of the entire specimen and some parts of the grips, while the extensometer will measure the actual elongation of the gage part of the specimen. Thus, the strain experienced by the specimen (real strain) is the one measured by the extensometer. During tensile test under hydrogen charging, the specimen was placed in an electrochemical cell. The measurement by the extensometer was not possible and thus only measurement by LVDT sensor (placed outside the cell) was conducted.

Figure.2 shows the displacement values measured from the internal LVDT sensor fixed on the moving crosshead, the external LVDT sensor fixed on both side of the corrosion cell and the extensometer as a function of time during a tensile test under air at 10^{-5} mm/s. The displacement speed of the crosshead is constant, since it is the set point fixed to the machine for the tensile test. The curves measured by external LVDT sensor and extensometer have time dependent strain rates. Their curves can be divided into two lines with approximately constant strain rates: first line corresponds to the elastic domain and the second line corresponds to the plastic domain of the specimen. As can be seen, the displacement rates ($5\ 10^{-7}$ mm/s for the extensometer and $2\ 10^{-6}$ mm/s for the LVDT sensor) in the elastic domain are different, while the displacement rates (10^{-5} mm/s) in the plastic domain are close to the displacement rate of the crosshead, and finally close to the targeted strain rate, considering the gage length of 10 mm of the specimen. This is because during the elastic loading of the specimen, the load on the device increases proportionally with the device deformation. The elongation is thus distributed over all the different parts of the fixing system, including the specimen. The elongation on the specimen is thus reduced and leads to a strain rate value lower than that targeted at the beginning of the test. When the material reaches its yield strength, all elongation occurs mainly on the specimen, even if a small part of the fasteners continues to be slightly deformed during the strain hardening. This corresponds to the domain where all the curves have the same slope in ***Figure.2***. The plastic strain rate is then in accordance with the set point. So, to summarize, the targeted strain rate is obtained on the specimen only in the plastic domain. In the elastic domain, the strain rate is significantly lower. If the

specimen fails in the elastic domain, or at the beginning of the plastic domain, as it is often the case under hydrogen, it means that the average stain rate (over the test duration) is significantly below the targeted one.

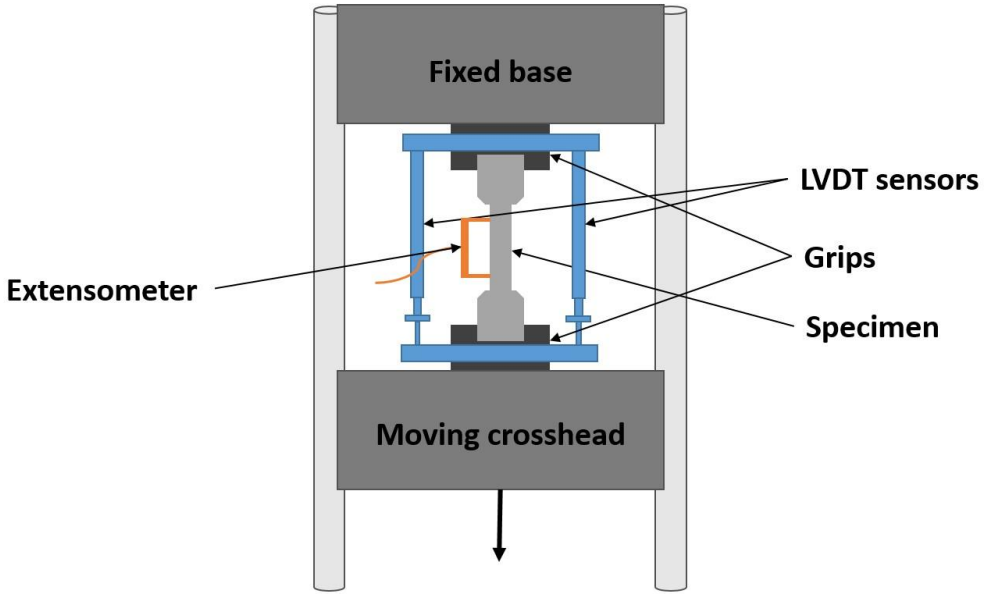

Figure 1: Schematic representation of the tensile machine during a test in air.

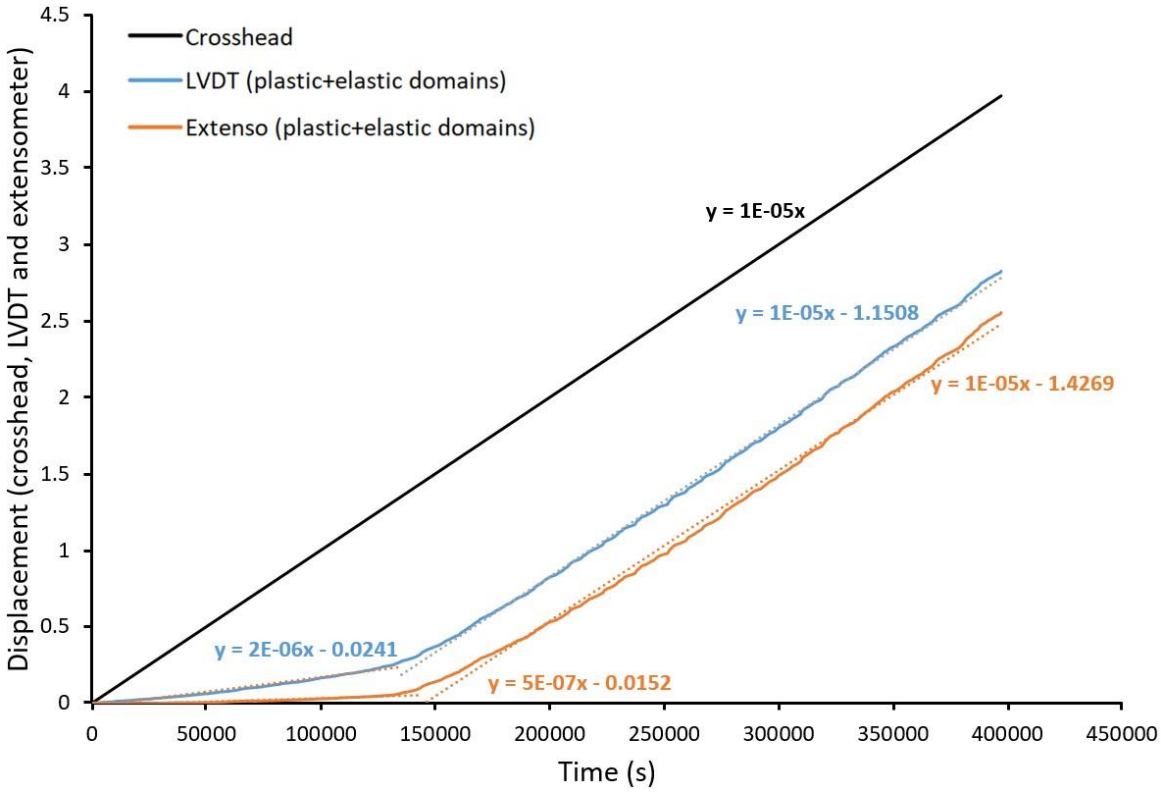

Figure 2: Displacements measured from crosshead, LVDT sensor and extensometer as a function of time during a tensile test at 10^{-5} mm/s.

Appendix 5: Correction methodology for the LVDT signal in tensile testing

As already mentioned, the extensometer cannot be used for tensile tests conducted in the electrochemical cell. Only the LVDT sensor is available. As explained in Appendix 3, the strain measured from LVDT sensor includes device-related deformation. Thus this strain needs to be corrected to obtain the correct strain-stress curve. The correction is conducted in two steps. First, in the elastic domain, the apparent strain measured from LVDT is divided by a constant (this constant is obtained in a previous experiment by comparing the strains form extensometer and from LVDT during a tensile test conducted in air). The first step is conducted in the elastic domain only, i.e. until the yield strength. Once this is done, the remaining part of the stress-strain curve (plastic domain + crack propagation) is simply shifted to the left to "stick" the two parts together again. An example of raw and corrected stress-strain curves is given is ***Figure.1***.

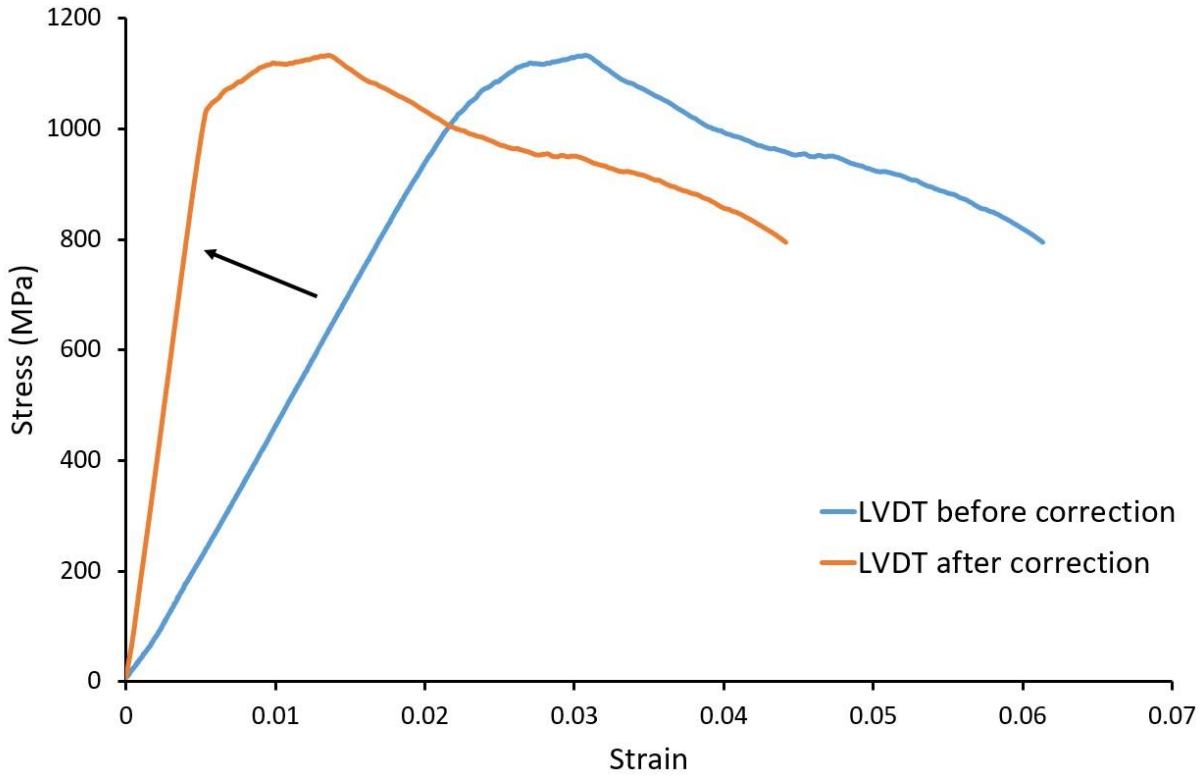

Figure 1: stress-strain curves measured by LVDT sensor before and after correction of a tensile test under hydrogen charging.

École Nationale Supérieure des Mines

de Saint-Étienne

NNT : *Communiqué le jour de la soutenance*

Michella ALNAJJAR

Corrosion properties of 17-4 PH martensitic stainless steel obtained by additive manufacturing

Speciality : Materials Science and Engineering

Keywords : Stainless steel, microstructure, SLM, electrochemical corrosion, hydrogen embrittlement

Abstract :

This PhD thesis focuses on the corrosion properties of 17-4 PH precipitation hardenable stainless steel obtained by additive manufacturing, specifically by Selective Laser Melting (SLM).

It was shown that the microstructure of 17-4 PH steel fabricated by SLM was ferritic, in contrast to the typical martensitic microstructure of the wrought 17-4 PH steel. This was correlated to the high cooling and heating rates (10^5-10^6 K/s) experienced during SLM that suppressed the δ ferrite to austenite transformation and retained the δ ferrite until the end of fabrication.

Since the microstructures of SLM-ed and wrought steels was different, it was expected that their corrosion properties would consequently be different. Thus, a comparative electrochemical study was conducted on both steels by performing anodic scans in acidic chloride solution. It was found that the SLM-ed steel had superior general corrosion resistance than the wrought steel. This was attributed to the absence of MnS inclusions in the SLM-ed steel. In contrast, in the wrought material, the dissolution of the MnS inclusions resulted in the redeposition of sulphur-rich species all over the surface, which contributed to the destabilization of the passive film.

A hydrogen embrittlement study was also conducted on both steels. It was found that the SLM-ed ferritic steel was more susceptible to hydrogen embrittlement (HE) than the wrought martensitic steel. The difference in microstructure, specifically the grain size, played a major role in this difference in behavior. In the SLM-ed ferritic steel subcritical cracking was transgranular and its initation was governed by the stress level and the amount of hydrogen introduced into the material. On the other hand, in the wrought martensitic steel, subcritical cracking was along the prior austenitic grain boundaries and it was shown that its initiation required at least a small amount of plastic deformation.

École Nationale Supérieure des Mines

de Saint-Étienne

NNT : *Communiqué le jour de la soutenance*

Michella ALNAJJAR

Durabilité de l'acier inoxydable martensitique 17-4 PH obtenu par fabrication additive

Spécialité: Sciences et Génie des Matériaux

Mots clefs : Acier inoxydable, microstructure, SLM, corrosion électrochimique, fragilisation par l'hydrogène

Résumé :

Ce travail de thèse porte sur la corrosion de l'acier inoxydable à durcissement structural 17-4 PH élaboré par fabrication additive par fusion sélective laser (SLM).

Nous avons montré que la microstructure de l'acier 17-4 PH fabriqué par SLM est ferritique, contrairement à l'acier corroyé qui présente une microstructure martensitique typique. Ceci résulte des vitesses de refroidissement et de chauffage très élevées (10^5-10^6 K/s) qui empêchent la formation de l'austénite et conduisent à une rétention complète de ferrite δ issue de la solidification.

Ces microstructures très différentes pouvaient laisser présager de fortes différences de comportement en corrosion. Nous avons mené une étude comparative de corrosion électrochimique à l'aide de courbes de polarisation anodiques dans des solutions chlorurées acides. Le matériau SLM présente une meilleure résistance à la corrosion généralisée que le matériau corroyé. Ce résultat est lié à l'absence d'inclusions MnS dans le matériau SLM. Au contraire, dans le matériau corroyé, la dissolution des inclusions MnS conduit à une redéposition d'espèces riches en soufre sur toute la surface, ce qui déstabilise le film passif.

Nous avons également mené une étude de la fragilisation par l'hydrogène des deux matériaux. Cette étude a montré une sensibilité plus forte du matériau SLM, qui peut s'expliquer par la différence de microstructure, en particulier la taille grains. Le matériau SLM, ferritique, présente une fissuration sous-critique transgranulaire, dont l'initiation est pilotée par le niveau de contrainte et la quantité d'hydrogène introduite dans le matériau. Au contraire, dans l'acier corroyé, martensitique, la fissuration sous-critique suit les anciens joints austénitiques. On montre par ailleurs que son initiation nécessite un minium de déformation plastique.